Nuclear Resonance Fluorescence for Safeguards Applications

Prepared for:
Materials Protection, Accounting and Control for Transmutation (MPACT)
Fuel Cycle Research and Development
Office of Nuclear Energy
U.S. Department of Energy
Work Package No.: FTLB11MP0212

Prepared by:

B.A. Ludewigt[1], B.J. Quiter[1], and S.D. Ambers[2]

[1]Lawrence Berkeley National Laboratory, Berkeley, CA 94720
[2]University of California, Berkeley, CA 94720

February 4, 2011

DISCLAIMER

ACKNOWLEDGMENTS

This work was supported by the MPACT Campaign of the FCRD Program of the Office of Nuclear Energy, U.S. Department of Energy under Contract No. DE-AC02-05CH11231.

Executive Summary

In nuclear resonance fluorescence (NRF) measurements, resonances are excited by an external photon beam leading to the emission of gamma rays with specific energies that are characteristic of the emitting isotope. The promise of NRF as a non-destructive analysis technique (NDA) in safeguards applications lies in its potential to directly quantify a specific isotope in an assay target.

This report addresses the assessment of NRF-based methods for safeguards applications in the context of related studies at LBNL, LLNL, and BNL. Our FY10 effort was comprised of three tasks: the study of the non-resonant scattering background and its simulation with MCNPX, analysis of our previously performed NRF transmission experiment, and the assessment of NRF for safeguards applications.

While the recent correction of the treatment of Rayleigh scattering in MCNPX resulted in much better agreement with some experimental data, the photonuclear processes, which are important contributors to the elastic scattering background at higher energies, are still not included. Our analysis showed that calculations based on ENDF form factors as currently implemented in MCNPX could underestimate the elastic scattering cross section by as much as a factor of ten for a uranium target at photon energies above 2 MeV. Even larger discrepancies, up to several orders of magnitude, are possible for lighter elements such as zirconium. It would be desirable to at least include nuclear Thomson scattering in MCNPX simulations for NRF studies.

The transmission experiment, using a bremsstrahlung beam and a target of comparable thickness to a spent nuclear fuel assembly, demonstrated sensitivity to a ^{238}U content of 1%. However, the precision was count rate limited. The data obtained in this experiment indicated notch refill that could change the measured NRF rates by up to 5% for the worst case. A correction based on MCNPX modeling has been implemented in the analysis.

NRF-based methods were assessed for three potential safeguards applications: the isotopic assay of spent nuclear fuel (SNF), the measurement of ^{235}U enrichment in UF$_6$ cylinders, and the determination of ^{239}Pu in mixed oxide (MOX) fuel. Given the small integrated nuclear resonance cross sections, the main challenge in these application, albeit to a varying degree, lies in accruing of sufficient counting statistics in an acceptable measurement times for achieving the desired uncertainties.

Pu isotopic masses in SNF could precisely be determined in transmission measurements using bremsstrahlung sources, but such measurements would require up to 100's of hours, a very intense bremsstrahlung source, and a very large array of fast detectors with high energy resolution. Quasi-monoenergetic photon sources such as Laser Compton scattering sources could potentially enable greatly improved performance. As an example, assuming a photon source with a 1 keV energy spread, an intensity of 6x10^8 ph/eV/s, and operating continuously or at very high pulse rates, the measurement time would be on the order of hours using a large detectors array. Shorter measurement times would require sources with narrower energy spreads and higher intensities. However, LCS sources of the type under development at LLNL are pulsed at kHz or lower rates and threshold detectors, such as Cherenkov detectors, are needed that integrate the photon signal and are not rate-limited. In a best-case scenario, a measurement with 1% statistical uncertainty could be accomplished with a 10^8 ph/eV/s photon source and an ideal threshold detector array

in 10 min. While this indicates promise, neither photon source nor detector technology presently exists.

The determination of ^{235}U enrichment in UF$_6$ cylinders is less demanding than SNF assay. The transmission method could be applied to the smaller cylinders up to 12" in diameter. Using an intense bremsstrahlung beam and a dozen HPGe detectors, a 5% precision measurement of 5% enrichment could be performed in less than 1/2 hour. For larger cylinders, through which the photon beam cannot be transmitted, the backscattering method could be used to measure enrichment to a depth of roughly 10 cm. As an example of a fresh fuel assay, we considered the measurement of 2.5% ^{239}Pu in a MOX fuel pin. Using an intense bremsstrahlung beam and an array of 24 HPGe detectors in a backscatter arrangement the ^{239}Pu content could be measured with 5% statistical uncertainties in roughly 3 hours. As in the case of SNF assay, much shorter measurement times could potentially be achieved with future intense quasi-monoenergetic photon sources.

Further research is essential to fully assess the NRF technique for safeguards applications and to develop future systems. To overcome the challenge of accruing sufficient counting statistics, the development of very intense LCS photon sources with small energy spreads is of utmost interest, as is the development of very fast, high-resolution γ-ray detectors and efficient threshold detectors. A high priority for assessing NRF measurements of Pu in SNF is to determine if ^{240}Pu has sufficiently strong NRF resonances so that this isotope could be measured using available photon sources and detectors. Also of interest is the expansion of nuclear data for other important actinides including long-lived Pu isotopes, ^{233}U, and possibly other transuranic isotopes. For accurate NRF-based measurement more precise and accurate resonance cross sections will be needed for all isotopes of interest.

Contents

List of Acronyms

ACE	nuclear data file format used by MCNP
ADC	Analogue-to-Digital Converter
BNL	Brookhaven National Laboratory
CDF	Cumulative probability Distribution Function
CW	Continuous Wave - particle accelerators that are not pulsed
DBLP	Doppler-broadened Lorentzian cross section Profile
DU	Depleted Uranium
ENDF	Evaluated Nuclear Data File
ENSDF	Evaluated Nuclear Structure Data File
EPDL	Evaluated Photon Data Library (97)
FCR & D	Fuel Cycle Research and Development
FEL	Free Electron Laser
FWHM	Full-Width at Half-Maximum
GDR	Giant Dipole Resonance
HIγS	High Intensity γ-ray Source
HPGe	High-Purity Germanium detector
IAEA	International Atomic Energy Agency
IOI	Isotope of Interest for transmission assay measurements
LBNL	Lawrence Berkeley National Laboratory
LLNL	Lawrence Livermore National Laboratory
LCS	Laser Compton Scattering photon sources
MCNP	computer program Monte Carlo N-Particle
MCNPX	computer program Monte Carlo N-Particle eXtended
MOX	Mixed oxide fuel
MPACT	Materials Protection, Accounting and Control for Transmutation
NA-221	DOE Office of Proliferation Detections
NDA	Non-Destructive Assay
NGSI	Next Generation Safeguards Initiative
NIST	National Institute of Standards and Technology
NJOY	daughter nuclear data processing code of program MINX: Multi-group Interpolation of Nuclear X-Sections
NRES	Non-Resonant Elastic Scatter
NRF	Nuclear Resonance Fluorescence
PDF	Probability Distribution Function
QM	Quasi-Monoenergetic photon source
RIPL	Reaction/Interaction Parameter Library
SNF	Spent Nuclear Fuel
TD	Transmission detector (comprised of IOI)
USDOE	United States Department of Energy
wt.%	weight percent
XCOM	NIST X-ray attenuation coefficient database

1 Introduction

In nuclear resonance fluorescence (NRF) measurements, resonances are excited by an external photon beam leading to the emission of γ rays with specific energies that are characteristic of the emitting isotope[1, 2]. The promise of NRF as a non-destructive analysis technique (NDA) in safeguards applications lies in its potential to directly quantify a specific isotope in an assay target without the need for unfolding the combined responses of several fissile isotopes as often required by other NDA methods.

The use of NRF for detection of sensitive nuclear materials and other contraband has been researched in the past[3]. In the safeguards applications considered here one has to go beyond mere detection and precisely quantify the isotopic content, a challenge that is discussed throughout this report. Basic NRF measurement methods, instrumentation, and the analytical calculation of NRF signal strengths are described in Section 2.

Well understood modeling and simulation tools are needed for assessing the potential of NRF for safeguards and for designing measurement systems. All our simulations were performed with the radiation transport code MCNPX, a code that is widely used in the safeguards community. Our initial studies showed that MCNPX grossly underestimated the elastically scattered background at backwards angles due to an incorrect treatment of Rayleigh scattering. While new, corrected calculations based on ENDF form factors showed much better agreement with experimental data for the elastic scattering of photons on an uranium target, the elastic backscatter is still not rigorously treated. Photonuclear scattering processes (nuclear Thomson, Delbruck and Giant Dipole Resonance scattering), which are expected to play an important role at higher energies, are not yet included. These missing elastic scattering contributions were studied and their importance evaluated evaluated against data found in the literature as discussed in Section 3.

A transmission experiment was performed in September 2009 to test and demonstrate the applicability of the method to the quantitative measurement of an isotope of interest embedded in a thick target. The experiment, data analysis, and results are described in Section 4.

The broad goal of our NRF studies is to assess the potential of the technique in safeguards applications. Three examples are analyzed in Section 5: the isotopic assay of spent nuclear fuel (SNF), the measurement of ^{235}U enrichment in UF$_6$ cylinders, and the determination of ^{239}Pu in mixed oxide (MOX) fuel. The study of NRF for the assay of SNF assemblies was supported by the Next Generation Safeguards Initiative (NGSI) of the U.S. Department of Energy as part of a large multi-lab/university effort to quantify the plutonium (Pu) mass in spent nuclear fuel assemblies and to detect the diversion of pins with non-destructive assay (NDA) methods. NRF is one of 14 NDA techniques being researched. The methodology for performing and analyzing quantitative NRF measurements was developed for determining Pu mass in SNF and is extensively discussed in this report. The same methodology was applied to the assessment of NRF for the measurement of ^{235}U enrichment and the determination of ^{239}Pu in MOX fuel. The analysis centers on determining suitable NRF measurement methods, measurement capabilities that could be realized with currently available instrumentation, and photon source and detector requirements for achieving useful NDA capabilities.

2 Quantitative NRF Measurements

Nuclear resonance fluorescence is the process by which a nucleus absorbs energy in the form of electromagnetic radiation, is excited to a nuclear state, and then subsequently de-excites to the ground state by the emission of one or more γ rays. As will be discussed in detail later, the angular distribution of re-emitted photons is governed by the angular momenta of the states involved in the process. The energy of the emitted γ rays is slightly below that of the NRF-inducing photons due to the energy transfered to the nucleus (nuclear recoil).

The energies of the photon that induced the initial excitation, and the energy of the re-emitted photon(s) are characteristic of the specific state that underwent NRF and therefore, characteristic of the isotope. Photons produced during de-excitation of an NRF state are referred to herein as NRF γ rays. Because NRF states are simply excited nuclear states, possible NRF γ-ray energies range from 10's of keV up to many MeV. However, for the purpose of using NRF to assay materials, photons of energy between 1.5 and 4 MeV are most useful.

Both, the elastic and inelastic scattering of photons may contribute to the background. Measurements of NRF γ rays at backwards angles, relative to the interrogating beam direction, yields backgrounds that are significantly reduced compared to forward angles.

2.1 Nuclear Resonance Fluorescence

In the context of assaying materials, NRF is usually induced by exciting nuclear states with a beam of photons. The subsequent NRF γ rays are measured using photon detectors such as high-purity germanium (HPGe) or scintillation detectors. Because NRF states correspond to excited nuclear levels, the photo-absorption and NRF γ-ray energies identify the nucleus that has undergone NRF, analogous to passive γ-ray spectroscopy.

If assay geometry and NRF cross section are known, measuring the rate at which NRF occurs allows the number of atoms of the corresponding isotope to be determined. The rate at which a nuclide undergoes NRF in thin targets is given by

$$R = \int N\Phi(E)\sigma(E)dE \tag{2.1}$$

Thicker targets require geometrical corrections due to the fact that the energy-dependent photon flux, $\Phi(E)$ changes as it traverses the target. This will be discussed in Section 2.4.1.1.

The cross section for photo-excitation of a nuclear state is given by the Breit-Wigner distribution

$$\sigma(E) = \pi g \frac{(\hbar c)^2}{E^2} \frac{\Gamma\Gamma_0}{(E - E_c)^2 + (\Gamma/2)^2} \tag{2.2}$$

where Γ is the full-width at half maximum (FWHM) of the state, Γ_0 is the partial width of the state for decay by γ ray emission to the ground state, E_c is the centroid energy of the resonance, and g is a statistical factor equal to the ratio of the number of spin states available for the excitation to the number of initial spin states. For NRF events where the initial nuclear state is the ground state, it is

$$g = \frac{2J+1}{2(2J_0+1)} \tag{2.3}$$

where J and J_0 are the angular momentum quantum numbers of the excited and ground states, respectively. There are $2J+1$ magnetic substates for a state of angular momentum J, and the additional factor of 2 in the denominator is due to the fact that the photons inducing excitation can have two possible helicities.

The probability for de-excitation of a state by a specific mode (i.e. neutron emission, γ-ray emission, etc.) yielding a lower-energy state can be defined by the state's partial width for that mode,

$$p_i = \frac{\Gamma_i}{\sum\limits_j \Gamma_j} = \frac{\Gamma_i}{\Gamma} \tag{2.4}$$

where we have used

$$\Gamma = \sum_j \Gamma_j \tag{2.5}$$

implying that the summation over j includes all possible de-excitation modes. Combining equation 2.2 and 2.4, we note that the cross section for NRF to occur via emission of a single γ ray, and de-excitation to the ground state is given by

$$\sigma_{\mathrm{GS}}(E) = \frac{\Gamma_0}{\Gamma}\sigma(E) = \pi g \frac{(\hbar c)^2}{E^2} \frac{\Gamma_0^2}{(E-E_c)^2 + (\Gamma/2)^2} \tag{2.6}$$

2.1.1 NRF γ-ray Angular Distributions

NRF is generally considered to only occur between states that differ by 2 or fewer units of angular momentum. The angular distribution of NRF γ rays, relative to the NRF-inducing radiation can be described by the same spin algebra that is used to define angular correlations in γ-ray cascades[5].

The cross section for NRF γ-ray emission at a direction, θ, relative to the incident photon beam is given by

$$\sigma(\theta) = W(\theta)\sigma \tag{2.7}$$

where, $W(\theta)$, denotes the angular correlation function. For a more in depth discussion of angular dependence see reference[2].

^{239}Pu has a spin-1/2 ground state and only transitions that return to the ground state are considered in this discussion. Transitions of the form $1/2 \rightarrow 1/2 \rightarrow 1/2$, $1/2 \rightarrow 3/2 \rightarrow 1/2$, and $1/2 \rightarrow 5/2 \rightarrow 1/2$, are all expected to be possible in NRF ($\Delta J \leq 2$). Furthermore, the multipolarity of the $1/2 \rightarrow 3/2$ excitation may be either dipole or quadrupole (due to vector spin addition rules), and likewise for the $3/2 \rightarrow 1/2$ de-excitation. The angular distributions predicted for purely dipole-dipole and purely quadrupole-quadrupole transitions happen to be the same, but if the excitation occurs via quadrupole and the de-excitation via dipole (or vice-versa) the expected $W(\theta)$ differs significantly. Because the actual intensities of quadrupole versus dipole transitions (commonly referred to as the *mixing ratio*, δ) can vary from state to state, any possible $W(\theta)$ distribution combination is allowed.

The cases of ground-state to ground-state NRF on spin 1/2 nuclei is presented in Figure 2.1. The red curve indicates a $1/2 \rightarrow 3/2 \rightarrow 1/2$ transition where both the photon multipolarities were both either dipole or quadrupole, whereas the green curve indicates a transition where one photon was dipole, and the other quadrupole. The area between the curves has been shaded gray to indicate that any possible angular correlation function between these two extremes is physically possible. Finally, the sequence $1/2 \rightarrow 5/2 \rightarrow 1/2$ (assuming octupole radiation is negligible) is only described by quadrupole transitions.

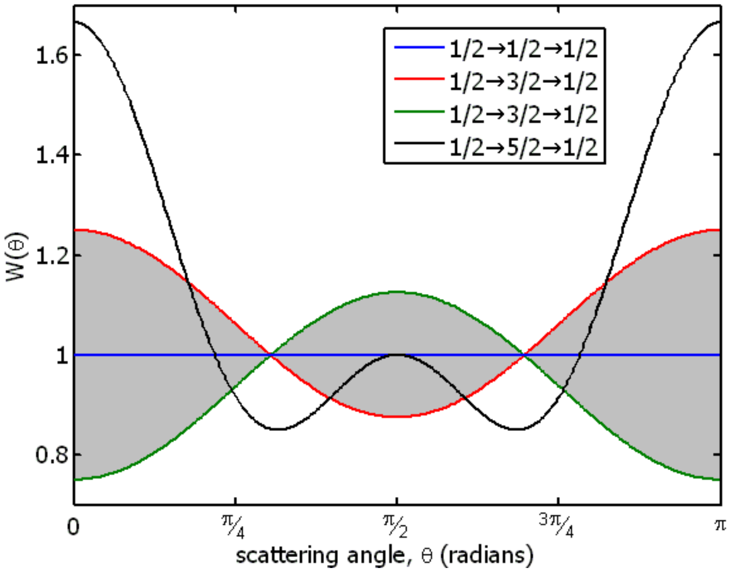

Figure 2.1 The angular correlation functions, $W(\theta)$ for NRF between states of initial and final spin 1/2 allowed by dipole and quadrupole radiation. See text for discussion.

2.1.2 Thermal Motion and Nuclear Recoil

The process of NRF is connected to the environment of the nucleus due to the fact that nuclei, as part of atoms, are not stationary, but are always in thermal motion. In the case where NRF is induced on a nucleus that is part of a gaseous molecule, the thermal velocity distribution of the nuclei leads to the Doppler broadening of the resonances.

The *Doppler width* of a broadened resonance is commonly refered to as

$$\Gamma_D \equiv 2\sqrt{2\ln 2}\Delta = 2.3548\Delta \tag{2.8}$$

with

$$\Delta = E\sqrt{\frac{k_B T}{Mc^2}} \tag{2.9}$$

because it describes the FWHM of the energy distribution[1]. M is the mass of the nucleus, k_B is the Boltzmann constant and T is the absolute temperature of the gas.

---

[1] It should be noted that another common definition of the Doppler width is $\sqrt{2}\Delta$. This definition is not used in this document.

The Doppler-broadened Lorentzian profile (DBLP) can be expressed as

$$\sigma_D(E) = \frac{\sqrt{\pi} g(\hbar c)^2 \Gamma\Gamma_0}{\sqrt{2}\Delta} \int_0^\infty dE' \frac{1}{(E'-E_c)^2 + (\Gamma/2)^2} \frac{\exp(-(E'-E)^2/2\Delta^2)}{E'^{\,2}} \tag{2.10}$$

As an illustrative example, Figure 2.2 demonstrates the effect that a Maxwell-Boltzmann energy distribution can have on the effective resonance shape that an incident photon experiences. This case describes a 2.175 MeV centroid energy (E_c) ^{238}U resonance with a width, $\Gamma = 54$ meV and that de-excites by photon emission to the ground state 68% of the time ($\Gamma_0/\Gamma = 0.68$). The spin of the ground state is 0, and that of the excited state is assumed to be 1, such that $g = 3/2$. This distribution is also broadened due to the motion of the atoms, which have been described by a Maxwell-Boltzmann velocity distribution for ^{238}U at 300 K: $\Gamma_D = 1.78$ eV. The corresponding energy probability distribution was multiplied by $\int \sigma(E)dE$, and is shown as the green line in Figure 2.2. Equation 2.10 was numerically integrated for these parameters for an array of incident photon energies and the resulting effective cross sections are shown as the dots on the red line in Figure 2.2. This example demonstrates that the width of the effective cross section distribution will be broader than that of the energy distribution and that of the natural cross section.

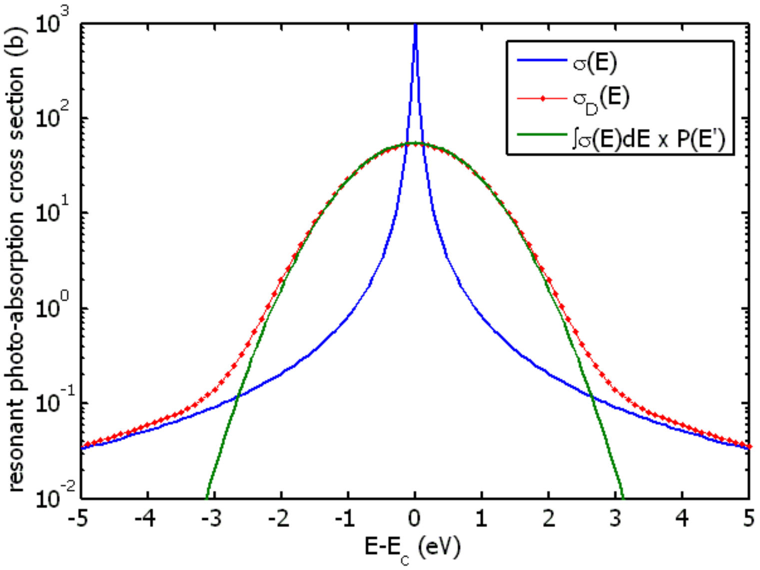

Figure 2.2 Effective resonance shape experienced by an incident photon, for the 2175 keV resonance of ^{238}U at 300 K. For this resonance, $\Gamma = 54$ meV, $\Gamma_0 = 37$ meV, and $g = 3/2$.

Non-amorphous solids are composed of crystalline arrangements of constituent atoms. These atoms vibrate with thermal energy, which can be described as a phonon.The effects of phonons are most evident when the nuclear recoil energy is not significantly greater than typical phonon energies. However, above ~ 1.5 MeV, the influence of crystalline phonons on the energy distribution of the nuclei continues to have measurable effects. In particular, the binding energy of the crystal and the phonon-induced motion causes crystalline atoms to vibrate faster than gaseous atoms at the same temperature. In the limit that $\Delta/\sqrt{2} + \Gamma >> 2k_B\theta$, the effective temperature at which equation 2.10 should be evaluated[1, 6] is

$$\frac{T_{eff}}{T} = 3\left(\frac{T}{\theta}\right)^3 \int_0^{\theta/T} t^3 \left(\frac{1}{\exp(t)-1} + \frac{1}{2}\right) dt \tag{2.11}$$

where, θ is the Debye temperature of the crystal, which is a physical property of a material that is related to the theoretical maximum energy a single phonon can carry in the material.

Finally, we consider the influence of momentum conservation on NRF physics. Conservation of momentum requires that when a nucleus of mass, M absorbs a γ ray of energy, E_γ, and momentum, E_γ/c, it will recoil with the γ ray's momentum, which translates to an energy

$$E_{\text{recoil}} = \frac{E_\gamma^2}{2Mc^2} \tag{2.12}$$

For example the 2431 keV resonance of ^{239}Pu corresponds to a recoil energy of 13.2 eV. The conservation of momentum applies to the re-emission of NRF γ rays as well. Upon resonance absorption, a nucleus will recoil with energy given by equation 2.12. NRF state lifetimes tend to be on the order of 10^{-17} to 10^{-12} s, implying that the nucleus will re-emit an NRF γ ray before slowing down to thermal velocities. In the event that the γ ray is emitted in precisely the same direction as the incident exciting photon, the nucleus would recoil back to its initial velocity. If the γ ray is emitted in a different direction, the nucleus will again recoil from γ-ray emission and the resulting NRF γ ray will be lower in energy than the initial photon. Most probably, this energy difference will be larger than the Doppler-broadened width of the NRF resonance, and thus the emitted NRF γ ray will no longer be resonant.

2.2 Measurement Methods

In this section the development and use of two methods to measure nuclear resonance fluorescence rates for non-destructive materials assay studies are discussed. The two assay methods considered here are termed *backscatter* and *transmission* assay. They differ in how photons undergoing NRF in the assay target are observed. Both methods use a photon source to induce NRF in the target material. In backscatter assay, a radiation detector is positioned at backwards angles relative to the incident photon beam trajectory. In transmission assay a detection system down-stream of the assay target is used to measure the excess attenuation of resonant-energy photons in the target. Both methods have advantages and disadvantages that will be discussed in the following sections.

2.2.1 Backscatter Method

Schematic drawings of backscatter NRF assay geometries are shown in Figure 2.3. A source of energetic photons illuminates the target material and one or more radiation detectors measure the photon flux backscattered from the target. The interogating photons stimulate resonances in the isotope of interest (IOI), e.g., ^{239}Pu within spent nuclear fuel, which promptly de-excite by nearly isotropic emission of one or more photons. These NRF γ rays are mixed in with the photon flux backscattered from the target.

The background, non-resonant photon flux in the backscattered direction relative to the beam incident upon the target is composed of elastically and non-elastically scattered interrogation photons and photons from radioactive decays in the target. The detectors used are positioned at backwards angles where the background photon flux is lowest and the signal-to-background ratio the highest. They are shielded from the interogation source using large amounts of shielding, such as lead or tungsten. To limit the count rate seen by the detector due to low energy scattered photons, 511 keV photons, and the radioactivity of the target, lead shielding, or filters, are placed in front of the detectors. Filters may consist of up to ~200 g/cm^2 of high-Z material, depending on photon beam characteristics and detector count rate limitations. They are application-specific and will be discussed in specific assay examples in Section 5. As discussed further in Section 2.3.2 better detector energy resolution increases the statistical value of registered NRF counts. Because of this, high-purity germanium detectors (HPGe) are most commonly used for NRF experiments.

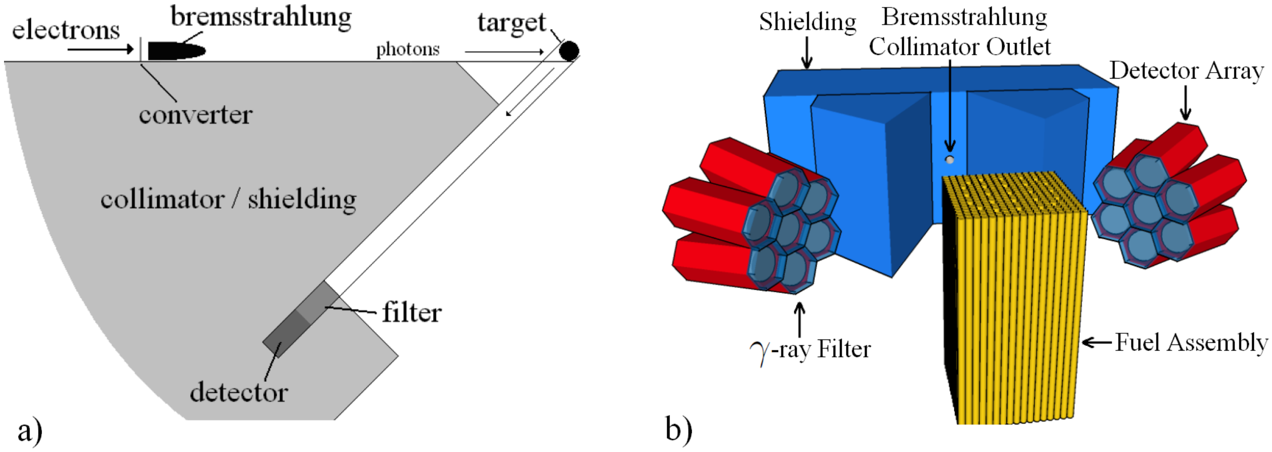

Figure 2.3 Schematic drawing of bremsstrahlung-induced backscatter NRF assay setups. Figure 2.3 a) on the left, depicts a measurement on a single fuel pin. Figure 2.3 b) on the right shows a possible arrangement for a measurement on a fuel assembly.

The measurement of NRF γ rays at backward angles suffers from the disadvantage that radioactivity emitted by the assay target can necessitate thick filters in front of the detectors, which subsequently reduce the NRF γ-ray detection rate. The NRF signal is also depth dependent and the method is more sensitive to radiation backscattered from the front of the target rather than from deeper in the target, resulting in potentially biased results for non-homogeneous targets. The transmission method described in the following section mitigates these disadvantages at the expense of a more complicated assay system and the need for stronger interrogating photon beams.

2.2.2 Transmission Method

The concept of an NRF assay using the spectrum transmitted through the target is as follows: an interrogating beam impinges upon the assay target and the spectrum transmitted through the target is then incident upon a thin sheet made of the isotope to be assayed or IOI, called the transmission detector (TD) or witness foil. Resonant-energy photons that impinge upon the TD may induce NRF. The NRF γ rays emanating from the TD are then detected by radiation detectors located at backward angles, relative to the incident bremsstrahlung beam. A schematic diagram of this assay type is shown in Figure 2.4.

The rate at which NRF γ rays are detected is a measure of the areal density of the IOI within the sensitive volume of the assay target which is defined as the region through which interrogating photons can penetrate and subsequently reach the TD without scatter. The rate of NRF in the target and thus the attenuation of resonant energy photons increases with the amount of the IOI within the target leading to a decrease in the rate of NRF in the TD (or witness foil).

For an ideal transmission measurement, the target thickness should be such that the IOI preferentially attenuates a significant fraction of the penetrating resonant-energy photons. Likewise,

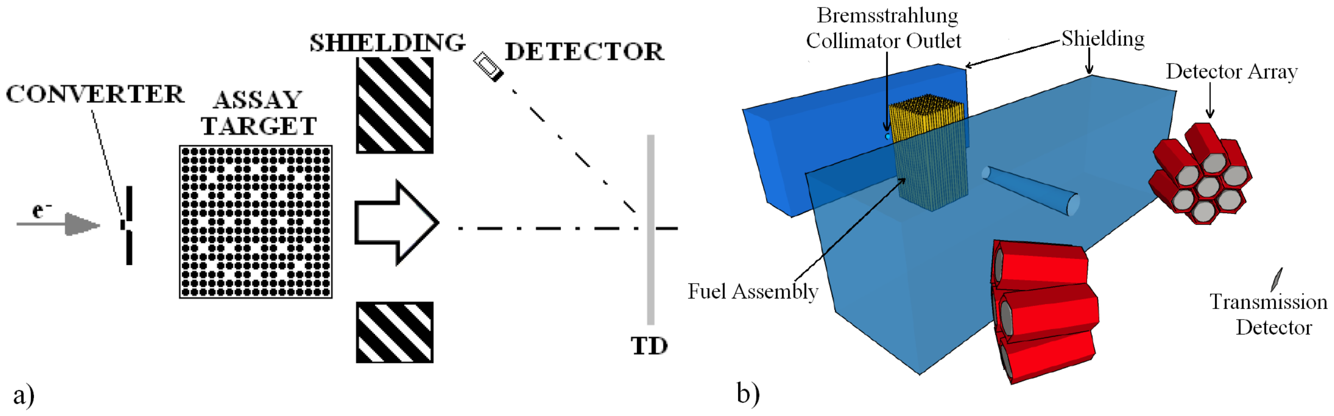

Figure 2.4 Schematic description of geometry used for transmission assay measurement.

the source of interrogating photons should be sufficiently intense such that the detectors used to view the TD operate near their rate limit.

For spent fuel, the areal densities of Pu isotopes are generally very low compared to this ideal case, and the excess attenuation of resonant-energy photons is small. Thus the transmission measurement is considered for spent fuel assemblies rather than fuel pins. The radioactivity of the spent fuel is not an impediment in this geometry since the detectors are well shielded.

The term *notch refill* is used to describe the process by which photons incident upon the assay geometry down-scatter to the energy of a resonance and subsequently interact in the transmission detection sheet. The process results in less observed resonant attenuation than would be predicted by consideration of simple exponential attenuation, and therefore neglect of the notch refill phenomenon could result in NRF transmission measurements that systematically under-predict the areal density of the measured isotope in the target.

Photon interaction processes that can induce notch refill include incoherent scatter and bremsstrahlung emission from photoelectrons. The rate at which notch refill occurs is dependent upon the compositions of the assay target and transmission detection sheet, their respective positioning, the energy and strength of a resonance, and the photon spectrum used for the measurement. For a more in depth discussion on notch refill see Section 3.3.3.

2.3 Instrumentation

2.3.1 Photon Sources

Two types of photon sources are being considered for NRF safegaurds applications. Bremsstrahlung sources are available and can provide intense photon beams. Quasi-monoenergetic photon sources offer great promise due to possibly very large increases in the signal-to-background ratio when compared to a bremsstrahlung source. However, quasi-monoenergetic sources are in the early stages of development and do not yet provide the necessary photon flux to, for example, precisely measure Pu content in spent fuel.

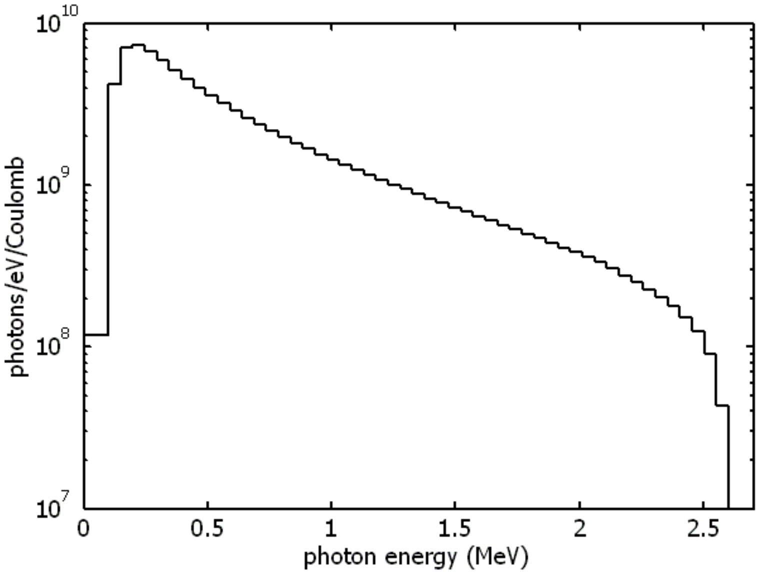

Figure 2.5 MCNPX-computed bremsstrahlung photons spectrum for photons leaving within 3.57° of the initial electron trajectory, for 2.6 MeV electrons normally incident upon 102 μm thick Au foil backed by 1 cm thick Cu.

2.3.1.1 Bremsstrahlung Sources

Bremsstrahlung sources utilize electron accelerators to produce photons in a conversion target. Newer electron accelerators, such as rhodotrons, have reported currents approaching ∼100 mA[9, 10]. A typical energy spectrum of photons produced by a bremsstrahlung source is shown in Figure 2.5. Only a small fraction of photons that are produced are at the energies of resonances. Most photons are produced at lower energies and must be filtered out in order to avoid saturating the γ-ray detectors.

2.3.1.2 Quasi-monoenergetic Sources

The most advanced quasi-monoenergetic (QM) source type to be considered are laser-Compton photon sources. When a laser beam is scattered off a beam of relativistic electrons, the photons are up-shifted in energy to produce photons whose energies are given by[11, 12, 13, 14, 15]:

$$E_\gamma = \frac{4\gamma^2 E_L}{1 + (\gamma\theta)^2 + 4\gamma E_L/m_e c^2} \tag{2.13}$$

where θ is the angle between the electron beam and the up-scattered photon, in radians, E_L is the laser energy, and γ is given by

$$\gamma = \frac{1}{\sqrt{1 - (v_e/c)^2}} \tag{2.14}$$

Table 2.1 presents an evaluation of equation 2.13 assuming a Nd:YAG laser is used as the low-energy photon source. For Nd:YAG laser energies, the electron energy must be adjustable between 335 and 375 MeV to produce photons capable of exciting the known ^{239}Pu resonances. Likewise, if the laser is frequency-doubled, the electron energy must be adjustable between 240 and 270 MeV.

Presently, the most intense source of QM photons of energies between 2 and 4 MeV is the High Intensity γ Source (HIΓS), [11]. It is capable of producing approximately 100 - 200 photons/eV/s

Table 2.1 Laser Compton photon energies given by equation 2.13.

E_{e^-} (MeV)	γ	E_L (eV)	θ (mrad)	E_γ (keV)
370.3	724.7	1.165	0.0	2431.5
370.3	724.7	1.165	0.2	2381.8
370.2	724.5	1.165	0.0	2430.2
347.6	680.2	1.165	0.0	2143.6
347.6	686.9	1.165	0.2	2104.7
262.2	513.1	2.330	0.0	2431.5
262.2	513.1	2.330	0.2	2406.4
246.1	481.8	2.330	0.0	2143.6
246.1	481.8	2.330	0.2	2125.5

at 2 MeV, with energy spreads ranging from 10 to 100 keV FWHM. HIΓS is primarily a free electron laser (FEL) based facility for nuclear physics research.

Pulsed lasers can provide much larger photon intensities than FELs and thus produce higher energetic photon intensities. Using higher repetition rates and better control of electron bunches, proposed facilities anticipate 1×10^6 photons/eV/s intensities and beam energy spreads as low as 1 keV. QM photon systems under construction are planned with 120 Hz lasers with 10 ps pulses[12]. Much higher repetition rates are desired for faster measurements. The possibility to time-correlate the counting of NRF γ rays with the timing of the source offer the potential for background suppression and additional measurement improvements.

The importance of very intense photon sources will discussed further in Section 5.

2.3.2 γ-ray Detectors

In order to use NRF to assay a material, the resonantly scattered photons must be observed against an intense background. Normally, this is best accomplished with high-resolution γ-ray detectors, but higher count rate capability may outweigh better energy resolution.

Today, high-purity germanium detectors (HPGe) provide the best energy resolution in the 2 - 3 MeV energy range. While micro-calorimeters have achieved better energy resolution, they have only been successful at measuring low-energy photons ($\lesssim$ 200 keV) at very low count rates[16, 17]. Thus in this report, HPGe detectors are considered the base-line detector and other detectors capable of higher count-rates are compared to HPGe. At 2 MeV, the HPGe energy resolution, ΔE, is approximately 2.5 keV (FWHM). HPGe and other detector types can vary significantly in size and shape. To generally account for this, we assume that a reference detector will be a 100% relative efficiency HPGe detector, with a surface area of approximately 50 cm^2.

2.3.2.1 Detector Energy Resolution and Statistics

To relate the relative intensities of NRF signals and backgrounds to the precision with which a measurement may be made, we present a simple statistical model. Suppose the signal of interest is detected at a rate, S. The background rate, B, is estimated by examining the count rate in adjacent channels. The total signal rate is, $T = S + B$. We define the signal-to-background

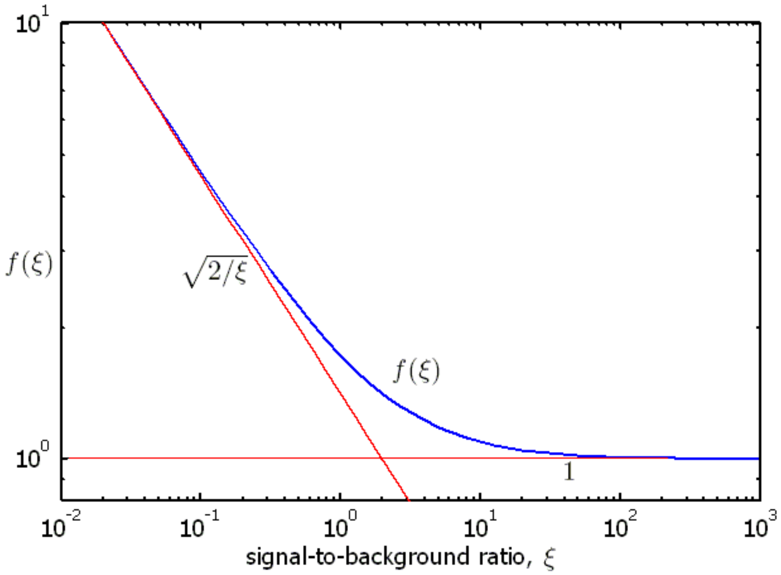

Figure 2.6 The relative increase in the fractional uncertainty of a measurement, $f(\xi)$, as a function of the signal-to-background ratio, ξ, along with the functions (red) that describe $f(\xi)$ as $\xi \to 0$ and $\xi \to \inf$.

ratio as $S/B = \xi$. After a counting period of t, we expect $t(S + B)$ total counts within the area of interest (presumably where an NRF peak is expected). The total number of counts from the signal is $N_S = tS$, with fractional uncertainty of $\vartheta = \frac{\sigma_S}{N_S}$. Assuming Poisson statistics, the standard deviation of the expected number of total counts, N, is $\sqrt{N}$, and we have

$$\vartheta = \frac{\sqrt{t(T+B)}}{tS} = \frac{\sqrt{S+2B}}{\sqrt{t}S} = \frac{\sqrt{1+2/\xi}}{\sqrt{N_S}} \equiv \frac{f(\xi)}{\sqrt{N_S}} \tag{2.15}$$

The function, $f(\xi)$, that expresses the reduction in statistical quality of a measurement of N_S signal counts varies as $f \sim \sqrt{2/\xi}$ for small values of ξ, whereas for large ξ, $f \to 1$. $f(\xi)$ is shown in Figure 2.6 along with the limiting functions. This observation leads us to conclude that the NRF count rate must be almost as intense as the background signal rate within the detector's energy resolution to obtain counts with reasonable statistical quality.

Background signals due to processes such as elastic and inelastic scattering will vary slowly for photon sources that are broad in energy resolution compared to those of detectors. Therefore, using a HPGe detector, it is necessary that the NRF interaction rate to be approximately 1000 ($\approx \Delta_E/\Gamma_D$) times the scattering rate of non-resonant photons to accrue NRF count rate statistics in an efficient manner. This ratio increases proportionally with detector resolution.

As an example, a $\mathrm{LaBr_3}$ scintillation detector has a resolution that is about 18 times worse than a HPGe detector[18]. This implies that the background count rate within the detector's resolution will be about 18 times higher than it would be for an HPGe detector, and if $\xi_{\mathrm{HPGe}} = 1$, the statistical value of a $\mathrm{LaBr_3}$ count,

$$f(\xi_{\mathrm{HPGe}})/f(\xi_{\mathrm{LaBr_3}}) \approx 1/3.5 \tag{2.16}$$

times less than that of an HPGe count. However, $\mathrm{LaBr_3}$ can operate at approximately 15 times higher count rates than HPGe, which may make its use advantageous, especially for transmission NRF measurements that use a TD .

Table 2.2 Parameters relevant for Cherenkov detectors of multi-MeV photons

material	n	E_{th} (MeV)	E_γ (MeV)
water	1.333	0.262	0.262
SiO_2 nanotube film	1.05	1.165	1.375
SF_6 gas @ 22 atm	1.025	1.817	2.044
SiO_2 aerogel	1.025	1.817	2.044
SF_6 gas @ 10 atm	1.008	3.553	3.793
SF_6 gas @ 1 atm	1.00078	12.41	12.66
air @ 1 atm	1.0003	20.6	20.8

2.3.3 Threshold γ-ray Detectors

The requirement that NRF detectors be capable of very high detection rates leads to investigation of alternative detector types, such as threshold detectors which only induce signals when incident particles have sufficient energy, e.g., Cherenkov detectors.[19, 20]

Cherenkov radiation is emitted when a particle such as an electron passes through a medium with a velocity, v_e, that is faster than the speed of light, $v_{h\nu} = c/n$ or if $v_e/c > 1/n$. This gives a minimum electron energy of

$$E_{th} = m_0c^2\left(\sqrt{1+\frac{1}{n^2-1}}-1\right) \tag{2.17}$$

Multi-MeV photons primarily interact by incoherent scattering or pair production. Electrons are primarily produced by incoherent scatter, yielding a continuum of electron energies up to $E_e = \frac{2E_\gamma^2}{m_ec^2+2E_\gamma^2}$. As E_γ increases, this value nears $E_\gamma - m_ec^2/2$. With E_γ in the NRF energy range (1.5 - 3 MeV), the difference between γ-ray energies and the most energetic Compton electrons is approximately 220 keV. Therefore in order to have some sensitivity for NRF photo-electrons, a Cherenkov detector must have $E_{th} < E_\gamma - 220$ keV. Table 2.2 lists the index of refraction of many materials, the threshold energy for electrons to produce Cherenkov radiation, and the corresponding minimum photon energy that will induce Cherenkov radiation.

Light yields tends to be proportional to the energy of the electron; examples can be found in Reference [20]. Because higher energy electrons induce larger signals, photons of higher energies than the resonance energy become particularly important as they contribute disproportionately to the measured signal, which is problematic especially for backscatter NRF measurements. We have found, see section 5.1.2, that these detector types would be useful in transmission measurements conducted using quasi-monoenergetic photon sources that are approximately 10^4 times more powerful than those currently being proposed.

2.4 Analytical Modeling

In this section the development and use of models to predict expected nuclear resonance fluorescence detection rates for non-destructive materials assay studies are discussed. We rely heavily on the use of analytical modeling to estimate the NRF rates because Monte Carlo simulations of NRF assays are very computationally intensive and time consuming even on large clusters. The

MCNPX code is used to simulate background rates and other scattering effects such as notch refill. We generally assume in our modeling that NRF is detected by a single radiation detector, and that use of multiple detectors would proportionally increase the calculated count rates. Advantages and disadvantages of the backscatter and transmission methods will be discussed in the following sections along with examples of measurements that have been modeled by a combination of computational and analytical methods.

2.4.1 Backscatter Assay

Schematic drawings of backscatter NRF assay geometries are shown in Figure 2.3. A source of energetic photons illuminates the target material (considered to be used fuel) and one or more radiation detectors measure the photon flux backscattered from the target. The photon flux at the detector, $\Phi(\mathbf{r_d}, E)$, which is proportional to the measured count rate, can be written as

$$\Phi(\mathbf{r_d}, E) = \Phi_{\text{target}}(\mathbf{r_d}, E) + \Phi_{\text{radioactivity}}(\mathbf{r_d}, E) + \Phi_{\text{beam}}(\mathbf{r_d}, E) \tag{2.18}$$

where $\Phi_{\text{target}}(\mathbf{r_d}, E)$ is the flux due to interrogating photons that were scattered toward the detector after interacting in the spent fuel, which includes the contribution due to NRF of constituent isotopes. $\Phi_{\text{radioactivity}}(\mathbf{r_d}, E)$ is the photon flux due to radioactive decay of materials within the interrogation geometry, and $\Phi_{\text{beam}}(\mathbf{r_d}, E)$ is due to interrogating beam photons that have reached the detector without interacting within the target material. Sufficient shielding must be placed between the bremsstrahlung source and the detectors to keep Φ_{beam} negligible.

2.4.1.1 NRF Count Rates

We consider the contributions to $\Phi_{\text{target}}(\mathbf{r_d}, E)$ due to resonant and non-resonant scattering separately. Resonant scattering produces NRF signals, whereas non-resonant scattering contributes to the background.

The rate at which NRF signals due to photons of energy, E, from a location, $\mathbf{r}$, within the target volume, V, are detected is given by

$$\frac{d^2 R_{\text{NRF}}}{dV dE} = N\Phi(E, \mathbf{r})\sigma_{\text{NRF}}(E) W_e(\theta) \exp[-\mu(E_\gamma) r_o] \left[\epsilon(E_\gamma)\frac{\Omega(\mathbf{r})}{4\pi} P_f(E_\gamma)\right] \tag{2.19}$$

where N is the number density of atoms in the target that undergo NRF with cross section $\sigma_{\text{NRF}}(E)$, $\Phi(E, \mathbf{r})$ is the energy-differentiated photon flux at the point $\mathbf{r}$, $W_e(\theta)$ is the effective angular correlation function (approximately given by equation 2.7), E_γ is the energy of the emitted NRF γ ray, which interacts within the target material with an attenuation coefficient, $\mu(E_\gamma)$, that results in a total attenuation of the NRF γ ray of $\exp[-\mu(E_\gamma) r_o]$, $\epsilon(E_\gamma)$ is the probability that the radiation detector measures the full energy of the NRF γ ray, $\frac{\Omega(\mathbf{r})}{4\pi}$ is the fraction of the solid angle subtended by the radiation detector from the point where the γ ray is emitted, and $P_f(E_\gamma)$ is the probability that the NRF γ ray penetrates through the radiation filter without scatter. The attenuation of NRF γ rays is only due to non-resonant interactions because the energy of the emitted γ rays is shifted out of the resonance due to the nuclear recoil.

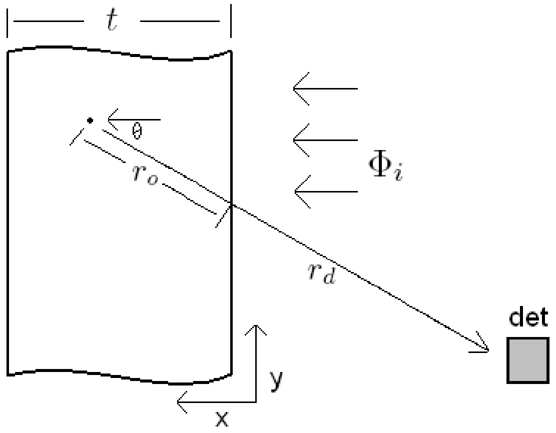

Figure 2.7 Schematic drawing of an NRF interrogation of a target slab.

2.4.1.2 Slab Geometry

The simplest geometry to consider is a slab target of thickness, t, irradiated with a uniform parallel beam of intensity, Φ_i, that is normally incident upon the slab. This geometry is applied to the calculation of the transmission detector response. A radiation detector is assumed to be located sufficiently far from the target that the beam diameter and slab thickness are negligibly small compared to the detector distance, r_d. A schematic rendering of this geometry is shown in Figure 2.7. Although not indicated, the detector geometry may include a filter that NRF-energy photons have a probability, $P_f(E_\gamma)$, to penetrate.

For simplicity, we neglect photon down-scatter. Then $\Phi(E, \mathbf{r})$ only varies due to the attenuation of photons,

$$\Phi(E, x) = \Phi_i \exp[-\mu(E)x] \tag{2.20}$$

and $\mu(E)$ now contains both resonant and non-resonant contributions,

$$\mu(E) = \mu_{nr} + N\sigma_{\text{NRF}}(E) \tag{2.21}$$

Considering only photon energies near an NRF resonance, we may neglect the energy-dependence of the non-resonant attenuation coefficient, μ_{nr}. Likewise, the attenuation coefficient for NRF γ rays, $\mu(E_\gamma)$, is equal to μ_{nr}, because the nuclear recoil has made them non-resonant.

The distance the photon must traverse to leave the target is given by $r_o = x/cos(\theta)$, where θ is the angle between the interrogating photon trajectory and the direction of the detector's location. The detector's surface area is assumed to be given by A.

Substituting, the rate of detection of full-energy NRF γ rays can be written as

$$\frac{d^2R_{\text{NRF}}}{dxdE} \approx \exp\left[-\left(\mu_{nr}[1 + 1/cos(\theta)] + N\sigma_{\text{NRF}}(E)\right)x\right] N\Phi_i\sigma_{\text{NRF}}(E)W_e(\theta)\frac{A\epsilon P_f E_\gamma}{4\pi r_d^2} \tag{2.22}$$

We define

$$\alpha = \mu_{nr}[1 + 1/\cos(\theta)] \tag{2.23}$$

and $\mu_{\text{NRF}}(E) = N\sigma_{\text{NRF}}(E)$ and obtain

$$\frac{dR_{\text{NRF}}}{dE} = \int_0^t \frac{d^2R_{\text{NRF}}}{dxdE}dx \approx \frac{1 - \exp[-(\alpha + \mu_{\text{NRF}}(E))t]}{\alpha + \mu_{\text{NRF}}(E)} N\Phi_i\sigma_{\text{NRF}}(E)W_e(\theta)\frac{A\epsilon P_f(E_\gamma)}{4\pi r_d^2} \tag{2.24}$$

If we further approximate that

$$\sigma_{\text{NRF}}(E) \approx \begin{cases} 0, & \text{if } E < E_C - \Gamma_D/2; \\ \sigma^C_{\text{NRF}}, & \text{if } E_C - \Gamma_D/2 \leq E \leq E_C + \Gamma_D/2; \\ 0, & \text{if } E > E_C + \Gamma_D/2. \end{cases} \tag{2.25}$$

where

$$\sigma^C_{\text{NRF}} = \frac{\int \sigma_{\text{NRF}}(E)dE}{\Gamma_D} \tag{2.26}$$

E_C is the centroid energy of the resonance, and Γ_D is given by equation 2.8. We may integrate equation 2.24 to obtain

$$R_{\text{NRF}} \approx \frac{1 - \exp[-(\alpha + N\sigma^C_{\text{NRF}})t]}{\alpha + N\sigma^C_{\text{NRF}}} [N\Phi_i \sigma^C_{\text{NRF}}] \frac{W_e(\theta)A\epsilon P_f(E_\gamma)}{4\pi r_d^2} \tag{2.27}$$

Equation 2.27 is arranged such that the expected rate at which NRF γ rays are detected is divided into contributions due to three phenomena, the first term is due to the effective geometric attenuation of photons before and after NRF. A more complex derivation of this term for non-trivial geometries uses a simple finite element integrating routine. The second term, $N\Phi_i\sigma^C_{\text{NRF}}$, is the rate (per unit thickness) at which NRF would occur in the target without any attenuation, and the final term is due to the probability of detection of NRF γ rays emitted from the target.

Although the constant cross section approximation of equation 2.25 will prove to be very flawed in analysis of transmission assay, the assumption that the solid angle subtended by the detector is independent of the interaction location within the target proves to be the largest approximation in many backscatter NRF assay geometries.

2.4.2 Transmission Assay

2.4.2.1 NRF and Background Signal Rates

Photons penetrating the fuel assmbly undergo attenuation given by

$$\Phi(E) = \Phi_0(E) \exp[-\mu(E)x] \tag{2.28}$$

where x is the thickness of the assembly material the photon penetrates, and $\mu(E)$ is the energy-dependent attenuation coefficient for photons in the assembly material, given by

$$\mu(E) = \sum_{ij} N_i \sigma_{ij}(E) \tag{2.29}$$

where N_i is the number density of a given isotope, i, and $\sigma_{ij}(E)$ is the partial cross section for a photon interaction event of type j for that isotope (i.e., incoherent scattering, pair production, NRF, ...). There is also the potential for higher-energy photons to be down-scattered to the energy, E, resulting in higher photon fluences than indicated by equation 2.28. The phenomenon of notch refill, where a down-scattered photon becomes resonant in energy is discussed in more detail in Section 3.3.3. For the case where the energy of an NRF resonance is near the maximum energy of the interrogating photon spectrum, this occurrence is relatively rare. However, down-scattering

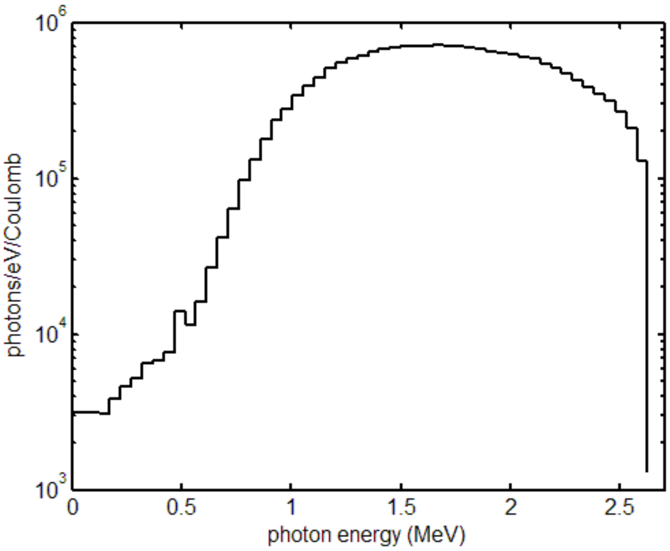

Figure 2.8 Calculated spectrum of photons leaving a fuel assembly in the direction of a witness foil located 150 cm downstream from the assembly. The incident photon spectrum was 2.6 MeV endpoint energy bremsstrahlung, similar to that shown in Figure 2.5, except the source collimation was assumed to be 1° .

significantly increases the photon flux for the low-energy portion of the transmitted spectrum, relative to that predicted by equation 2.28.

We consider non-resonant photon transport through a target composed of UO_2, Zr, and small quantities of other actinides and fission products. The target geometry is a homogenized mixture of these constituents at 4 g/cm^3 density and 21.8 cm square, which is the homogenized equivalent of a 17 pin by 17 pin (17x17) spent fuel assembly. Expected photon intensities are estimated with MCNPX simulations, where the effects of resonant absorption are explicitly excluded. Resonant absorption is calculated separately using the formalisms developed below in this section.

The bremsstrahlung spectrum used in this simulation to irradiate the target is shown in Figure 2.5. The conversion target is assumed to be 150 cm from the side face of the homogenized fuel assembly target. The geometry is such that the diameter of the un-scattered beam is 21.8 cm at the back plane of the target. The spectrum of photons leaving the target's back plane in the direction of the TD is shown in Figure 2.8. The integrated flux is attenuated by a factor of $\sim$400, however, photons above 2 MeV are only attenuated by a factor of $40 - 50$.

The transport of the photons through and scattered off the TD are simulated in a next step. The energy-differentiated photon flux was calculated at a point 100 cm from the TD at an angle of 120°, relative to the initial beam direction. This photon energy distribution is then taken as the source spectrum for a final series of simulations in which the shielded detector response is examined. In these simulations, the thickness of the Pb filter was varied, and for each incident photon, the energy deposited within the germanium was calculated, resulting in the expected measured photon spectrum.

The thicknesses of the Pb filters were 1.27, 2.54, 4, 6, and 8 cm for these simulations. Going from a filter thickness of 1.27 cm to 8 cm, the total count rate in the detector (100% relative efficiency HPGe) decreases from 4.4×10^7 to 1.2×10^5 counts per Coulomb of 2.6 MeV electrons incident upon the bremsstrahlung converter. In general, an HPGe detector should operate at a

Table 2.3 Effects of the photon filter on the photon spectrum that is calculated to be measured by a 100% relative efficiency HPGe detector. $x_{\rm f}$ indicates the thickness of the Pb filter. The values corresponding to 'counts per 2.6 MeV e^-' indicate the total number of expected counts per 2.6 MeV electron incident upon the bremsstrahlung converter, and from these values, the electron beam intensity resulting in 2×10^4 counts per second, I_{max}, is calculated. Values labeled as $I_\gamma/I_{\gamma 0}$ indicate the attenuation of a 2.25 MeV γ ray as it penetrates through the corresponding filter thickness.

$x_{\rm f}$ (cm)	counts per 2.6 MeV e^-	I_{max} (mA)	$I_\gamma/I_{\gamma 0}$
1.27	7.0×10^{-12}	0.46	0.53
2.54	1.8×10^{-12}	1.8	0.28
4.0	4.1×10^{-13}	7.8	0.14
6.0	7.6×10^{-14}	42	0.051
8.0	1.9×10^{-14}	170	0.019

maximum of between 2×10^4 and 8×10^4 Hz[21]. Using 2×10^4 as a conservative nominal maximum count rate, the maximum allowable beam current for a given filter thickness is determined. These values are summarized in Table 2.3.

Increasing the filter thickness results in more attenuation of the NRF γ rays. This decreases the probability that a NRF γ ray will deposit its full-energy in the HPGe detector. This attenuation is estimated with the expression $I = I_O \exp(-\mu x_f)$, where μ is the attenuation coefficient (without coherent scattering) taken from reference[22]. The attenuation due to the filter, $I_\gamma/I_{\gamma 0}$, is also shown in Table 2.3 for a 2.25 MeV γ ray. Attenuation coefficients are not a strong function of energy in the range between 2 and 2.5 MeV, and therefore we can consider these values to be fairly representative of the behavior NRF γ rays that would be induced by a 2.6 MeV endpoint-energy bremsstrahlung beam.

2.4.2.2 Analytical Considerations

In this section we discuss the analytical model that relates the areal density of the IOI in the target to the decrease in the intensity of the NRF γ rays measured by radiation detectors in the transmission geometry. We consider the relative attenuation of photons at, and near, resonant-energies through materials containing varying amounts of an isotope of interest. As discussed in Section 2.1.2, the energy-dependent cross section that photons experience while traversing a material is given to an excellent approximation by the Doppler-broadened Lorentzian profile (DBLP) described in equation 2.10. The relative probability that a photon at or near resonant-energy traverses the assay target and then subsequently undergoes NRF in the TD is calculated. In Section 2.5 the expected NRF probabilities are compared to alternate predictions that would result if approximate models of the energy-dependent cross section were used.

First, we assert that within a few eV of a resonance, it is valid to approximate all non-resonant cross sections as constants and this approximation is accurate to a fraction of a percent[22]. Likewise, across the width of a resonance the change in intensity of bremsstrahlung-spectrum photons may be neglected. With this, the energy-differentiated photon flux, $\Phi_i(E)$, incident upon the assay target is assumed constant and effects due to non-resonant photon attenuation are separated. Neglecting down-scattering, the effective photon flux leaving a target is approximately

$$\Phi_o(E) \approx \Phi_i \exp[-N\sigma_{\text{NRF}}(E)x] \exp\left[-\mu_{\text{atom}}x\right] \tag{2.30}$$

where N is the atom density of a Pu isotope (in units of atoms/cm^3) in the assembly, x is the target thickness (that is determined by a ray-tracing algorithm), $\sigma_{\text{NRF}}(E)$ is the cross section due to NRF, and μ_{atom} is the attenuation coefficient for photons in the assay target due to non-resonant processes (assumed to be constant over the energy range of interest).

The rate at which NRF γ rays emitted into backward angles relative to the direction of the NRF-inducing incident beam are counted and was considered in Section 2.4.1.1 for a slab target. The only difference here is that the incident photon flux is now $\Phi_o(E)$.

$$\frac{dR_{\text{NRF}}}{dE} \approx \frac{1-\exp[-(\alpha+\mu_{\text{NRF}}(E))t_{\text{TD}}]}{\alpha+\mu_{\text{NRF}}(E)} N_{\text{TD}}\Phi_o(E)\sigma_{\text{NRF}}(E)W_e(\theta)\frac{A\epsilon}{4\pi r_d^2} \tag{2.31}$$

where t_{TD} refers to the TD thickness and α is defined in equation 2.23.

Equation 2.31 may be re-written as follows

$$\frac{dR_{\text{NRF}}}{dE} = \lambda(E)\Big[\exp[-N\sigma_{\text{NRF}}(E)x]\sigma_{\text{NRF}}(E)\Big]\left[N_{\text{TD}}\Phi_i \exp(-\mu x)W_e(\theta)\frac{A\epsilon}{4\pi r_d^2}\right] \tag{2.32}$$

The first term,

$$\lambda(E, t_{\text{TD}}) = \frac{1-\exp[-(\alpha+\mu_{\text{NRF}}(E))t_{\text{TD}}]}{\alpha+\mu_{\text{NRF}}(E)} \tag{2.33}$$

is an effective thickness that a photon experiences as it traverses the slab. If the quantity $\alpha + \mu_{\text{NRF}}(E)$ is small,

$$\lambda(E, t_{\text{TD}}) \approx t_{\text{TD}} \tag{2.34}$$

Indicating that the rate of NRF γ ray detection would be directly proportional to the TD thickness. However, for geometries containing a thick TD or if larger photon interaction probabilities are present, the rate at which NRF is induced in the slab is less than $N_{\text{TD}}\sigma_{\text{NRF}}t_{\text{TD}}$ because $\lambda(E) \leq t_{\text{TD}}$.

We define the first two terms of equation 2.32 as $\Lambda(E, t_{\text{TD}}, Nx)$,

$$\Lambda(E, t_{\text{TD}}, Nx) \equiv \lambda(E)\Big(\exp[-N\sigma_{\text{NRF}}(E)x]\sigma_{\text{NRF}}(E)\Big) \tag{2.35}$$

This function contains all the parameters that can significantly vary over an energy range comparable to the Doppler-broadened width of an NRF resonance. The energy resolutions of all commonly used γ-ray detectors are much wider than the width of an NRF resonance. Therefore energy-dependent variations in Λ will not be directly observed in the detected photon energy spectrum and the quantity $\int \Lambda(E)dE$ provides a quantity that is proportional to the rate at which NRF counts will be measured.

The measured quantity that provides information on the areal density of the IOI in the sensitive volume of the assay target is the reduced rate of NRF γ-ray counts, relative to those expected for a comparable assay target with none of the IOI present. This quantity is called the *effective attenuation* and is given by

$$\mathbb{A}(t_{\text{TD}}, Nx) \equiv \frac{\int \Lambda(E, t_{\text{TD}}, Nx)dE}{\int \Lambda(E, t_{\text{TD}}, 0)dE} \tag{2.36}$$

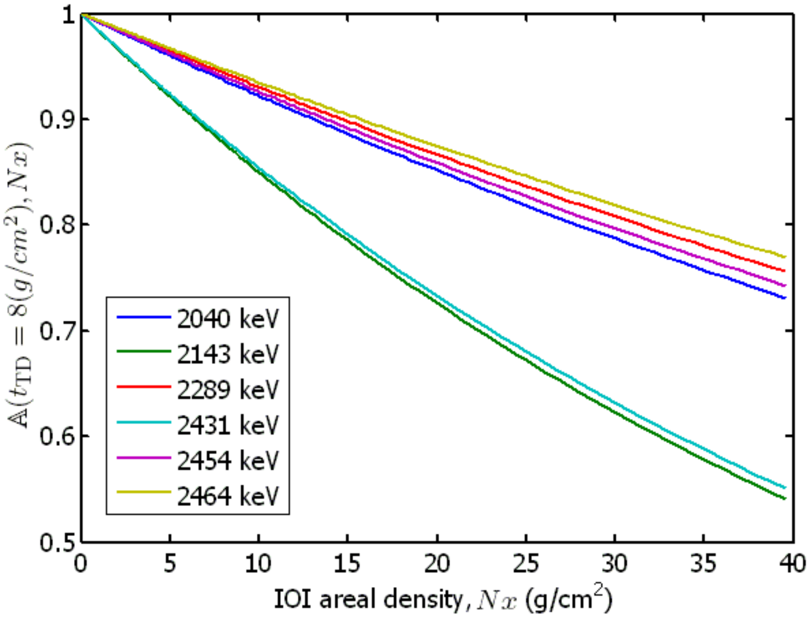

Figure 2.9 The effective attenuation of photons given by equation 2.36 due to ^{239}Pu NRF resonances with $t_{\mathrm{TD}} = 8$ g/cm^2. Data for the resonances are shown in Table 3.3 and are from reference [23]. Each resonances is indicated by its centroid energy in the legend.

The effective attenuation is dependent upon the parameters of the resonance it describes. Effective attenuation functions are shown for different ^{239}Pu resonances when $t_{\mathrm{TD}} = 8$ g/cm^2 in Figure 2.9. The parameters of the known ^{239}Pu NRF resonances are shown in Table 3.3. Figure 2.9 indicates that for a target of constant total areal density, but increasing Pu areal density, NRF γ-ray count rates decrease. The rate at which they decrease is proportional to the width of the resonance. By observing this reduced rate, the areal density of the Pu isotope is measured.

$\Lambda(E, t_{\mathrm{TD}}, Nx)$ and therefore $\mathbb{A}(t_{\mathrm{TD}}, Nx)$ are functions of t_{TD}. The thin TD sheet approximation can result in significant errors (30% of $\mathbb{A}(t_{\mathrm{TD}}, Nx)$) when a thick sheet is used to measure targets with significant resonant attenuation. These effects however, appear predictable and are less severe when $\mathbb{A}(t_{\mathrm{TD}}, Nx)$ is nearer unity.

2.5 Approximate NRF Cross Section Models

In the previous section it was implicitly assumed that all resonances take the Doppler-Broadened Lorentzian Profile (DBLP) given in equation 2.10. However, approximate forms of the DBLP are often assumed. The NRF data added to MCNPX and ENDF files as described in Section 3.2 uses one such approximation.

The forms considered for resonance shapes are:

- a Maxwell-Boltzmann profile of equationwith width, Δ, given by equation 2.9;
- a point-wise evaluation of the Maxwell-Boltzmann distribution with linear interpolation between points. The energies at which the Maxwell-Boltzmann distribution was evaluated are the centroid energy, E_C and $E_C \pm 2$ eV and $E_C \pm 4$ eV; and

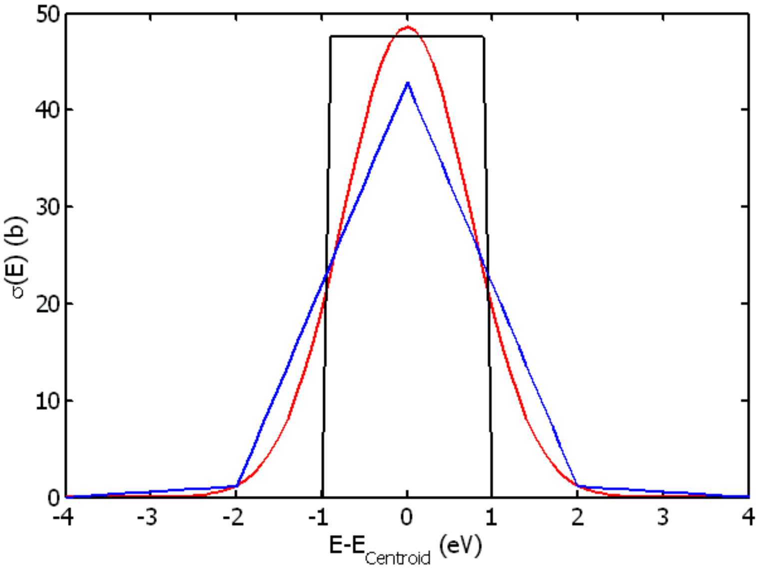

Figure 2.10 Model forms of the resonance cross section profile. Width and total cross section values are from the 2209 keV resonance of ^{238}U. Red = Maxwell-Boltzmann, Blue = point-wise, and Black = step function.

- a step increase and decrease as defined in equation 2.25.

The cross section from each model is normalized such that the integrated cross section is the same as that of the natural cross section. These functional forms with shape parameters due to the 2209 keV resonance of ^{238}U[24] are shown in Figure 2.10.

The differing approximate forms of the cross section profile result in calculated values of $\mathbb{A}(t_{\mathrm{TD}}, Nx)$ that may differ by up to 5% for ^{239}Pu isotopic areal density found in spent fuel. The largest disagreement, results from the use of the constant cross section approximation. Use of the Maxwell-Boltzmann profile or its point-wise evaluation will generally produce less than 1% errors for ^{239} areal densities. However, the transmission experiment described in Section 4 involved significantly larger areal densities, and therefore careful consideration of the forms of the resonances was necessary.

2.6 Measurement Sensitivity

The research reported here aims at determining the feasibility of using NRF for NDA in safegaurds. This is discussed explicitly for SNF assay, measurement of uranium enrichment, and MOX fuel assay in Section 5. The core question is what measurement sensitivity, i.e., precission and accuracy, can potentially be achieved. The many contributing factors that were considered include interrogating photon source, interrogating photon flux, measurement technique (backscatter vs transmission), detector filter thickness, detector energy resolution, transmission target thickness, backscatter angle of the detectors, and measurement time. The challenge for a precise measurement of a small concentration of Pu isotopes in SNF comes from accruing the necessary counting statistics because the integrated resonance cross sections are relatively small. Using the backscatter detection method, the NRF peaks are difficult to precisely measure on the much larger background. In the transmission technique only a small change in the NRF peak intensity is observed. In order to achieve practical measurement times, a new generation of high-intensity photon sources and efficient detection systems, as discussed in the following sections of the report, are needed.

2.6.1 Measurement Precision and Counting Statistics

In this section, we relate counting statistics to the measurement precision of the areal density of the IOI in the sensitive volume. The relationship between statistical uncertainties in the effective attenuation of resonant photons and the uncertainty of the areal density is derived for cases where the concentration of the IOI is low such as ^{239}Pu in spent fuel. Finally, a generalization between the strength of a resonance and the relative statistical uncertainty a measurement of this resonance would provide is made for low-attenuating assay targets.

Assume there exists a function for each NRF resonance, $f(Nx) \equiv C$ that relates the number of full-energy NRF γ-ray counts, C, to the areal density of the IOI in the target, Nx. Nx is then given by

$$Nx = f^{-1}(C) \tag{2.37}$$

Likewise, uncertainty in Nx can be written as

$$\sigma_{Nx} = \left| \frac{df^{-1}}{dC} \right| \sigma_C \tag{2.38}$$

Neglecting down-scatter of photons while they penetrate the assay target and the TD, the expected number of γ-ray counts, C, due to NRF in the TD may be expressed as

$$C \equiv f(Nx) = c_t \Phi_0 \exp(-\mu_{\text{atom}} x) \mathbb{A}(Nx) N_{\text{TD}} \sigma_{\text{NRF}} \frac{P_f \epsilon \Delta\Omega}{r_{det}^2} \tag{2.39}$$

where c_t is the duration of the measurement and all remaining terms have been defined in preceding sections. Only $\mathbb{A}(Nx)$ in equation 2.39 is dependent upon N, the density of the IOI in the assay target. We re-express $f(Nx)$ as,

$$f(Nx) = \chi \mathbb{A}(Nx) \tag{2.40}$$

where

$$\chi \equiv c_t \Phi_0 \exp(-\mu_{\text{atom}} x) N_{\text{TD}} \sigma_{\text{NRF}} \frac{P_f \epsilon \Delta\Omega}{r_{det}^2} \tag{2.41}$$

χ represents the number of NRF γ-ray counts that are expected to be measured from the TD in the absence of IOI atoms in the assay target.

The function, $f(Nx)$ is therefore directly proportional to $\mathbb{A}(Nx)$, the effective attenuation. Unfortunately, the functional form of $\mathbb{A}(Nx)$ is somewhat complex, and it cannot be analytically differentiated.

Figure 2.9 shows $\mathbb{A}(Nx)$ for ^{239}Pu resonances and a TD thickness of 8 g/cm^2 of ^{239}Pu. Stronger resonances result in functions of $\mathbb{A}(Nx)$ with a steeper slope at lower areal densities and then flatten for higher values of Nx.

To obtain an analytically differentiable function that approximates $f^{-1}(C)$, We consider a fit to $\mathbb{A}(Nx)$ of the form

$$\mathbb{A}(Nx)_{\text{fit}} = \exp(-\alpha_f Nx) \tag{2.42}$$

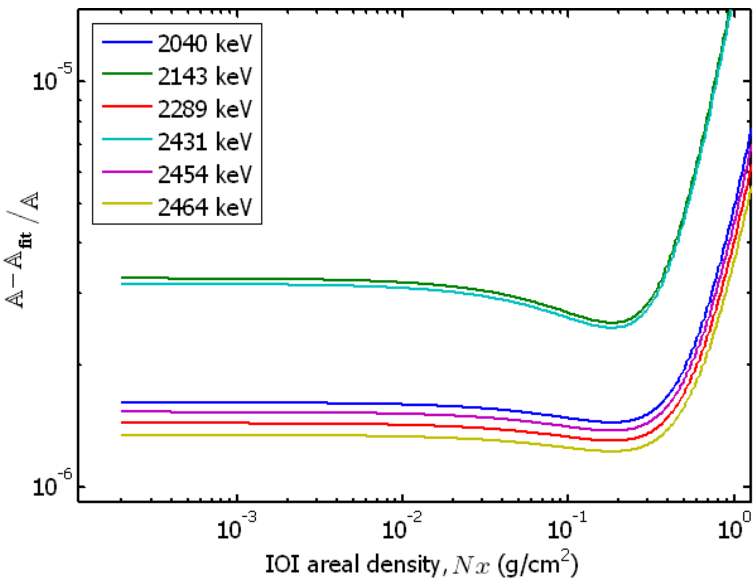

Figure 2.11 Fraction deviation between calculated values of $\mathbb{A}(Nx)$ and those resulting from the best-fit of the form shown in equation 2.42.

for the range $Nx \leq 0.5$ g/cm^2, which is approximately the range of areal densities encountered for spent fuel assemblies[2]. Comparisons between fits of this form and $\mathbb{A}(Nx)$ are shown for ^{239}Pu resonances in Figure 2.11. The fit is quite good over the fitted range, but becomes quite poor for higher Nx. Best-fit values of α_f for each ^{239}Pu resonance are shown in Table 3.3 along with measured resonance parameters from reference[23].

Considering only the cases where $Nx \leq 0.5$ g/cm^2 and using

$$f(C) \approx \chi \exp(-\alpha Nx) \tag{2.43}$$

we can write

$$f^{-1}(C) \approx \frac{\ln \chi - \ln C}{\alpha} \tag{2.44}$$

and

$$\frac{df^{-1}}{dC} = \frac{-1}{C\alpha} \tag{2.45}$$

Using equation 2.15, which relates the statistical precision of a γ-ray counting measurement to the ratio of signal-to-background intensities, ξ, and substituting equation 2.45 into equation 2.38, we have

$$\sigma_{Nx} = \frac{\sqrt{1+2/\xi}}{\alpha\sqrt{C}} \tag{2.46}$$

This relates the precision with which Nx is measured to both counting statistics and the quantity α, which is the magnitude of the slope of the effective attenuation curve at the corresponding areal density.

---

[2] A fit of the form $\mathbb{A}(Nx)_{\text{fit}} = a_1 \exp(a_2 Nx) + a_3 \exp(a_4 Nx)$ provides quite good agreement over a much larger range of areal densities ($\leq 2 \times 10^{-6}$ error fraction for $Nx \leq 30$ g/cm^2), but it also does not provide an analytical form for $df^{-1}(C)/dC$.

From equation 2.46, we can infer that large resonances will provide the smallest statistical errors when the IOI areal density in the target is small, as is the case for measuring Pu in spent fuel assemblies. These models are applied to the evaluation of measurement methods using bremsstrahlung and quasi-monoenergetic photon sources. In Section 5.1.1.2 the numerical results presented there demonstrate that counting statistics are a main limitation for NRF measurements.

2.6.2 Importance of Resonance Strength for Transmission Measurements

To illustrate the importance of the resonance strength for providing precise measurements of target areal densities, we consider a case where Nx is still assumed to be small (i.e. where equation 2.42 remains valid), and compare two hypothetical resonances, a and b. Assume these resonances have widths, Γ_a and Γ_b, respectively, and that $\Gamma_a > \Gamma_b$. The relative uncertainties in areal density that transmission measurements made using resonance a will be reduced by at least

$$\frac{\sigma_a}{\sigma_b} \approx \left(\frac{\Gamma_b}{\Gamma_a}\right)^{1.5-2} \tag{2.47}$$

relative to an identical measurement using resonance b. This is the combination of three factors. First, stronger resonances result in proportionally higher NRF count rates, which, reduces the uncertainty by a factor of $\left(\frac{\Gamma_b}{\Gamma_a}\right)^{1/2}$. Also, stronger resonances increase the slope of the effective attenuation function, α, which result in a relative decrease in uncertainty of approximately $\left(\frac{\Gamma_b}{\Gamma_a}\right)$. Finally, for NRF signals not significantly stronger than background intensity, the term $\sqrt{1+2/\xi}$ in equation 2.46 can contribute an additional factor of up to $\left(\frac{\Gamma_b}{\Gamma_a}\right)^{1/2}$.

The strong dependence of measurement precision on resonance strength could make it easier to measure the ^{240}Pu content in spent fuel than the ^{239}Pu areal density. Although the NRF response of ^{240}Pu has not been measured, NRF cross sections are likely comparable to those of ^{238}U and thus much higher than ^{239}Pu ones.

2.6.3 Systematic Errors

The systematic errors that may be associated with NRF measurements include the following: Errors in NRF cross sections result in proportionally inaccurate measurements. Notch refill may reduce the intensity of measured resonant absorption in a transmission measurement, relative to the predicted by simple analytical models, and will result in systematic errors, without precise models that account for it. Overlap of other γ ray peaks (other NRF lines or background) can significantly reduce the precision with which the intensity of a resonance may be measured. The photon flux that induces NRF must be precisely known. This may be accomplished by system calibration as long as the beam remains stable. If this method is used, beam instability becomes an important contributor to systematic error. If the flux is determined by an alternative normalizations scheme, such as the 511 keV normalization routine, or by making relative measurements to other NRF lines, beam stability may be less important, however such routines may result in separate systematic errors. Similarly, the uncertainty to which the γ-ray detectors are calibrated will proportionally induce errors for absolute measurements, but relative measurements made on well-calibrated systems will be less sensitive to absolute knowledge of the γ-ray detection efficiency.

Similar to beam stability, detector stability becomes very important for calibrated systems. Radiation damage to the fuel pins may lead to deformations and may, thus, result in geometric differences between a measured assembly and the reference assembly. Although these are likely to be small, non-negligible systematic errors may result. Likewise, the uncertainty to which non-resonant attenuation coefficients are known will adversely effect the precision at which geometric effects may be corrected for in relative and absolute measurement schemes.

Model calculation corrections can be applied to correct for notch refill and possibly peak overlap. Improved measurements of NRF cross sections using newer and more intense bremsstrahlung sources are necessary. Other systematic errors can be addressed and minimized through calibration which is expected to be necessary for any measurement system.

3 MCNPX Modeling - Simulation of Non-Resonant Background

We have used the MCNPX code extensively to study the use of NRF. MCNPX was used to generate bremsstrahlung spectra, simulate photon transport in both the backscatter and transmission geometries, test the analytical models derived to compute NRF fluences in Sections 2.4.1 and 2.4.2, and to test the effect of notch refill.

It became evident in our initial study of NRF for spent fuel assay that MCNPX needed additional capabilities to become a useful tool for modeling NRF responses and background. Critical to this effort, we have added existing NRF data to the MCNPX photonuclear data files and are now able to include NRF physics into MCNPX simulations. During the modeling studies, it was also recognized that MCNPX does not accurately calculate photon elastic scatter that is the dominant contributor to the background at backward angles in the NRF energy range. This can be seen in Figure 3.1 which shows the simulated photon spectrum scattered off a uranium pin (^{238}U with 1% ^{235}U) at a backwards angle of 135°. At photon energies close to the bremsstrahlung end point energy the photon flux was underestimated by an order of magnitude or more before MCNPX was modified to properly sample the ENDF libraries when simulating Rayleigh Scattering. The nuclear Thomson scattering, Delbruck scattering, and Giant Dipole Resonance (GDR) are still neglected by MCNPX. The modification of the photon transport routines used by MCNPX and the reconstruction of the photo-atomic datafiles used by MCNPX to include extended descriptions of the form factors for the elastic photon scatter process are described in more detail in Appendix A. The potentially important photonuclear processes nuclear Thomson scattering , Delbruck scattering, and Giant Dipole Resonance (GDR) were not included and their potential contributions are discussed in this section.

3.1 MCNPX Simulations of Photon Scattering

Below we discuss the MCNPX computations of the combination of the photon scattering processes and the effective scattered spectrum that results.

3.1.0.1 Scattering of Monoenergetic Photons as Simulated by MCNPX

In many regards this section is a continuation and elaboration on work previously done by Hagmann and Pruet[67], with the additional inclusion of Rayleigh scattering, which had previously been omitted due to legacy MCNP coding. Figure 3.2 shows spectra computed by MCNPX, where monoenergetic photons interact in a 100 μm thick uranium target and are scattered into solid angles defined by an angle relative to the incident photon trajectory. The spectra have 5 general features;

- A peak in the highest energy bin, corresponding to elastic scattering. As discussed in Appendix A, the intensity of this peak is due primarily to Rayleigh scattering – as is described in EPDL97 – and is missing nuclear elastic scattering contributions. The integrated area

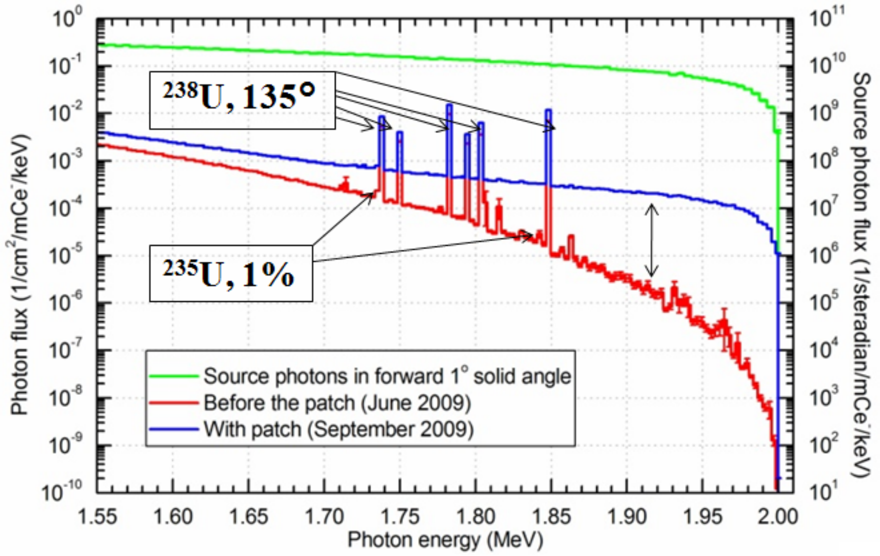

Figure 3.1 The red curve shows the simulated spectrum before implimintation of the Rayleigh scattering patch. The blue curve shows the simultated spectrum with the patch. The green curve is the Bremsstrahlung source photon spectrum.

of the elastic scattering peak is very small compared to the remainder of the photon spectrum, which illustrates the relative unimportance of the elastic backscattering of photons for applications less sensitive to backscattered photon spectra than NRF.

- A peak at 511 keV due to annihilation of positrons produced during pair production. The 511 keV photons are emitted isototropically.
- An incoherent photon peak. The energy of this peak is defined by Compton scatter kinematics. It ranges from near the incident photon energy for small-angle scattering to $\left(\frac{E}{1+2E/m_ec^2}\right)$ in backwards directions.
- x rays resulting from photoabsorption, which extend up to 109 keV for uranium.
- A spectral continuum that is primarily due to bremsstrahlung produced by electron and positron slowing down in the targets. Energetic electrons and positrons are produced by pair production, incoherent scattering, and photoelectric absorption.

The bremsstrahlung spectra due to these three electron sources have been included in Figure 3.2. The similarity of the distributions indicates that the simple model describes the continuum fairly well. With the exception of the energy range 1.4 - 1.55 MeV, the model provides good agreement with the overall spectrum at higher energies. Between 1.4 and 1.55 MeV, the assumption that all electrons are forward-directed, along with the neglect of electrons from multiple-scattered photons is rather inaccurate. At lower energies, many more processes appear to contribute to the photon spectrum, including multiple scattering of photons and bremsstrahlung from lower-energy Compton electrons.

From these scattered photon spectra, we can conclude that the most probable processes resulting in backscattered photons are incoherent scattering, pair production, and x ray emission.

However, the energies of these photons are quite low. MCNPX predicts that backscattered, energetic photons are primarily due to bremsstrahlung from energetic photo-excited electrons, but the contribution due to Rayleigh scattering is not negligible, and dominates near the initial photon energy. This implies that the accuracy with which MCNPX calculates bremsstrahlung spectra is important for predicting backscattered photon spectra and that the omission of other elastic scattering physics processes may be very problematic for making conclusions based on MCNPX-predicted spectra.

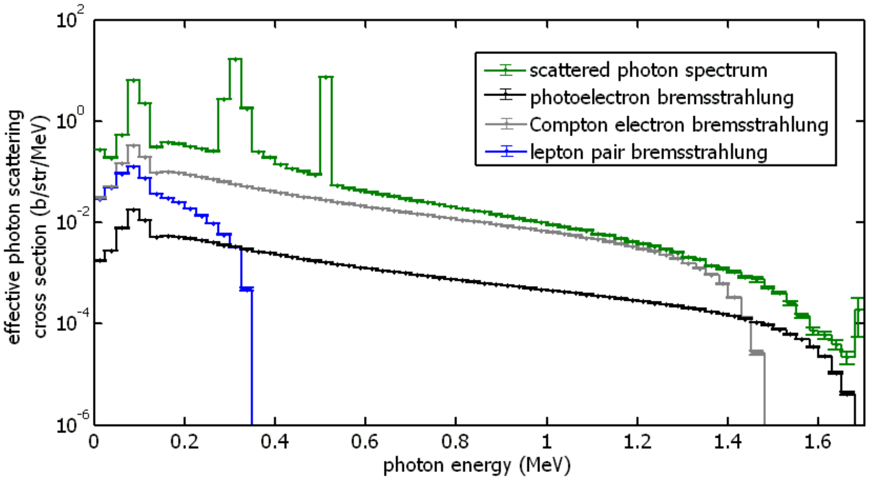

Figure 3.2 MCNPX-simulated differential cross section for scattering of 1.7 MeV photons from 100 μm thick uranium to the $100^{\mathrm{o}} - 110^{\mathrm{o}}$ angular range with electron induced bremsstrahlung spectra overlain.

3.1.1 Photonuclear Interactions

Here we consider photon interactions with the nucleus that are not included in MCNP but are a possibly significant contribution to the elastically scattered background. Both, photon scattering via off-resonant nuclear states and elastic scattering due to the electromagnetic field, are of interest.

Nuclear Thomson and Delbrück scattering are two examples of elastic scattering in the field of the nucleus. Pair production also involves photons interacting with the nuclear field, except the resulting particles are leptons instead of photons.

An additional complication is the effects of wave function phase shifts on total elastic scattering cross sections. For elastic photon scattering, the scattering amplitudes of each mechanism must be summed before the total scattering cross section is obtained by squaring the summed amplitude. This can cause interference due to differences in the complex phases of amplitudes resulting from different scattering mechanisms.

3.1.1.1 Nuclear Thomson Scattering

The typical nuclear Thomson scattering cross section is independent of photon energy and is given by

$$\sigma_{NT}(\theta) = \frac{r_e^2}{2}\left(\frac{Z^2 m_e}{A M_n}\right)^2 (1+\cos^2\theta) \qquad (3.1)$$

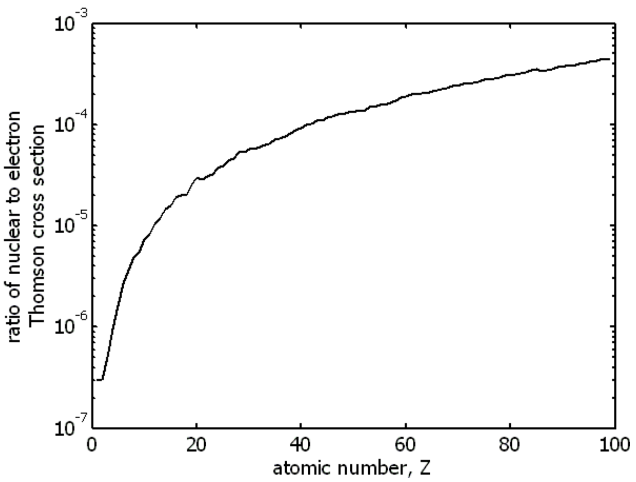

Figure 3.3 Ratio of Thomson scattering cross sections for a photon incident upon a nucleus of charge Zq_e and mass AM_n to that for a photon incident upon a free electron. The ordinate is the square of the constants in the parentheses in equation 3.1.

where r_e is the classical radius of the electron, m_e is the mass of the electron, θ is the scatter angle, and A, Z, and M_n are the atomic number, mass number, and average nucleon mass, repectively[61]. Figure 3.3 shows the ratio of the constants in the parentheses in equation 3.1 plotted for every element. Although the cross section is isotope-specific, in this case each element's mass was taken to be the weighted mean mass for a natural isotopic concentration. For man-made elements, the mass was assumed to be the average of the known isotopes' masses. Thomson scattering cross sections for nuclei vary from 3×10^{-7} to almost 4×10^{-4} of those of a single electron as Z increases from 1 to 92. While this seems to indicate that nuclear Thomson scattering would never be of any significance, it is important to note that for large-angle scattering, the momentum transfer, q, increases with scattering angle and energy. The form factor decreases dramatically with increasing q and the Rayleigh scattering cross section is proportional to the square of the form factor.

In Table 3.1, values of q and the corresponding Rayleigh scattering form factors, $F(Z,q)$, for which the Rayleigh scattering cross section is equal to the nuclear Thomson scattering cross section, i.e

$$\frac{Z^2 m_e}{AM_n} = F(Z,q) \tag{3.2}$$

are tabulated. Also tabulated are photon energies through which scattering at indicated angles yield indicated momentum transfer values.

As indicated in Table 3.1, the energy at which a nuclear Thomson cross section is equal to a Rayleigh scattering cross section increases with increasing Z. However, with larger scattering angles, the form-factor predictions of $\sigma_{Ray}(\theta)$ become increasingly inaccurate[48]. Thus, the energies given in Table 3.1 may be inaccurate, but the general trends remain correct. Furthermore, when photons of energy 1.5 - 4 MeV are backscattered, nuclear Thomson scattering is always of some practical importance.

element	q ($\mathring{A}^{-1}$)	$F(Z,q)$	$E(45^o)$ (MeV)	$E(90^o)$ (MeV)	$E(135^o)$ (MeV)	$E(180^o)$ (MeV)
Carbon	10.4	1.64×10^{-3}	0.337	0.182	0.140	0.129
Aluminum	19.2	3.34×10^{-3}	0.622	0.337	0.258	0.238
Iron	33.1	6.64×10^{-3}	1.07	0.580	0.444	0.410
Cesium	68.1	1.25×10^{-2}	2.21	1.19	0.914	0.844
Uranium	152.9	1.95×10^{-2}	4.95	2.68	2.05	1.90

Table 3.1 Elastic scattering momentum transfer, q, and form factors, $F(Z,q)$, (from EPDL97[42]) where $\sigma_{NT}(\theta) = \sigma_{Ray}(\theta)$ for different elements. Also tabulated are photon energies, that result in the given momentum transfers when scattering occurs at the indicated angles.

3.1.1.2 Delbrück Scattering

Delbrück scattering is the process by which a photon undergoes pair production within the Coulomb field of a nucleus, and the electron-positron pair promptly annihilates to create another photon whose energy is equal to the initial energy. Whereas Thomson scattering and pair production are considered to be second-order effects, Delbrück scattering is a fourth-order effect.

The matrix element for Delbrück scattering is given by[49]

$$\begin{aligned}\mathcal{A}_{fi} =& 2i\alpha \int d\mathbf{r_1} \int d\mathbf{r_2} \exp[i(\mathbf{k_1} \cdot \mathbf{r_1} - \mathbf{k_2} \cdot \mathbf{r_2})] \\ &\times \int dE_1 \int dE_2 \delta(\omega - E_1 + E_2) \mathrm{Tr}[\hat{e}_1 G(\mathbf{r_1}, \mathbf{r_2}|E_2) \hat{e}_2^* G(\mathbf{r_2}, \mathbf{r_1}|E_1)]\end{aligned} \tag{3.3}$$

where Tr signifies the trace of the indicated matrix, $\hat{e}_\mu = \epsilon_\mu \gamma^\mu$, γ^μ are Dirac matrices, and $G(\mathbf{r_a}, \mathbf{r_b}|E)$ are Green's functions in the Coulomb field. Calculations have exactly evaluated matrix elements in the limits $E \ll m_e c^2$ and $E \gg m_e c^2$ and by using the Born approximation at intermediate energies.

Matrix elements have been numerically integrated in the limit that $\hbar\omega \ll m_e c^2$[50]. Resulting scattering amplitudes are proportional to $(Z\alpha)^2$, and therefore cross sections are generally proportional to $(Z\alpha)^4$. Empirical evaluations indicate that the Born-series calculations remain quite accurate up to a few MeV if $Z \lesssim 50$. At higher Z, stronger fields make the lowest-order Born approximation inaccurate. Numerical calculations of higher-order terms in the Born series have only partially been accomplished for very few angles and energies[51],[52], but semi-empirical Coulomb correction factors have been published[49],[53],[54]. For uranium, these corrections can be a large fraction of the Delbrück differential scattering cross section, which, in turn can result in significant changes to the total theoretical elastic scattering cross section.

Figure 3.4 shows the sum of Delbrück scattering amplitudes squared for various photon energies. These would correspond to the Delbrück cross sections were they directly measurable. However, the addition of elastic scattering amplitudes from other processes can induce interferences that cause total scattering cross sections to differ from those predicted by summing cross sections of individual processes. The cross sections shown were calculated by high-precision numerical integration of the first-order Born series results[55],[56].

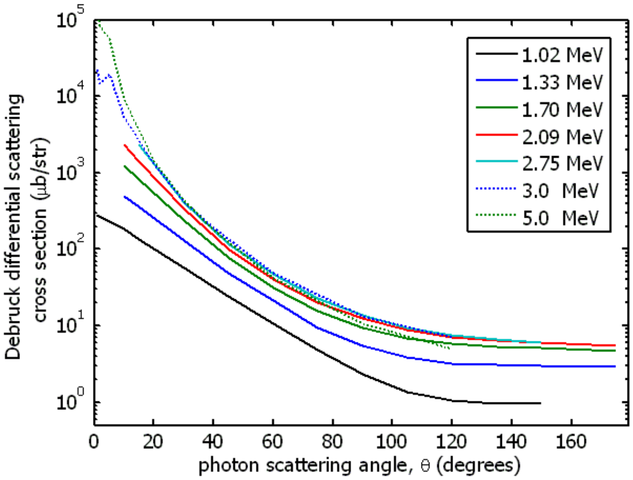

Figure 3.4 Calculated differential Delbrück scattering cross sections for various photon energies. The values ignore destructive interferences that reduce the summed cross section. Values are from references[55] except for the two highest energy curves, which are from[56].

3.1.1.3 Giant Dipole Resonance Scattering

For assay purposes and nuclear safeguards applications, we are concerned with specific excited states of relatively low energy. However, the primary strength of resonance photon scattering involves the Giant Dipole Resonance (GDR).

The GDR is described as a collection of excited nuclear states that all express a collective nuclear motion where all nuclear protons oscillate relative to the neutrons. The large number of such states effectively yields a broad resonance whose cross section is well-described as a Lorentzian distribution. For spheroidal nuclei, the energy associated with GDR oscillations depends on the mode of oscillation, resulting in two broad Lorentzian functions. The centroid energies of these resonances are approximately given by the following relation, which assumes the nuclear excitation energy of the GDR is due to increased surface area in a liquid-drop model of the nucleus[57],[58],[59].

$$E_{\mathrm{GDR}} \approx 77[\mathrm{MeV}]A^{-1/3} \tag{3.4}$$

GDR centroid energies are plotted as a function of mass number, A in Figure 3.5 along with the trend-line from equation 3.4. The trend-line holds well for spherical higher-A nuclei, whereas GDR centroid energies for spheroidal nuclei bifurcate into two bands. These bands can be explained as the symmetry breaking of the spheroidal nucleus, where vibrations along the axis of symmetry of prolate (oblate) spheroids are decreased (increased) in excitation energy relative to a sphere.

The total cross section for photo-excitation of the GDR collection of states, and subsequent de-excitation is most commonly given by the single- or double-Lorentzian form

$$\sigma_{\mathrm{GDR}} = \sum_{i=1}^{n} \sigma_i \frac{E_i^2 \Gamma_i^2}{E_i^2 \Gamma_i^2 + (E^2 - E_I^2)^2} \tag{3.5}$$

where n is the number of Lorentzian modes, 1 for spherical nuclei and 2 for spheroidal nuclei, Γ_i is the effective width of the mode, σ_i is the maximum cross section of the mode, and E_i is the centroid energy of the mode.

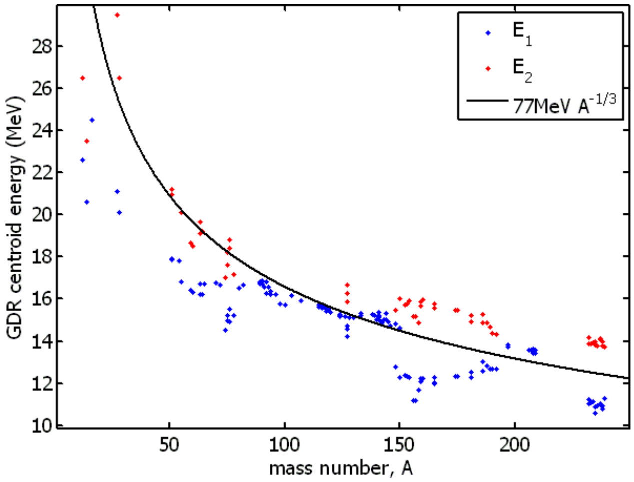

Figure 3.5 Giant Dipole Resonance Lorentzian distribution centroid energies, E_i, as taken from the RIPL-2 database (blue)[60]. For deformed nuclei, the GDR is described by two Lorentzian functions and the centroid energy of the upper Lorentzian is shown in red. The curve corresponds to a fluid-dynamics theoretical prediction of the centroid energies for spherical nuclei, and is given by equation 3.4.

The total cross section for photo-excitation of the GDR is then probabilistically subdivided into partial cross sections for each de-excitation mode that is energetically allowed. Charged particle emission, although often energetically allowed, does not significantly contribute to cross sections due to the Coulomb barrier for emission. The GDR centroid energies of all nuclei are greater than neutron separation energies, and the majority of the GDR cross section is due to neutron emission and fission, where possible. Neutron emission and fission can be accompanied by γ-ray emission to return the daughter nucleus or nuclei to their ground states. At lower energies, γ-ray emission is the most probable de-excitation mode. The large energy range over which the GDR extends causes the photon interaction cross section to remain non-negligible at these energies.

Figure 3.6 presents cross sections for elastic scattering of 1.5, 2.25, 3, and 5 MeV photons from GDR Lorentzians described in the RIPL-2 database[60]. GDR resonance profiles are also shown in Figure 3.7. The neutron-emission thresholds are indicated as the vertical lines.

Two important points arise from Figure 3.7. The first is that by increasing photon energy in the 1.5 to 4 MeV energy range and above, GDR cross sections increase. Thus, with increasing NRF lines energies, the photon background due to GDR scattering increases. Secondly, increasing photon energies yields more (γ,n) reactions as more neutron emission thresholds are exceeded. Thermal neutron-capture γ rays can be a major source of discrete background for NRF assay of materials.

3.1.2 Scattering Amplitudes and Cross Sections

To this point, all elastic photon scattering processes have been presented with the assumption that each may be considered independently of the others. This, however, is not the case. The amplitudes of all scattering processes that leave the state of the scattering atom unaltered and do not change the energy of the scattered photon must be summed to yield a total elastic scattering amplitude. Thus we write

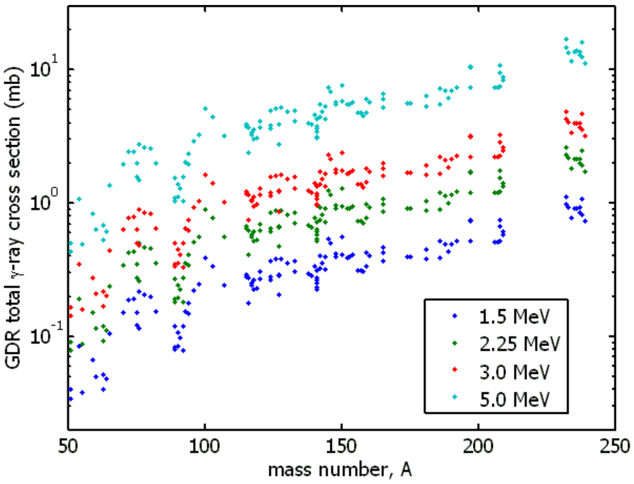

Figure 3.6 Photon cross sections due to lower-energy tails of GDRs as taken from the RIPL-2 database[60].

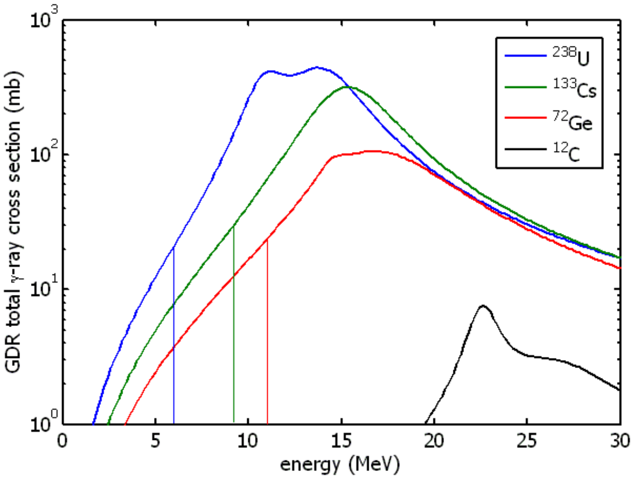

Figure 3.7 Giant Dipole Resonance Lorentzian Distributions for various isotopes[60]. The vertical lines indicate (γ,n) threshold energies, which correspond to dramatically decreased elastic scattering cross sections as the majority of GDR de-excitations begin to occur via neutron emission .

Data	**Reference**	**Quoted Accuracy**
Rayleigh	Kissel[45]	$< 5\%$
Delbrück	Falkenberg[55]	$\approx 20\%$
Nuclear Thomson	Ericson, Hufner[61]	$\approx 1\%$
GDR	RIPL2[60], Berman[62]	$< 30\%$

Table 3.2 Sources and accuracy of elastic scattering amplitude data and calculations.

$$A_{\mathrm{Coh}} = A_{\mathrm{Ray}} + A_{\mathrm{Del}} + A_{\mathrm{NT}} + A_{\mathrm{GDR}} \tag{3.6}$$

Likewise, scattering amplitudes are often derived assuming a given photon polarization. Thus, for linearly polarized photons with polarization perpendicular or parallel to the plane of scattering, $A_\perp$ and $A_\parallel$, respectively, the total scattering cross section is given by

$$\frac{d\sigma}{d\Omega} = \frac{1}{2}\left[|A_\perp|^2 + |A_\parallel|^2\right] \tag{3.7}$$

Amplitudes are often tabulated in units of the *reduced electron radius*, in which case the cross section would be given by

$$\frac{d\sigma}{d\Omega} = \frac{r_e^2}{2}\left[|A_\perp|^2 + |A_\parallel|^2\right] \tag{3.8}$$

When amplitudes are derived for circularly polarized light, they can be related to linearly polarized amplitudes by the following expressions

$$A_\parallel = A_{++} + A_{+-} \tag{3.9}$$

$$A_\perp = A_{++} - A_{+-} \tag{3.10}$$

where A_{+-} and A_{++} indicate the photon polarization does, or does not change sign, respectively.

Thus for a given set of calculated amplitudes, the total elastic scattering cross section for unpolarized incident radiation is calculated by summing each complex amplitude for a given polarization; squaring the magnitude of the summed amplitudes to yield a cross section for incident polarized photons; and averaging the cross sections resulting from both polarizations.

Figures 3.8 through 3.11 present real and imaginary parts of calculated complex scattering amplitudes for elastic scattering of photons incident upon uranium at a scattering angle of 120° due to the mechanisms discussed previously in this section. Dotted lines indicate that the amplitude is negative at the corresponding energy. In the phase convention used in the derivations, nuclear Thomson scattering amplitudes are always purely real, and GDR amplitudes are real below the (n,γ) threshold energy. The data from these figures come from the references indicated in Table 3.2 and approximate accuracies are also included.

The quoted accuracies come with many caveats. The Rayleigh scattering calculations are thought to be very accurate, but were only performed for K-shell electrons. Corrections due to L-shell electrons have indicated that the errors are less than 5%[53], however the errors were initially estimated for high-Z atoms to be up to 20%[63]. Delbrück scattering amplitudes are likewise calculated to high precision ($< 3\%$), but only for first-order terms in the Born series. Higher-order corrections have been estimated to be of the same magnitude as the first-order term

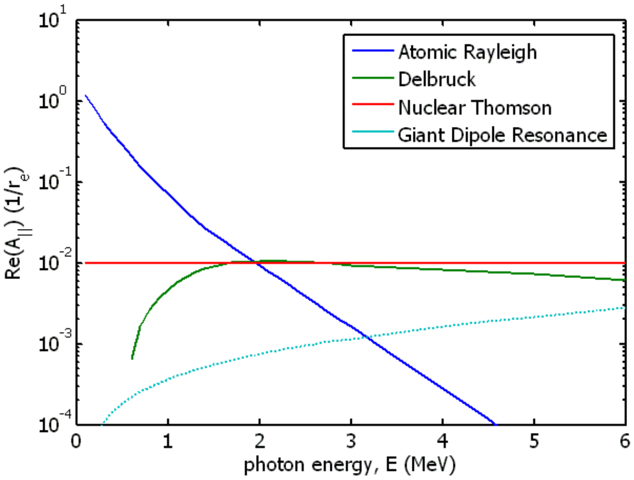

Figure 3.8 The real portion of elastic scattering amplitudes due to mechanisms of Rayleigh, Delbrück, nuclear Thomson, and GDR scattering at 120° for photons polarized parallel to the plane of scattering incident upon ^{238}U, $A_{\|}$. Dotted lines indicate a negative amplitude.

for high Z and small scattering angles. At higher angles, the higher-order terms, or Coulomb corrections, appear to be approximately 20%. The nuclear Thomson cross section appears to be well-understood for spherical nuclei. Second-order corrections due to the polarizability of the nucleus and its finite size increase quadratically with energy and are approximately 1% at 4.5 MeV. Additional corrections for nuclei of non-zero spin increase linearly with energy but these corrections are generally small[64]. GDR amplitudes are derived from reported cross sections[62]. For spin-0 ground states, the GDR amplitudes are related by

$$A_{\|}^{\mathrm{GDR}} = A_{\perp}^{\mathrm{GDR}} \cos\theta \tag{3.11}$$

With this, we can relate the amplitude to the total cross section by using equation 3.8.

$$\sigma_{\mathrm{GDR}} = \int d\Omega \frac{d\sigma_{\mathrm{GDR}}}{d\Omega} = 2\pi \frac{r_e^2}{2}|A_{\perp}|^2 \int_0^{\pi} (1+\cos\theta)\sin\theta d\theta = \frac{8\pi r_e^2}{3}|A_{\perp}|^2 \tag{3.12}$$

Solving for $|A_{\perp}|$, we find

$$|A_{\perp}| = \sqrt{\frac{3\sigma_{\mathrm{GDR}}}{8\pi r_e^2}} \tag{3.13}$$

Finally, errors reported for GDR scattering are due to differences between Lorentzian fits of experimental data for photon cross sections in the GDR energy range. These different shapes result in quite different GDR scattering cross sections at lower energies, however at the energies of interest, the GDR remains a minor contributor to the total elastic scattering cross section.

The amplitudes shown in Figures 3.8 - 3.11, are summed and squared to obtain contributions to the total photo-elastic scattering cross section due to each polarization. The real and imaginary parts of these amplitudes are shown in Figure 3.12 along with their sum, which is the total differential elastic scattering cross section for 120° scattering of photons incident upon ^{238}U. The same total differential scattering cross section is also plotted in Figure 3.13, however in this figure, the sum of the squared amplitudes for each individual elastic scattering process are also shown.

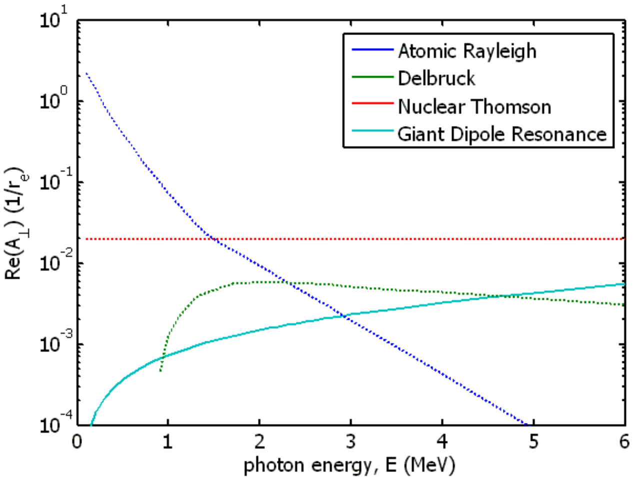

Figure 3.9 The real portion of elastic scattering amplitudes due to mechanisms of Rayleigh, Delbrück, nuclear Thomson, and GDR scattering at 120° for photons polarized perpendicular to the plane of scattering incident upon ^{238}U, $A_{\|}$. Dotted lines indicate a negative amplitude.

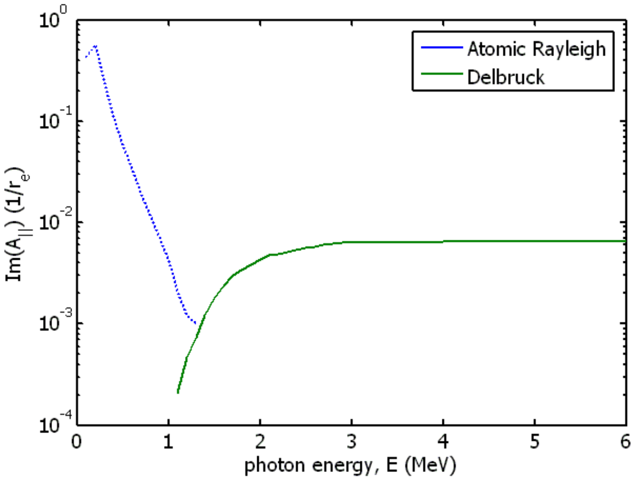

Figure 3.10 The imaginary portion of elastic scattering amplitudes due to mechanisms of Rayleigh, and Delbrück scattering at 120° for photons polarized parallel to the plane of scattering incident upon ^{238}U, $A_{\|}$. Dotted lines indicate a negative amplitude.

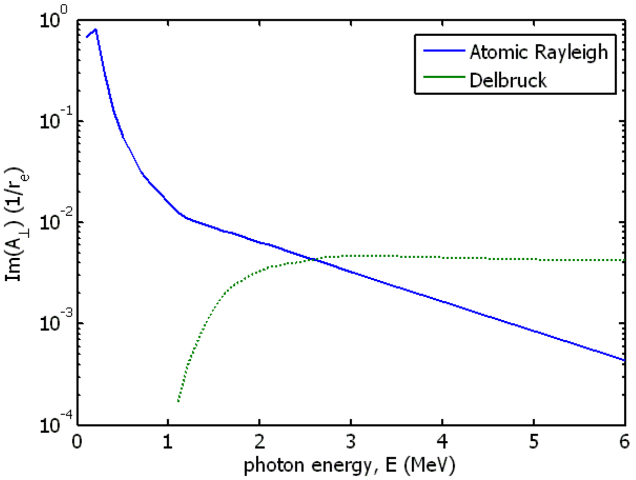

Figure 3.11 The imaginary portion of elastic scattering amplitudes due to mechanisms of Rayleigh, and Delbrück scattering at 120° for photons polarized perpendicular to the plane of scattering incident upon ^{238}U, $A_\parallel$. Dotted lines indicate a negative amplitude.

The effect of coherence is prominent near $E_\gamma = 2$ MeV, where the sums of the individual scattering cross sections are significantly less than the total cross section. Likewise, Figure 3.14 shows the cross sections of the individual elastic scattering processes and the total differential cross section for 30° scattering of photons incident upon ^{238}U. In this case, destructive interference results in a smaller total cross section near 2.5 MeV than would be expected from the individual contributions of both Delbrück and Rayleigh scattering.

Data collected from the elastic scattering of 2.754 MeV photons on various isotopes are shown in Figures 3.15 a) and 3.15 b). These figures contain data and predictions from reference[53] and the experiments performed are described both there and in references [63],[65], and[66]. The difference between the data point and the dotted lines has been attributed to the Coulomb correction. Incomplete integration of the Coulomb correction has moved theoretical elastic scattering cross sections closer to the measured data. In 1995 it was noted that computational power was limiting more complete computations[51]. This suggests that current computer technology may be able to satisfactorily tabulate Coulomb corrections to Delbrück scattering amplitudes for use in photon transport Monte Carlo codes and elsewhere.

Some insight into the quality of the MCNPX predictions for the scattered background at backwards angles can be gained by comparing the MCNPX results to separately calculated Rayleigh and nuclear Thomson contributions, to data found in the literature, and to our recently measured backscattered photon spectra for a bremsstrahlung beam on a ^{238}U target. Figure 3.16 compares calculated elastic scattering contributions for 1.408 MeV photons on uranium. The MCNPX calculation based on ENDF form factors of the angular distribution (blue line) greatly over predicts the Rayleigh scattering found in RTAB (green line). However, the MCNPX result is in good agreement with the calculated sum of Rayleigh and nuclear Thomson scattering (red line) for scattering angles above 110°, i.e., for the backwards angles of interest to NRF measurements. Figure 3.17 shows the same comparison at the higher photon energy of 2.754 MeV together with measured data from Rulhussen et al[54]. The MCNPX calculation using ENDF form factors greatly under predicts the measured cross sections at backwards angles while still over predicting the Rayleigh

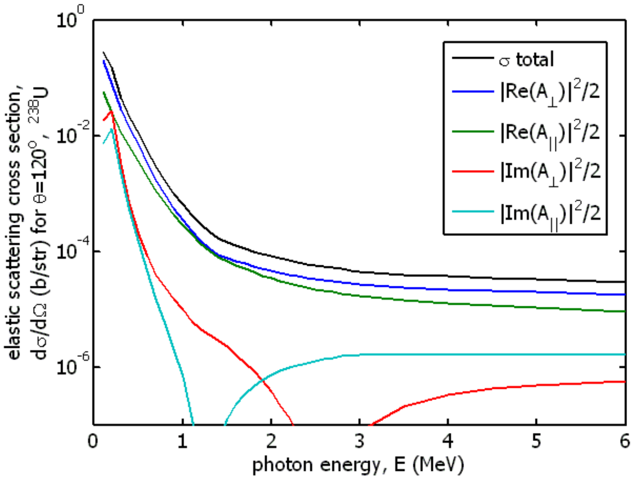

Figure 3.12 Calculated elastic scattering amplitudes and the total differential scattering cross section for 120° scattering of photons incident upon ^{238}U. The sources of the plotted values are discussed in the text

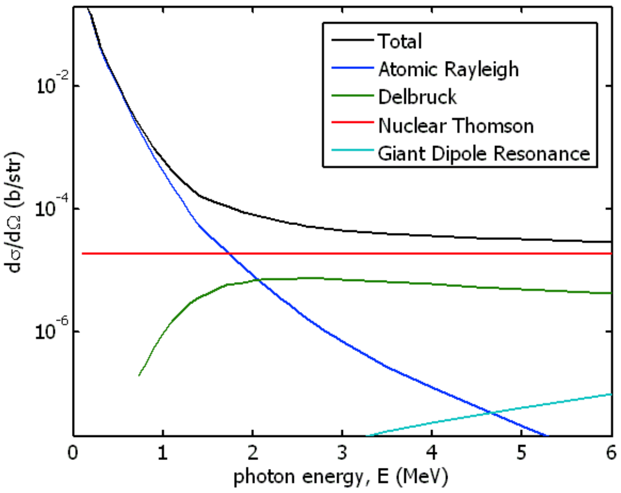

Figure 3.13 Calculated elastic scattering cross sections for individual scattering processes and the total differential scattering cross section for 120° scattering of photons incident upon ^{238}U. Individual cross sections are non-physical because they cannot be separately measured from the total cross section. The sources of the plotted values are discussed in the text.

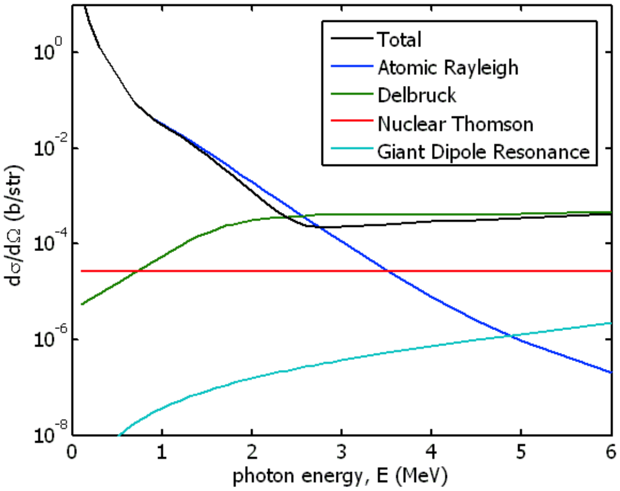

Figure 3.14 Same as Figure 3.13 but for 30° scattering.

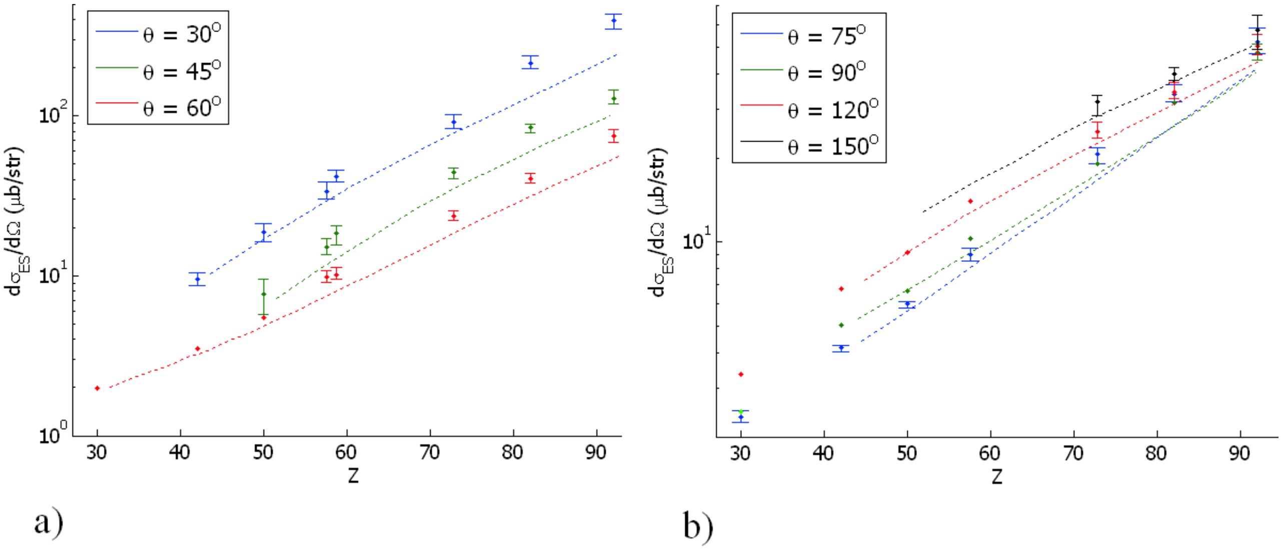

Figure 3.15 a) Measured and predicted elastic scattering cross sections for 2.754 MeV photons and scattering angles 30° - 60° incident upon ^{65}Zn, ^{92}Nb, Ce, ^{141}Pr, Nd, Ta, Pb and U. Dashed lines are theoretical predictions including summed amplitudes of Rayleigh, nuclear Thomson, GDR, and Delbrück scattering without Coulomb correction terms. The data for this figure are taken from reference[53].
Figure 3.15 b) Same as Figure 3.15 a) but for scattering angles of 75° - 150°. The data for this figure are taken from reference[53].

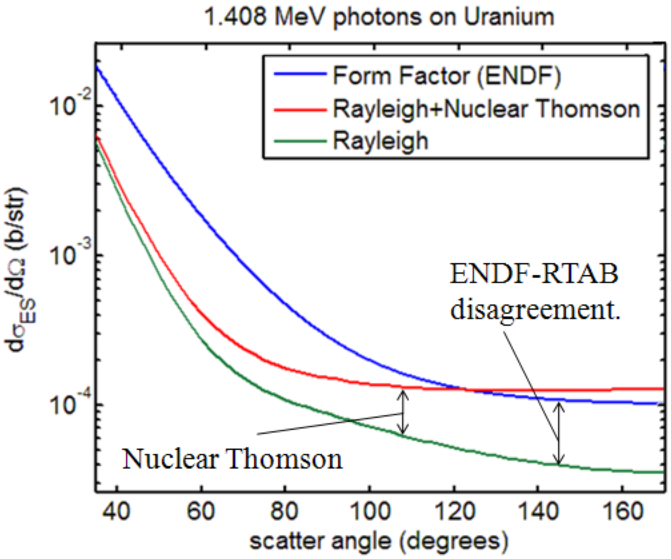

Figure 3.16 Elastic scattering contributions calculated for 1.408 MeV photons on uranium as a function of the scatter angle.

contribution. At this higher energy nuclear Thomson scattering, which is not included in the MCNPX calculations, is the main elastic scattering contribution.

A comparison of MCNPX predictions with a backscattered (120°) photon spectrum that was measured by us for a bremsstrahlung beam (not a mono-energetic photon beam as in Figures 3.16 and 3.17) on a ^{238}U target is shown in Figure 3.18. The spectrum is equally well reproduced by the MCNPX calculation with the corrected Rayleigh treatment and by the "old" MCNPX results to which Rayleigh and nuclear Thomson scattering contributions were added manually. The data shown in Figures 3.16 and 3.17 suggest that this agreement is likely special for the scattering angle and energy range of the measurement and that the differences may be much greater for other scattering angles and photon energies.

Figure 3.19 shows the same comparison as Figure 3.17 but for the elastic scattering off iron instead of uranium. For the lighter element the nuclear Thomson scattering contribution is orders of magnitude higher than the Rayleigh contribution at scattering angles larger than 30° and thus, the MCNPX calculation without the nuclear Thomson contribution under predicts the elastic scattering by orders of magnitude.

These comparisons indicated that it would be desirable to include nuclear Thomson scattering in MCNPX simulations for NRF studies. Calculations based on ENDF form factors as currently implemented in MCNPX could underestimate the elastic scattering cross section by as much as a factor of ten for an uranium target. Even larger discrepancies may be possible for lighter elements such as zirconium, which is used in the cladding of fuel pins.

3.2 Addition of Available NRF Resonance Data to ENDF and MCNPX Datafiles

In order to be able to model the NRF response in MCNPX measured NRF data were added to the photonuclear evaluated nuclear data files (ENDF) and were converted to ACE files for use

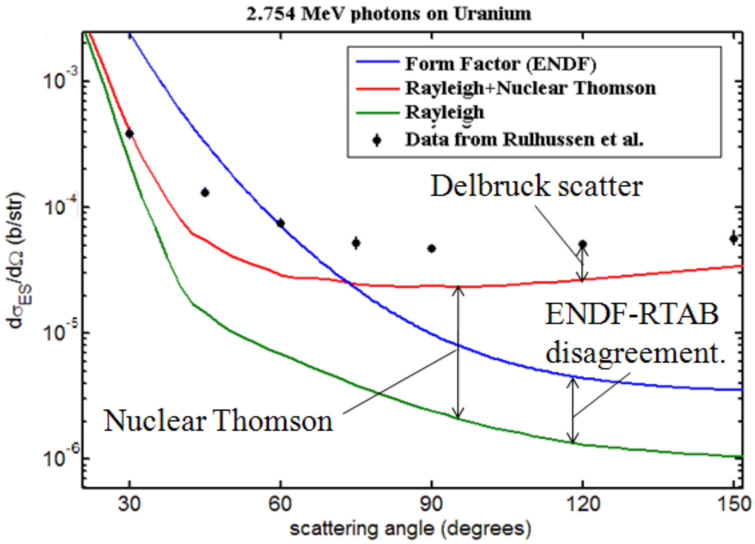

Figure 3.17 Comparison of elastic scattering contributions with measurement data for 2.754 MeV photons on uranium.

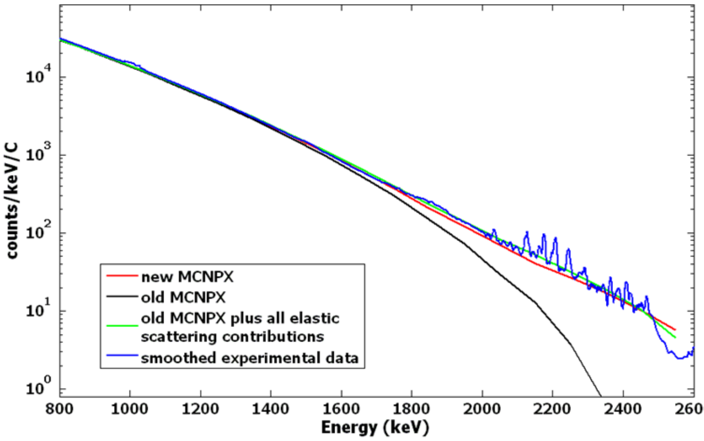

Figure 3.18 Comparison of the elastic scatter background between MCNPX simulations and experimental data

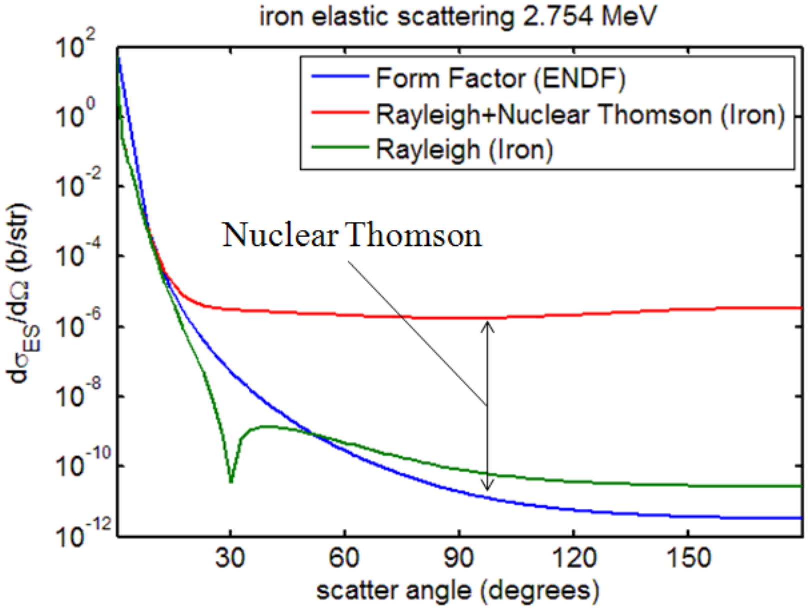

Figure 3.19 Calculated elastic scattering cross sections as a function of scattering angle for 2.754 MeV photons on uranium.

in MCNPX [25]. To maintain compatibility with existing data processing codes such as NJOY [26], cross sections for NRF interactions have been added as pointwise data and characteristic NRF γ rays are added as secondary particles emitted by the reaction. The energy width between consecutive data points was selected to be a minimum of 2 eV due to ENDF format limitations. The resonances were Doppler broadened assuming a temperature (T) of 300 K. Similar to the implementation of NRF cross sections, the energies of emitted NRF γ rays are entered into ENDF pointwise, and the multiplicity for photon emission is defined for each resonance.

The NRF responses of ^{235}U and ^{239}Pu were measured in 2006 and 2007[23], and the results from these experiments are presented in Tables 3.4 and 3.3. Several pairs of observed NRF γ rays were found to have energy differences equal to the excitation energy of low-lying excited states (7.9 ± 0.002 keV for ^{239}Pu and 46.21 ± 0.01 keV for ^{235}U)[27]. In these cases the sum of the measured cross sections is shown in the table, and the tabulated value of Γ_0/Γ differs from unity. Subsequent experiments attempting to measure higher-energy NRF resonances in these isotopes have not yielded new transitions[28, 29].

3.3 MCNPX Simulation Techniques

MCNPX simulations are used in this study for calculating non-resonant scattered backgrounds, backscatter measurements, notch refilling in a transmission assay, detector responses and resonant attenuation. How this has been done is described below.

3.3.1 MCNPX Simulation of Backscatter Measurements with Bremsstrahlung

With the addition of NRF data to MCNPX datafiles and the inclusion of elastic photon backscatter to MCNPX, the code may directly be used to determine expected photon intensities and count

Table 3.3 ^{239}Pu NRF data. The values of $\int \sigma_{\mathrm{NRF}} dE$ were taken from Reference [23]. Where $g\Gamma_0 \neq g\Gamma$, two NRF γ rays were measured at energies that differ by the excitation energy of the first excited state of ^{239}Pu. It has been assumed that these γ rays correspond to de-excitation of a single NRF state. Values of gΓ_0 were calculated from from equation 2.2. The meaning of α_f is explained in the text.

E_{level} (MeV)	gΓ (meV)	gΓ_0 (meV)	$\int \sigma_{\mathrm{NRF}} dE$ (eV·b)	α_f (cm^2/g)
2.040	4.3 ± 1.1	4.3 ± 1.1	8 ± 2	0.0081 ± 0.0021
2.144	13.4 ± 2.2	10.2 ± 1.7	17 ± 3	0.0164 ± 0.0027
2.289	5.4 ± 1.4	5.4 ± 1.4	8 ± 2	0.0072 ± 0.0019
2.432	30.8 ± 5.8	14.6 ± 2.8	19 ± 4	0.0160 ± 0.0030
2.454	7.1 ± 2.4	7.1 ± 2.4	9 ± 3	0.0077 ± 0.0026
2.464	6.3 ± 3.2	6.3 ± 3.2	8 ± 4	0.0068 ± 0.0034

Table 3.4 Characteristics of measured NRF states in ^{235}U as reported in reference[23]. Values of $g\Gamma_0$ were obtained by application of equation 2.2. States where $\Gamma_0/\Gamma \neq 1$ indicate that a γ ray of energy, $E_\gamma = E_C - 46.2$ keV was observed. These lines are assumed to correspond to de-excitation of the NRF state via emission of a γ ray populating the low-lying $9/2^-$ excited state of ^{235}U. Values of $\int \sigma_{\mathrm{NRF}}\, dE$ shown here are the sum of the reported values.

E_{level} (keV)	gΓ (meV)	gΓ_0 (meV)	$\int \sigma_{\mathrm{NRF}} dE$ (eV·b)
1656.23 ±0.80	1.47 ±0.46	1.47 ±0.46	4.1 ±1.3
1733.60 ±0.22	17.0 ±2.0	14.11 ±1.61	35.9 ±4.1
1815.31 ±0.22	8.79 ±1.06	6.05 ±0.73	14.1 ±1.7
1827.54 ±0.23	2.91 ±0.52	2.91 ±0.52	6.7 ±1.2
1862.31 ±0.20	4.33 ±0.77	4.33 ±0.77	9.6 ±1.7
2003.32 ±0.25	5.07 ±0.89	5.07 ±0.89	9.7 ±1.7
2006.19 ±0.31	2.46 ±0.84	2.46 ±0.84	4.7 ±1.6

Table 3.5 Relevant ^{238}U NRF data. Values of Γ_0^2/Γ and Γ_1/Γ_0 were taken from reference[24] where γ-ray emission to the first excited state of ^{238}U ($J^\pi = 2^+$) at 44.92 keV were also measured. Here, it is assumed that this probability is $1 - \Gamma_0/\Gamma$. The final column is calculated from equation 2.2, it has a fractional uncertainty equal to that of Γ_0.

E_{level} (MeV)	Γ (meV)	Γ_0 (meV)	$\int \sigma_{\mathrm{NRF}} dE$ (eV·b)
2.176	54.7 ± 2.5	36.0 ± 2.2	87.7 ± 5.2
2.209	54.3 ± 2.8	35.0 ± 2.3	82.7 ± 5.1
2.245	29.0 ± 1.6	19.7 ± 1.4	45.0 ± 3.0
2.295	13.4 ± 1.5	8.4 ± 1.0	14.4 ± 1.4
2.410	26.0 ± 1.7	16.9 ± 1.2	33.6 ± 2.1
2.468	30.2 ± 2.2	20.1 ± 1.6	38.0 ± 2.8

rates in backscatter NRF measurements.

The primary difficulty in simulating backscattered NRF is that the vast majority of photons that interact within the assay target produce low-energy or forward-scattered photons. However, the energetic portion of the backscattered photon spectrum is of most interest. To overcome these difficulties, variance reduction techniques are used.

First, the time-consuming simulation of bremsstrahlung source spectra is done separately. Thereafter, the calculated bremsstrahlung spectrum is used as a source term for separate simulations.

A second simulation is conducted with the bremsstrahlung photons incident upon a target in the backscatter NRF assay geometry. Sampling of the bremsstrahlung photon source spectrum is biased to preferentially simulate photons of higher energies, with reduced statistical weights. The photon flux at a hypothetical detector location is then calculated using the next-event estimator tally (F5) wherein each time a particle interacts in the assay target, the probability for emission of a particle in the direction of the detector is determined, and a value proportional to this quantity is added to the flux tally.

In a third simulation, the response of a radiation detector is simulated by impinging the photon spectrum determined in the second calculation onto a shielded detector geometry. The energy deposited within the detector volume is tallied, and if necessary, an energy resolution-broadening routine is applied. These simulations provide the total and NRF count rates that are expected for a given assay geometry.

3.3.2 MCNPX Simulation of Resonant Attenuation

In addition to determining expected NRF and background signal rates for transmission measurements using bremsstrahlung sources, MCNPX was also used to test the analytical effective attenuation model. This is done by determining the NRF flux at a detector position when no resonant absorption occurred in the assay target and comparing that to the NRF flux when the Pu IOI is present in the target.

NRF peak intensities are calculated using MCNPX for two geometries, one in which the Pu IOI is present in the fuel assembly, and another in which it is absent. The removal of the IOI from the assembly results in slight changes in the non-resonant attenuation of photons as they penetrate the assembly. To correct for this non-resonant attenuation change, the intensity of NRF peaks is normalized by the intensity of the 511 keV peak which is entirely due to pair production in the TD , i.e.,

$$\mathbb{A}_{E_{pk}} = \frac{A_{E_{pk}}}{A^{noPu}_{E_{pk}}} \frac{A^{noPu}_{511}}{A_{511}} \tag{3.14}$$

This is analogous to the method described in Section 4.3, and proved satisfactory when experimentally tested. The quantity $\mathbb{A}_{E_{pk}}$, is used in equation 2.36 for the corresponding resonance to determine the expected areal density of Pu in the target.

Figure 3.20 presents a comparison between analytical effective attenuation values and those obtained using the analysis method described here to evaluate $\mathbb{A}_{E_{pk}}$. Two analytical curves are provided. The blue curve is the analytically-expected attenuation due to the 2431 keV ^{239}Pu resonance, as in equation 2.36. The green curve is the expected attenuation due to the 2431 keV ^{239}Pu resonance if the 5 point evaluation of the Maxwell-Boltzmann cross section is used as the cross section form (as described in Section 2.5). This curve is shown because the 5 point evaluation

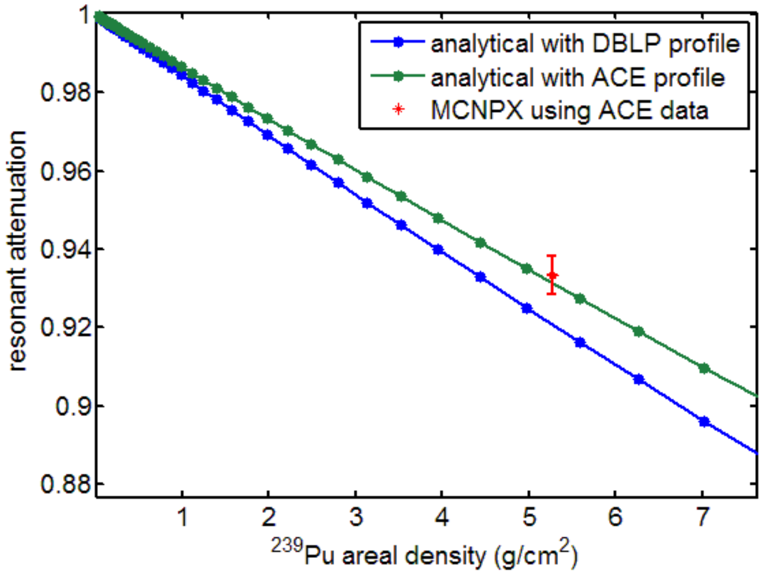

Figure 3.20 Comparison of analytically-calculated effective attenuation values with that calculated by MCNPX. The different analytical curves correspond to the expected true form (blue) and that due to the shape of the NRF data entered into the ACE file used by MCNPX.

profile is used to described resonances in MCNPX (in the ACE data format). The red point with error bars indicates an effective attenuation value obtained via MCNPX calculations. Although the MCNXP value overlaps the green curve within the error bars, it is anticipated that the true value would lay above the curve, due to the effects of notch refill.

3.3.3 *Notch Refilling* and Transmission Assay Complications

In transmission measurements, the attenuation of resonant-energy photons in the target provides the signal that relates to areal density of the IOI in the target. This attenuation manifests itself in a decrease in the flux intensity at the resonance, which is often referred to as a *notch*. *Notch refilling* is the process by which interrogating photons are down-scattered into the notch during transport through the assay target and TD. The down-scatter of photons results in more resonant-energy photons leaving the assay target than would be predicted by the model described in Section 2.4.2.2. In this section, the relative intensity of the notch-refilling effect is considered.

Notch refilling depends not only on the shape of the energy spectrum, but also on the measurement geometry because the down-scattered photons must interact in the TD in order to change the measured signal. The smaller the solid angle subtended by the TD, the more restricted is the geometry for notch refilling. Likewise, increasing the number of photons that have more energy than the excitation energy of a resonance increases the likelihood that some of these photons will down-scatter into the notch created by resonant absorption.

The processes that result in notch refilling are incoherent scattering and bremsstrahlung emitted from photo-electrons. Both processes predominantly produce down-scattered photons at forwards angles. Those photons that are down-scattered into a resonant energy and toward the TD effectively refill the notch.

To examine this effect, we first consider a Monte Carlo simulation of 2.3 MeV photons incident upon an assay target. The target consisted of 7 cm thick slab of Pb behind a 4.4 mm thick slab

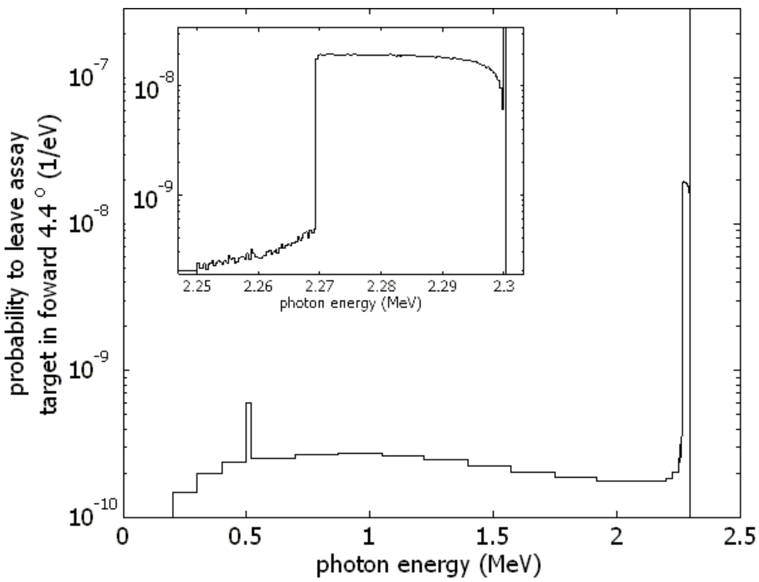

Figure 3.21 Calculated spectrum of photons leaving a target of areal density similar to a homogenized fuel assembly within 4.4° of the initial photon direction. The incident photon energy was 2.3 MeV. The inset shows a larger view of the energy range of 2.25 - 2.3 MeV. The probability that an incident photon leaves the target without interacting is 2.1%.

of uranium, which is comparable to the average areal density of a fuel assembly. The energy spectrum of photons leaving the assay target within 4.4° of the initial direction were calculated. The selection of 4.4° is representative of the solid angle that would be subtended by a large TD , as described in Section 3.3.2. The results of this simulation are shown in Figure 3.21. Full-energy photons and those that have undergone a single incoherent scatter are the most probable sources of emitted photons. The photons that undergo a single incoherent scatter produce a continuum of photons between 2.27 and 2.3 MeV. Pair production and subsequent positron annihilation, multiple-scattering events, and secondary electron bremsstrahlung produce the events indicated below the Compton continuum.

A 2.3 MeV initial energy photon undergoing incoherent scattering with $\theta \leq 4.4^{\circ}$ results in a scattered photon with energy $E' \geq 2.27$ MeV. This energy is the lower energy of the Compton continuum. The probability per 2.3 MeV incident photon for an emitted photon to be down-scattered into the Compton continuum is approximately 2×10^{-8} per eV. Doppler-broadened NRF resonances tend to have $\Gamma \approx 1.5$ eV, thus we can assume 3×10^{-8} per eV is a reasonable probability for down-scattering of 2.3 MeV photons into its Compton continuum for assay targets of similar areal densities as fuel assemblies.

To consider the potential for refill of a given resonant notch, only photons incident upon the assay target whose Compton continuum includes the resonance energy are of importance. If the TD only subtends a polar angle of 4.4° only photons with $E - E_{res} \lesssim 35$ keV need be considered. From Figure 2.5, we expect $\sim 2 \times 10^{8}$ photons/eV/Coulomb to impinge upon the assay target in the energy range of 2 - 2.4 MeV. Combining this source photon rate with the notch-refill probability ($\sim 2 \times 10^{-8}$ per eV) and the range of energies of interest, we expect $\sim 1.4 \times 10^{5}$ notch refill events per Coulomb of electrons incident upon the Bremsstrahlung converter. Conversely, if an entire bremsstrahlung spectrum were transmitted through this target, we would expect in the absence of resonant attenuation, $\sim 4.5 \times 10^{6}$ photons/eV/C to be incident upon the TD between 2 and 2.4

MeV. Thus, photons that arrive at the TD, after down-scattering, represent 2 - 5% of the total flux in this energy range.

From these estimates, we expect that notch refilling will result in a slight decrease in the slopes of the effective attenuation curves, $\mathbb{A}(Nx)$ (Figure 2.9) compared to those predicted by neglecting notch refill. This, in turn, would slightly increase the statistical uncertainties estimated in Table 5.3 and the surrounding discussion. Nevertheless, notch refilling would change the statistical uncertainty estimates for a measurement of a Pu isotope in spent fuel significantly less than the contributions from uncertainties in the measured NRF cross sections. We therefore conclude that while notch refilling is likely to be an important factor in achieving an absolute areal density measurement with precision near 1%, the NRF cross sections must be known to far better precision before this level of uncertainty can be reached.

3.3.4 Division of Simulations Into Resonant and Non-resonant Problems

The simulation of NRF measurements that use quasi-monoenergetic photon sources can be treated differently from bremsstrahlung source simulations because of the narrow range of photon energies that must be considered. This implies that non-resonant source photons will behave similarly, regardless of their initial energy. To take advantage of this, two separate simulations are conducted for assay using quasi-monoenergetic photons, one with source photons of resonant energy, and the other where the effects of NRF is turned off, which only simulates the transport of non-resonant photons.

These two simulations may be combined by summing the two spectra, weighted by the relative number of resonant and non-resonant photons in the source spectrum. This decomposition method is used throughout Section 5.1.2.

4 Transmission Nuclear Resonance Fluorescence Measurements of ^{238}U in Thick Targets

This experiment was supported by the MPACT campaign of the FCR&D program of the Office of Nuclear Energy (US DOE), the Office of Proliferation Detection (US DOE, NA-221) contributed to the analysis of the experimental results by supporting the development of analytical and Monte Carlo modeling tools. The experiment provides validation of the modeling and demonstrates the transmission measurement method.

4.1 Introduction and Experimental Goals

Transmission nuclear resonance fluorescence measurements were made of ^{238}U in thick targets consisting of Pb and depleted U with total areal densities near 86 g/cm^2 using a bremsstrahlung source. The target thickness was selected to have an areal density and attenuation properties similar to a nuclear fuel assembly so that the applicability of the transmission method as a non-destructive measurement technique for spent nuclear fuel could be tested. In this experiment Pb was used as a surrogate for the UO_2 matrix in spent fuel and the ^{238}U in depleted uranium (DU) was used as a surrogate for ^{239}Pu or any other minor actinide that would be measured in spent fuel. The amount of ^{238}U used in the experiment varied from 0 to 8.5% (atom fraction) and thus represented significantly higher concentrations than those of minor actinides in spent fuel. These amounts were selected to demonstrate the transmission attenuation effect in a timely manner using readily available radiation detectors and photon sources. A similar measurement was made using thinner targets and a quasi-monoenergetic photon source[35]. The experiment demonstrates the capability of using transmission measurements as a non-destructive technique to identify and quantify the presence of an isotope in samples with thicknesses comparable to the average thickness of a nuclear fuel assembly. The experimental data also appear to demonstrate the process of notch refilling.

4.2 Experimental Setup

The experiment was conducted at the High Voltage Research Laboratory at the Massachusetts Institute of Technology. Electrons accelerated to 2.60 ±0.03 MeV by a Van de Graaff accelerator were transported through a beamline, around a 90^{o} bend, and entered the experimental geometry as shown in Figure 4.1. The converter target consisted of a 102 μm thick Au layer on a 1 cm thick water-cooled Cu backing. The electron current incident upon the converter was approximately 65 μA throughout the experiment. The bremsstrahlung emitted from the converter target was shaped by a 20 cm thick Pb collimator. The diameter of the collimator opening was 1 cm on the bremsstrahlung converter side, and increased to 2.5 cm, for a 3.6^{o} opening from the beam center, and a maximum angular acceptance of 5^{o}.

Figure 4.1, shows the important components: the bremsstrahlung converter and collimator, the assay target, the transmission detection sheet, the HPGe detectors and the Pb shielding. The

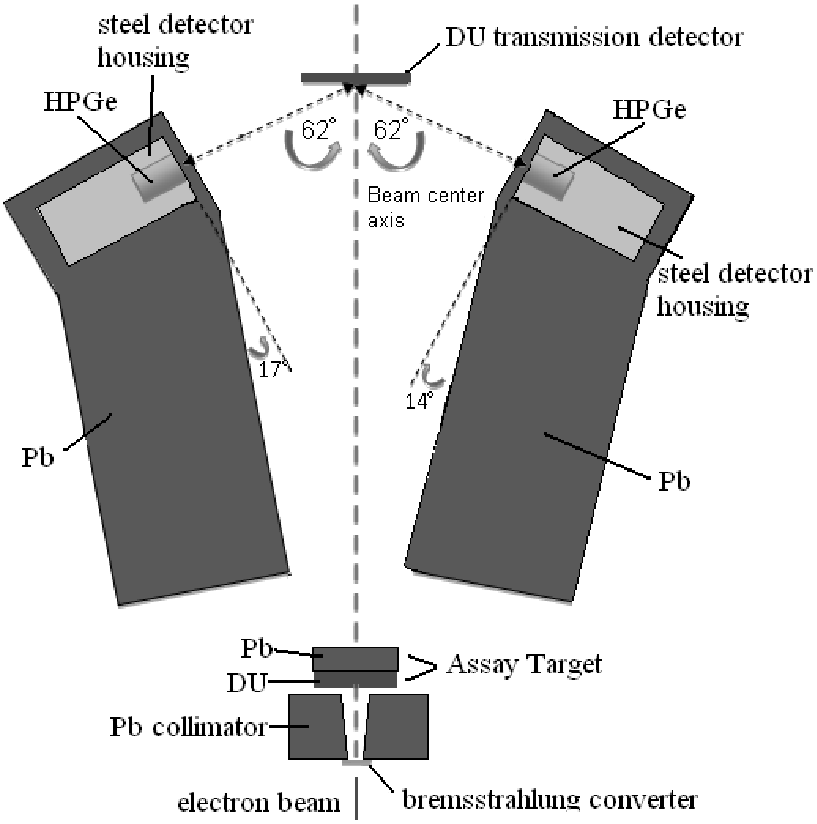

Figure 4.1 Schematic view of experimental setup. DU thicknesses have been exaggerated for visibility.

assay target, a combination of DU and Pb, was located directly downstream of the collimator opening. The areal densities of DU and Pb used in the assay targets are summarized in Table 4.1. The DU was placed up-stream of the Pb in the beam, setting up the most probable geometry for notch refill.

The transmission detection sheet was placed 142 cm downstream of the collimator opening and was not moved throughout the experiment. It consisted of five 20.32 cm x 20.32 cm DU sheets that were nominally 0.8 mm thick. Each sheet was contained in two plastic bags. The total mass of the five plates plus the containment bags was measured to be 3341.7 ± 3.3 g, of which 3226.7 ± 28 g are attributed to the DU. Behind the DU plates, 82.3 ± 0.5 g of Mn and 185.1 ± 0.8 g of 99.52% enriched ^{11}B were also positioned in the beam to serve as auxiliary flux monitors.

Table 4.1 Assay target compositions. Pb density assumed to be 11.34 g/cm^3, DU sheets were assumed to be 99.799% ^{238}U by mass. Uncertainties in DU masses are approximately 1%.

run	ρx_{DU} (g/cm^2)	ρx_{Pb} (g/cm^2)	total ρx (g/cm^2)	^{238}U atom%
1	0	86.26	86.26	0
2	8.47	79.85	87.86	8.48
3	1.69	85.20	86.80	1.69
4	3.34	83.37	86.54	3.37

Table 4.2 γ-ray lines identified in overnight background spectra used to calibrate energy spectra[37].

E_{line} (keV)	Isotope
766.36	$^{234\text{m}}$Pa
1001.03	$^{234\text{m}}$Pa
1193.77	$^{234\text{m}}$Pa
1460.83	^{40}K
1737.73	$^{234\text{m}}$Pa
1911.17	$^{234\text{m}}$Pa
2204.21	^{214}Bi
2614.49	^{208}Tl

Two pairs of approximately 100% relative efficiency high-purity germanium detectors were positioned 27 cm from the intersection of the beam center and the transmission detection sheet, at an angle of 118° relative to the centroid beam direction. Actual detector acceptances were distributed around the centroid angle with an approximate 10° width. The detectors were contained in steel housings that were stacked in pairs, resulting in one detector being centered 4.5 cm above the beam center and the other centered 7 cm below the beam center.

Pb brick walls with minimum thicknesses of 80 cm were constructed to shield the radiation detectors from the bremsstrahlung converter and assay target. The detectors were also shielded with 5 cm of Pb in the down-stream direction, 10 cm of Pb below and behind the detectors, 17 cm of Pb above the detectors, and with a 1.27 cm thick Pb *filter* facing the transmission detection sheet. The filter reduces the intensity of low-energy photons emitted from the transmission detection sheet due to Compton scatter and other processes.

Each target was irradiated for approximately 7 hour measurements. The electron beam current was nominally 65 μA for each irradiation. The detectors were operated with Ortec DSPEC Pro$^{\text{TM}}$ digital γ-ray spectrometers. The integrated pulse amplitudes were read and stored using MAESTRO-32 and a personal computer. In this configuration, the ADC rates were approximately 10^4 counts per second.

4.3 Data Analysis

Spectra were collected during four day-long irradiation shifts and background spectra, with no electron beam incident upon the bremsstrahlung converter, were collected overnight. The radioactivity of the DU and ambient ^{40}K provided lines for energy-calibrating the detectors. The γ-ray energies used for energy calibration are shown in Table 4.2. After calibrating the four detectors, their spectra were re-binned to a common energy grid and summed to provide a single spectrum for each target. An example of spectral summing is provided in Figure 4.2. After summing, peaks that were present in spectra taken during irradiations but not in background spectra were attributed to NRF.

To correct for varying beam intensity and the differing attenuation lengths of the targets, the rates at which 511 keV γ rays were measured in the detectors were compared. To demonstrate the accuracy of this normalization, a series of calculations were performed using MCNPX. The calculations simulated a bremsstrahlung spectrum transported through the four different targets. The photon spectra that reached the transmission detection sheet after emission from each of the

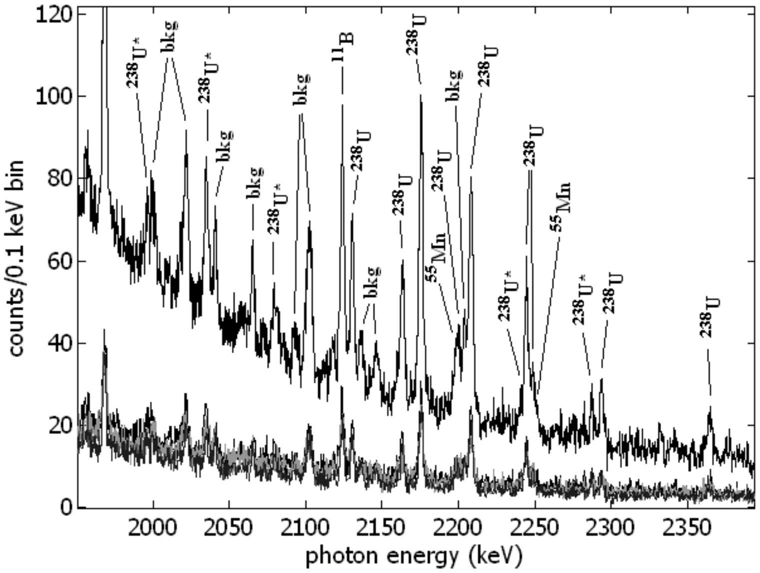

Figure 4.2 Spectra from all four detectors collected during run 1. The lower spectra are from the four different detectors before summing. Summing of these spectra produce the upper spectrum, which includes labeling to indicate the source of identified peaks. 'bkg' indicates the peak is present in the radioactive background spectrum, '^{238}U' indicates the peak is due to a known ^{238}U NRF resonance, and '^{238}U*' indicates the peak is suspected to be due to ^{238}U NRF.

assay targets is defined as $\Phi^i(E)$, where the superscript indicates the target used in the run, whose number is indicated in Table 4.1. Each of these computed spectra were also convolved with the cross section for pair production in uranium[22] to provide a quantity proportional to the rate at which pair production occurred in the transmission detection sheet,

$$R^i_{\mathrm{PP}} = \int \Phi^i(E)\sigma_{\mathrm{PP}}(E)dE \tag{4.1}$$

Computed photon spectra, $\Phi^i(E)$, were then normalized by dividing each spectrum by R^i_{PP}, and compared. The quantity,

$$\Phi^i_N(E) = \frac{\Phi^i(E)/R^i_{\mathrm{PP}}}{\Phi^1(E)/R^1_{\mathrm{PP}}} \tag{4.2}$$

is shown in Figure 4.3 for the three targets containing DU. If the simulations indicated that normalization by measured pair production rates were perfect, the functions, $\Phi^i_N(E)$ would be unity at all energies. The calculations indicate that below approximately 1.8 MeV, normalizing spectra incident upon the transmission detection sheet by the intensity of pair production would result in large errors. However, the normalization needs only to be accurate in the range of the NRF resonances: 2.1 - 2.5 MeV. In this range the calculations indicate that by using the measured 511 keV peak to normalize the intensity of photons reaching the transmission detection sheet after penetrating through differing targets, should incur less than a 1.5% systematic error. The error bars in Figure 4.3 indicate the uncertainty of the MCNPX calculation, and do not include the systematic error due to the linear, rather than logarithmic, interpolation of atomic scattering functions that is performed in MCNPX[38]. The saw-tooth shape of the inset in Figure 4.3 can be attributed to these interpolation errors, and therefore the actual systematic error due to this normalization technique may be closer to 0.5%.

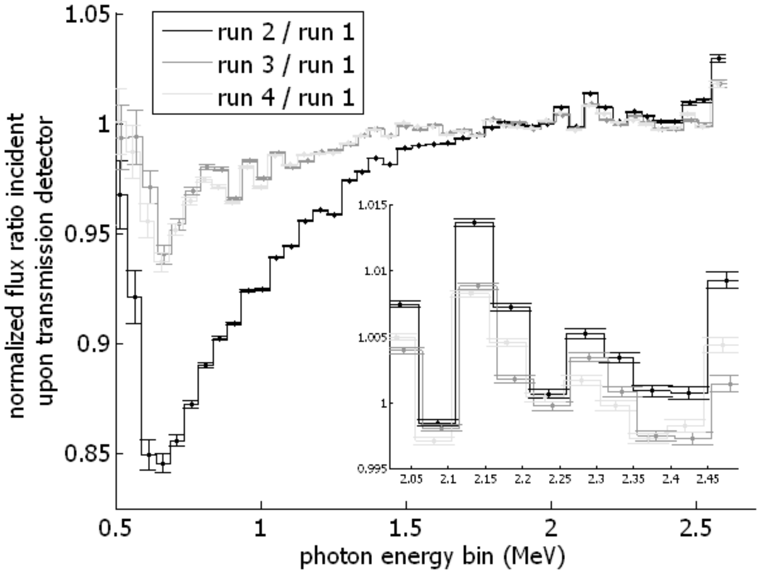

Figure 4.3 Calculated values of $\Phi^i_N(E)$, given by Equation 4.2 for the measurement of the targets containing DU, i=2, 3 and 4.

The normalization technique also automatically accounts for differing non-resonant attenuation of photons in the assay targets due to varying compositions and systematic uncertainties that may arise due to errors in electron beam integration. This is because neither of these quantities is directly used in the analysis. Instead, the intensity of the measured 511 keV photopeak provides a measured quantity that is proportional to the intensity of 2 - 2.5 MeV photons that reach the transmission detection foil, and that the total systematic error may be up to 1.5%. Given that statistical uncertainties described in Table 4.3 are between 6.7 and 28%, the addition of a systematic error of this magnitude will have little effect on the overall conclusions.

^{238}U NRF peaks identified in runs 2 - 4 were fit, integrated, and compared to corresponding peak intensities from run 1. The comparison of peak intensities is expressed as

$$\mathbb{A}^i_{E_{pk}} = \frac{A^i_{E_{pk}}}{A^1_{E_{pk}}} \frac{A^1_{511}}{A^i_{511}} \tag{4.3}$$

where $\mathbb{A}^i_{E_{pk}}$ is the relative intensity of the peak at $E = E_{pk}$ for run i, relative to run 1. $A^i_{E_{pk}}$ corresponds to the fit area of that peak. Each resonance yielded two observable peaks, due to de-excitation of the NRF level directly to the ground level, and also due to de-excitation via the first-excited state. The two values of $\mathbb{A}^i_{E_{pk}}$ for each level were averaged, resulting in a single value of $\mathbb{A}^i_{level}$ for each NRF level, measured in each of runs 2 - 4. These values are shown in the last columns of Table 4.3.

4.4 Areal Density Measurement

The areal density of an isotope in an irradiated target is related to the attenuation of resonant energy photons, as observed by a reduction in the rate that radiation detectors measure NRF γ rays emitted from the transmission detection sheet. For each ^{238}U resonance, a function was

Table 4.3 Predicted and measured values of $\mathbb{A}^{i}_{level}$ with statistical errors. The levels at 2467 and 2080 keV have not been previously reported and therefore no prediction of $\mathbb{A}^{i}_{level}$ was made. Predicted values of $\mathbb{A}^{i}_{level}$ are obtained from evaluation of Equation 4.4 using the values of Γ and Γ_0 reported in Heil et al. and that $C_{\text{notch}} = 1$, column C uses values of Γ and Γ_0 from ENSDF, columns B and D use the same values as A and C, respectively, but use the best-estimate of C_{notch} shown in Figure 4.4.

	E_{level}	predicted attenuation					measured	
	(keV)	A	B	C	D	uncertainty	attenuation	
run 1	2175.6	0.54	0.57	0.55	0.58	±0.018	0.58	±0.05
	2208.2	0.55	0.58	0.57	0.59	±0.019	0.62	±0.06
	2246.7	0.71	0.73	0.72	0.74	±0.016	0.72	±0.09
	2293.8	0.87	0.87	0.87	0.88	±0.014	0.94	±0.16
	2409.7	0.78	0.80	0.79	0.80	±0.013	0.84	±0.16
	2467.4	0.76	0.78	0.77	0.79	±0.016	0.65	±0.18
	2080.0						0.87	±0.15
	2287.4						0.67	±0.27
run 2	2175.6	0.88	0.89	0.88	0.89	±0.006	0.92	±0.06
	2208.2	0.88	0.89	0.89	0.90	±0.006	0.93	±0.07
	2246.7	0.93	0.94	0.94	0.94	±0.004	0.84	±0.09
	2293.8	0.97	0.97	0.97	0.97	±0.003	0.99	±0.16
	2409.7	0.95	0.95	0.95	0.96	±0.003	1.00	±0.16
	2467.4	0.95	0.95	0.95	0.95	±0.004	1.02	±0.21
	2080.0						0.99	±0.18
	2287.4						0.75	±0.27
run 3	2175.6	0.77	0.79	0.78	0.79	±0.011	0.82	±0.06
	2208.2	0.78	0.80	0.79	0.81	±0.011	0.80	±0.07
	2246.7	0.87	0.88	0.88	0.89	±0.008	0.89	±0.10
	2293.8	0.94	0.95	0.95	0.95	±0.006	0.84	±0.15
	2409.7	0.91	0.91	0.91	0.92	±0.006	1.00	±0.17
	2467.4	0.90	0.90	0.90	0.91	±0.007	1.04	±0.22
	2080.0						0.90	±0.16
	2287.4						0.59	±0.37
	χ^2	6.84	4.79	5.72	4.34			

derived that relates the rate at which NRF γ rays are emitted from the transmission detection sheet to the areal density of ^{238}U in the assay target. This function, for a target containing the measured isotope at an areal density, ρx, is given by

$$\mathbb{A}_{\text{model}}(\rho) = C_{\text{notch}} \frac{\int \lambda(t_{\text{TD}}, E) \exp[-\sigma_D(E)\rho x]\sigma_D(E)dE}{\int \lambda(t_{\text{TD}}, E)\sigma_D(E)dE} \tag{4.4}$$

where $\lambda(t_{\text{TD}}, E)$ is the effective thickness a photon of energy, E, traverses in a transmission detection sheet having a thickness, t_{TD}, and atom density, N_{TD}, given by

$$\lambda(t_{\text{TD}}, E) = \frac{1 - \exp[-(\alpha + N_{\text{TD}}\sigma_D(E))t_{\text{TD}}]}{\alpha + N_{\text{TD}}\sigma_D(E)} \tag{4.5}$$

and $\alpha = \mu_{nr}[1+1/\cos(\theta)]$ and $\theta \approx 62^{\circ}$ for the experimental geometry. μ_{nr} contains the attenuation coefficients for all non-resonant photon scattering events, and has been retrieved from the XCOM database[22]. The quantity, C_{notch}, accounts for notch refill.

For targets as thick as a fuel assembly notch refill can impact the measurement and needs to be taken into account. The term *notch refill* is used to describe the process by which photons incident upon the assay geometry down-scatter to the energy of a resonance and subsequently interact in the transmission detection sheet. The process results in less observed resonant attenuation than would be predicted by consideration of simple exponential attenuation, and therefore neglect of the notch refill phenomenon would result in NRF transmission measurements that systematically under-predict the areal density of the measured isotope in the target.

The processes that result in notch refill are readily computed using Monte Carlo radiation transport computer codes such as MCNPX[4]. Comparing MCNPX calculations with models that exclude notch refill gives an estimate of the notch refill intensity.

Transmission experiments have previously neglected notch refilling because target areal densities were generally significantly smaller[1, 35, 36]. Thinner target thicknesses are better for measurement of resonant state parameters, but the targets used in this experiment were intended to be representative of nuclear fuel assemblies. These thicker targets cause notch refill to be no longer negligible, and the positioning of DU and Pb in the targets was further selected to maximize the notch refill effect by placement of the Pb, which induced scatter but no absorption, downstream of the absorbing DU.

To obtain values of C_{notch}, simulations of the experimental geometry were conducted using MCNPX and the new NRF data library[39] to obtain $\mathbb{A}(\rho)$. These values were compared to analytical evaluations of $\mathbb{A}_{\text{model}}/C_{\text{notch}}$, giving C_{notch}. Values of C_{notch} are shown in Figure 4.4 for the 2176, 2209 and 2245 keV ^{238}U resonances. The notch refill process is most intense for stronger and lower-energy resonances, and is more important for thicker targets. As seen in Figure 4.4, the effect of notch refill is estimated not to exceed 5% for this experiment.

Columns A - D in Table 4.3 present calculated values of $\mathbb{A}_{\text{model}}(\rho)$ for four different treatments of Equation 4.4. Values in columns A and B assume that the resonance parameters as reported by Heil et al. are correct[24], whereas the values in columns C and D were obtained using the resonance parameters described in ENSDF. Columns A and C assume that $C_{\text{notch}} = 1$, and columns B and D use the estimates of C_{notch} shown in Figure 4.4. The χ^2 values shown in the last row of Table 4.3 are determined by comparing the 18 measured $\mathbb{A}^{i}_{level}$ values to those predicted in columns A - D. Only

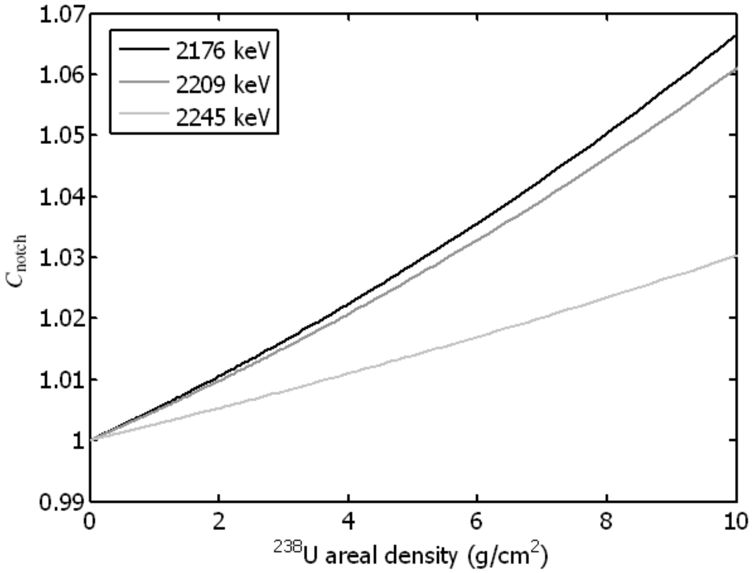

Figure 4.4 Estimated intensities of notch refilling for three ^{238}U resonances indicated by their centroid energy.

the statistical uncertainties of each measurement was used to calculate the reported χ^2 values[1]. Use of the notch-refill correction and the ENSDF evaluation of the resonance parameters (column D) provided the best agreement between data and prediction and therefore this treatment is used to determinate ^{238}U areal densities in the targets as measured by transmission NRF. The predicted attenuation values shown in column B, using the Heil et al. interpretation of the resonance data with the notch refill correction, demonstrates better agreement to the data than either predicted attenuation that omitted the notch refill correction.

Using the values, $C_{\text{notch}}(\rho)$ shown in Figure 4.4 and the resonance parameters from ENSDF, Equation 4.4 is evaluated and values of $\mathbb{A}_{\text{model}}(\rho)$ corresponding to values in column D of Table 4.3 are shown in Figure 4.5. The dotted lines indicate errors due to the uncertainty of Γ_0 from the previous measurement of the ^{238}U resonances.

For each measured value of $\mathbb{A}^i_{level}$ shown in Table 4.3, $\mathbb{A}_{model}(\rho)$ was inverted to obtain an areal density of ^{238}U that would produce the corresponding attenuation. These values were combined for the six known resonances by calculating the weighted average of each estimated areal density. The weighted averages are shown in Table 4.4 with experimental statistical errors and systematic errors due to uncertainties in the strengths of the ^{238}U resonances.

4.5 Conclusion

The determination of ^{238}U areal densities ranging between 1.7 and 8.5 g/cm^2 in an approximately 86 g/cm^2 target by observation of attenuation of resonant-energy photons has been accomplished. While previous transmission measurements using quasi-monoenergetic photon sources have indicated null results for the observation of notch refill[35], the data obtained in this experiment, using thick targets and a bremsstrahlung beam have exhibited a trend indicative of notch refill that could

---

[1] Inclusion of the statistical uncertainties reported by Heil et al. into the χ^2 calculation does not significantly alter the results.

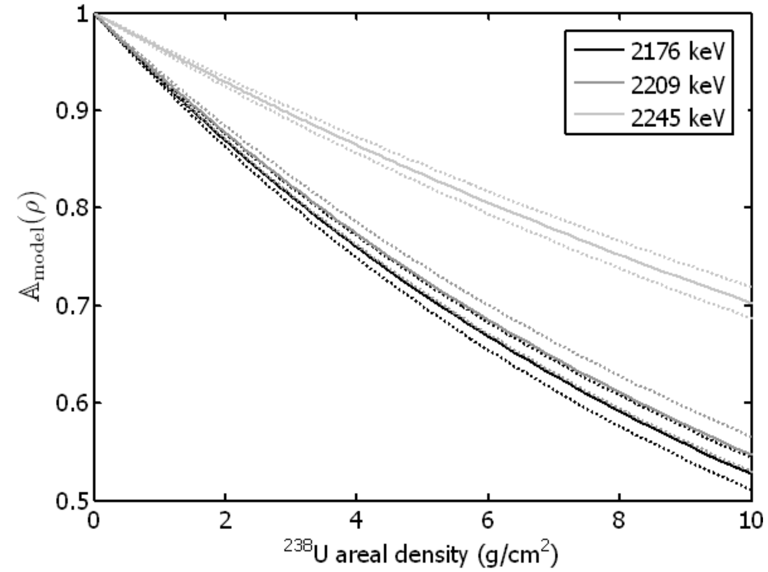

Figure 4.5 Predicted values of $\mathbb{A}_{\text{model}}(\rho)$ for three strongest ^{238}U resonances measured. Dotted lines indicate $\pm 1\sigma$ errors due to uncertainty in the strengths of the resonances from the Heil et al. measurement.

Table 4.4 Values of the measured areal density of ^{238}U obtained by analysis of NRF peaks, and by direct measurement of the mass and area of the ^{238}U plates used in the assay target. The first errors listed for the NRF measurement are 1σ errors due to counting statistics in this experiment. The second stated errors are due to the uncertainties in values of Γ_0 extracted from Heil et al.

Run	NRF-measured ρx (g/cm^2)	direct ρx (g/cm^2)
2	$8.14 \pm ^{0.98}_{0.99} \pm 0.49$	8.47
3	$1.37 \pm 0.68 \pm 0.08$	1.69
4	$3.12 \pm ^{0.73}_{0.76} \pm 0.15$	3.34

increase the measured NRF rate by up to 5% for large resonances and the target containing the most ^{238}U. A correction based on the MCNPX modeling has been implemented in the analysis producing the areal densities measured by transmission NRF. Without the notch refill correction, the data tend to under-predict the areal density of ^{238}U in the target by approximately twice the standard deviation estimated by Poisson counting statistics.

The ^{238}U resonance parameters reported by Heil et al. tend to result in under-predicted ^{238}U areal densities, primarily due to the 2176 and 2209 keV resonances, which were found to be slightly smaller than reported. This could also be due to a slightly larger notch refill correction than indicated by our modeling.

To within statistical uncertainties, the measurement agrees with models used to describe resonant attenuation and subsequent measurement of fluorescence emitted from the transmission detector. However, the results indicate the difficulty of using transmission nuclear resonance fluorescence to precisely measure small quantities of an isotope in an assay target. Rates at which statistics accrue in a transmission measurement are strongly dependent on the strengths of the resonances used for the measurement. Measurements of NRF in ^{235}U and ^{239}Pu have indicated their resonances are smaller than those examined here. This indicates that a transmission NRF measurement that is useful for nuclear safeguards applications would require orders of magnitude more intense photon sources than the 65 μA bremsstrahlung beam used in this experiment. While higher current electron accelerators are commercially available[9], required photon count rates pose difficult challenges for the γ ray detection system.

5 Application of NRF Methods to Safeguards

As described in the previous sections, NRF-based methods provide the potential capability to directly measure the amount of a specific isotope in a material and to perform an isotopic assay. Such a capability can, in principal, be employed across the spectrum of safeguards activities including the assay of spent/used nuclear fuel (SNF), the characterization of reprocessed/fresh or MOX fuel, enrichment measurements in UF_6 containers, and the monitoring of waste and effluent streams. The measurement challenges vary widely. SNF assay is perhaps the most demanding but also the most important application. The challenge for NRF methods lies in the measurement of low concentrations of Pu isotopes and other minor actinides with relatively high accuracies of a few percent or less against a high background from the radioactive decay of fission products. In enrichment measurements on the other hand, the radioactive background is rather low and the concentrations of the IOI can be rather high, but the cylinders can be thick and hard to penetrate.

In this section we analyze three examples of NRF measurements, spent fuel assay, determination of enrichment in UF_6 containers, and measurement of ^{239}Pu in MOX fuel, and discuss potential capabilities and limitations of NRF measurement systems. Based on modeling and MCNPX simulations, NRF detection rates are estimated for backscatter and transmission methods assuming both, the use of currently available technology, i.e., bremsstrahlung photon sources, and of quasi-monoenergetic (QM) photon sources that are currently in an early stage of development. The results are generally expressed in terms of measurement times for a single radiation detector assuming that the use of multiple detectors (a detector array) would proportionally increase the calculated count rates.

5.1 Spent Nuclear Fuel Assay

The Next Generation Safeguard Initiative (NGSI) of the U.S Department of Energy is supporting a multi-lab/university collaboration to quantify the plutonium mass in spent nuclear fuel assemblies and to detect the diversion of pins with non-destructive assay (NDA) methods. Nuclear Resonance Fluorescence (NRF) has been investigated by us as one of 14 NDA techniques included in the study. The results are summarized in this section.

Pu Content in Spent Fuel

In reference[7], Phillips presents calculations of the concentrations of Pu isotopes in spent fuel as a function of fuel burn-up. These values were calculated using the computer code CINDER[8] and are shown in Figure 5.1. Phillips indicates that Pu concentrations are expected to be accurate to ± 10% when the reactor spectrum is well-known, and up to ± 25%, if only the type of reactor is known. Because the Pu concentrations are a function of the reactor type, the Pu concentration values are used to estimate a region of relevant target areal densities. For a typical 15x15 fuel assembly, the average areal densities of ^{239}Pu and ^{240}Pu traversed by photons normally incident upon the side of an assembly are $Nx \approx 0.25$ g/cm^2 and ≈ 0.15 g/cm^2, respectively.

These concentrations are used as reference values throughout the predictive modeling that is described in Sections 5.1.1 - 5.1.2.

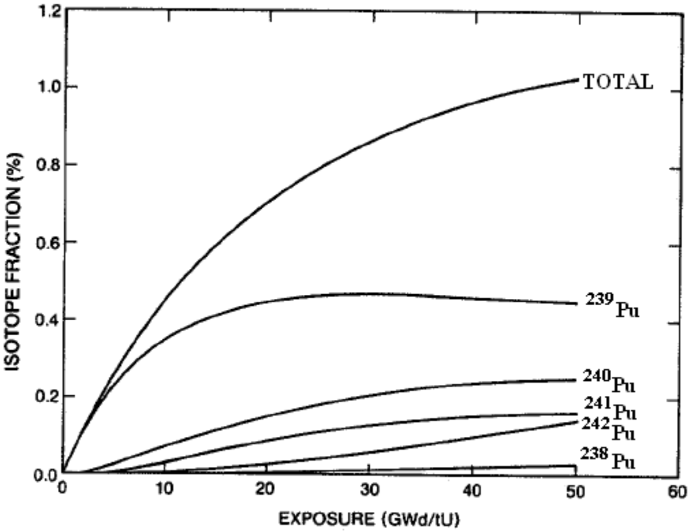

Figure 5.1 Example of computed Pu concentrations in spent fuel as a function of LWR reactor burn-up[7]. The figure is reproduced from this reference. The ordinate is percentage of Pu atoms to the initial uranium atoms present in the fuel.

5.1.1 Measurements Using Bremsstrahlung

The use of currently available intense bremsstrahlung sources for SNF assay is examined in this section. Possible NRF measurements with quasi-monoenergetic photon sources that may become available in the future are analyzed in Section 5.1.2.

5.1.1.1 Backscatter Measurement of Spent Fuel Pins

The geometry for a backscatter measurement on a fuel pin is schematically shown in Figure 2.3. The pin was assumed to be a 10 mm diameter UO_2 cylinder.

Backscattered Background

Photons reaching the radiation detectors that are not due to NRF are considered background. These events may be due to scatter of the interrogating photon beam or radioactive decay in the material to be assayed. Understanding and quantifying this background is important to determine signal-to-noise ratios and detector count rate limitations.

The physical processes that result in photons being emitted at backwards angles relative to the incident photon direction are incoherent scatter, coherent scatter, pair production, and bremsstrahlung emission from photoelectrons. Incoherent scatter produces only low-energy backscattered photons and pair production results in 511 keV photons in all directions. Coherent scattering, on the other hand, produces energetic photons, that are predominantly forward-directed, but also result in some energetic backscattered radiation. Similarly, multi-step processes such as multiple incoherent scattering events or bremsstrahlung emission from energetic photoelectrons can result in energetic backscattered radiation.

The background for the case studied here was simulated in MCNPX. The interrogating radiation was generated with 2.6 MeV electrons incident upon a 102 μm Au foil on a 1 cm thick Cu

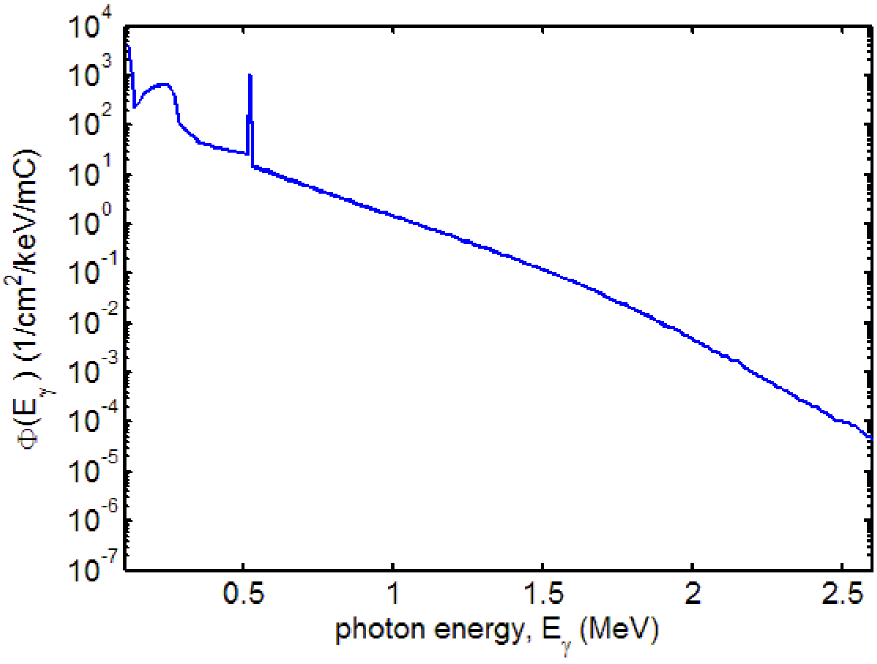

Figure 5.2 Calculated backscattered photon flux for assay of a 5 mm diameter cylinder of spent BWR elements at a detection position 100 cm from the target, at 135° relative to initial electron beam direction. The flux is normalized per mC of 2.6 MeV electrons incident upon bremsstrahlung converter.

backing, (see Figure 2.5). The resulting bremsstrahlung was collimated to 1° half-angle and used to irradiate the UO_2 cylinder 30 cm downstream. The backscattered fluence, shown in Figure 5.2, was calculated 100 cm from the target in a viewing window located at an angle of 135° relative to the direction of the electron beam.

The energy-integrated fluence for the spectrum shown in Figure 5.2 is approximately 1.6×10^5 photons/cm^2/mC. With the front surface area of a large HPGe detector of $\sim$50 cm^2, the detector count rate would be too high with a bremsstrahlung source of reasonable intensity and therefore thick filters (e.g. 7.5 mm of Pb) must be used to reduce the flux of low-energy photons.

The expected background photon flux is shown in Figure 5.2 and the resulting values at resonant energies are tabulated as R_{bkg} in Table 5.1. The total intensity is given by integrating the energy-differentiated spectrum over all energies. This results in 4.6×10^2 counts/mC. Using a 25 mA electron beam to produce the bremsstrahlung beam would then result in approximately 10^4 background counts/s in the counting geometry. Adding the simulated counting rate due to the radioactivity of the spent fuel of 10^4 counts/s, yields a total count rate of $\sim 2 \times 10^4$ counts/s.

NRF Count Rates from Backscatter Assay of Spent Fuel Pin

The NRF rates were calculated using the analytical model for the case of 0.4% of actinide mass, ^{239}Pu, in the SNF pin. The detector response was modeled in MCNPX for a filter thickness of $x_f = 7.5$ cm.

Resulting expected count rates of NRF γ rays from ^{239}Pu are tabulated in Table 5.1. The values are reported in units of counts/mC, indicating that rates are proportional to the intensity of the electron beam that generates the bremsstrahlung beam. For the background continuum,

Table 5.1 Expected rates at which ^{239}Pu NRF γ rays (R_{NRF}), non-resonantly backscattered interrogation photons (R_{bkg}), and photons emitted via radioactive decay spent fuel that has cooled for 11 years (R_{fuel}), are detected at energies corresponding to ^{239}Pu resonance γ rays. The detector was assumed to be a 100% relative efficiency HPGe shielded behind 7.5 cm lead, with assumed energy resolution of 3 keV, 100 cm from the center of the fuel pin at an angle of 135^o , relative to the initial electron beam direction. Values in the last row represent total rates expected over the entire spectrum.

Centroid Energy (keV)	$\int \sigma_{\mathrm{NRF}}\, dE$ (b·eV)	R_{NRF} (1/mC)	R_{bkg} (1/mC)	R_{fuel} (1/s)
2040.3	8	2.5×10^{-5}	4.2×10^{-3}	9×10^{-3}
2135.0	4	1.1×10^{-5}	2.4×10^{-3}	8×10^{-3}
2143.6	13	3.3×10^{-5}	2.2×10^{-3}	8×10^{-3}
2289.0	8	1.6×10^{-5}	6.9×10^{-3}	6×10^{-3}
2423.5	10	1.4×10^{-5}	2.3×10^{-4}	5×10^{-3}
2431.7	9	1.2×10^{-5}	2.2×10^{-4}	5×10^{-3}
2454.4	9	1.1×10^{-5}	1.8×10^{-4}	4×10^{-3}
2464.6	8	9.6×10^{-6}	1.6×10^{-4}	3×10^{-3}
	total	1.3×10^{-4}	4.6×10^{2}	1×10^{4}

the energy-differentiated photon flux is multiplied by the detector's energy resolution, which is assumed to be 3 keV. The expected uncertainties in the rate at which NRF γ rays would be counted are primarily due to experimental uncertainties in the measured strengths of the NRF resonances. These values are up to 33% for the smaller resonances. Likewise, effects due to detector dead-time will proportionally decrease all rates listed in Table 5.1.

Referring to the results shown in Table 5.1, we observe that a beam current of ~200 mA would be necessary for the intensity of NRF γ rays from the 2143 keV ^{239}Pu resonance to be equal to the intensity from the radioactivity of spent fuel, 11 years after reactor discharge. With this beam intensity in mind, we now consider the intensity of non-resonantly backscattered photons, which also scales with the intensity of the interrogating beam.

The significantly larger intensity of the non-resonantly scattered photons and the radioactive decay photons, relative to the NRF γ rays, causes the measurement of backscattered NRF γ rays needed to determine spent fuel content to be difficult. Since longer cooling times can reduce the photon intensity due to radioactive decay in spent fuel, the fundamental limit is defined by the fact that the intensity of NRF γ rays, relative to those non-resonantly scattered, is fixed and small. This indicates that very large numbers of photon counts would be required to precisely measure the quantity of ^{239}Pu in spent fuel. Data from multiple resonances should be combined to improve statistics.

Measurement durations necessary to obtain 5% uncertainties, in units of the product of number of HPGe detectors and time are tabulated in Table 5.2 for several beam intensities. The third column indicates the relative efficiency for a measurement with the stated beam current. The stronger the current, the less significant is the radioactive background. However, in the assumed configuration, currents above 45 mA will begin to induce problematic count rates in an HPGe detector.

The stated measurement times are for a single fuel pin. The measurement times for an exterior

Table 5.2 Measurement durations in units of number of 100% relative efficiency HPGe detectors·time necessary to obtain 5% statistical uncertainty in ^{239}Pu concentrations in a single spent fuel pin for various beam intensities. Also shown are the relative efficiencies of the measurement, which indicates the relative importance of the radioactive background, compared to the beam-on signal.

I_e (mA)	5% (det·day)	Rel. Meas. Eff.
0.10	6.6×10^7	0.11
1.0	8.0×10^4	0.31
10	1.8×10^3	0.65
45	225	0.86
100	88	0.93

row fuel pin of an assembly would be quite similar if a detector were collimated to only view the irradiated portion of the pin. Fuel pins located in deeper rows in an assembly accrue statistics at slower rates due to self shielding by other pins. We therefore conclude that determination of ^{239}Pu concentration in spent fuel via measurement of backscattered bremsstrahlung-induced NRF γ rays is not practical to pursue.

The signal-to-noise ratio, ξ, in the backscatter measurements are well into the small ξ regime, wherein statistical uncertainty in backscatter NRF-measured concentrations scale as $\sigma \propto 1/\sqrt{N\xi}$. This implies the following:

- Detectors that operate at higher (lower) count rates may proportionally increase (decrease) N for a given measurement duration and therefore decrease (increase) σ by $1/\sqrt{N}$;
- Detectors with better (worse) resolution proportionally increase (decrease) ξ for a given measurement and therefore decrease (increase) σ for a given measurement duration by $1/\sqrt{\xi}$;
- Measurement of a material with larger (smaller) NRF resonances produces proportionally larger (smaller) values of N and ξ, thereby proportionally decreasing (increasing) σ for a given measurement.

5.1.1.2 Transmission NRF Assay of Spent Fuel Assemblies with a Bremsstrahlung Source

The concept of performing a transmission measurement to determine Pu content in spent fuel was presented in Section 2.2.2. The method has the following advantages compared to a backscatter measurement:

- the positioning of radiation detectors makes it possible to shield them from radioactivity emitted from the spent fuel;
- measured NRF γ rays have significantly improved signal strengths, relative to the non-resonant photon scatter background; and
- neglecting the small effects of notch refill, the measurement has uniform sensitivity throughout the volume of the irradiated portion of the fuel assembly.

Table 5.3 Expected effective attenuation values, $\mathbb{A}$, signal-to-background ratios of the NRF γ rays, ξ, numbers of counted NRF γ rays due to ^{239}Pu resonances, C, and statistical relative uncertainties, σ_{Nx}, for a simulated assay of ^{239}Pu in a spent fuel assembly. The assay assumes a 24-hour measurement of a fuel assembly containing 0.25 g/cm^2 ^{239}Pu and that the bremsstrahlung source induces 2×10^4 counts per second in each HPGe detector. An * indicates that the corresponding NRF γ ray is due to de-excitation of the NRF state to the first-excited state of ^{239}Pu.

E_{level}	$\mathbb{A}$	ξ	$x_f = 6$ cm	
(MeV)			C	σ_{Nx} (%)
2.040	0.998	0.87	5.1×10^6	39.6
2.144*	0.996	0.59	2.3×10^6	33.8
2.144	0.996	1.91	7.5×10^6	12.8
2.289	0.998	1.91	3.7×10^6	41.4
2.432*	0.996	2.44	3.3×10^6	18.5
2.432	0.996	2.72	3.0×10^6	19.0
2.454	0.998	2.60	2.8×10^6	41.3
2.464	0.998	2.34	2.4×10^6	51.6
total			3.0×10^7	8.3

Transmission methods also generally allow for stronger photon sources than those used in a backscatter measurement. Assuming intense CW electron sources such as a Rhodotron are used to generate bremsstrahlung, the transmission measurement of entire fuel assemblies is more effective than that of a single fuel pin.

Using the modeling described in Section 3 the effectiveness of a transmission measurement of Pu areal densities in spent fuel is examined.

In a transmission assay, the rate at which a particular resonance undergoes NRF in the TD is proportional to the product of the integrated cross section of that resonance, $\mathbb{A}(Nx)$ and the photon intensity incident upon the TD at the resonance centroid energy. Using Table 3.3 and assuming the incident photon spectrum given in Figure 2.8, we estimate relative count rates for each of the ^{239}Pu resonances, and use equation 2.46 to estimate the expected experimental uncertainty in a ^{239}Pu areal density measurement. An example is given in Table 5.3. The example assume that four hundred 100% relative efficiency HPGe detectors are located behind lead filters of thickness $x_f = 6$ and positioned 100 cm from a 4 mm thick TD. The maximum total photon interaction rate in the HPGe detectors is conservatively assumed to be 2×10^4/s. In this geometry, 1/3 of the total available backward solid angle is subtended by the detectors.

The uncertainties expected from a 24 hour measurement using a 42 mA beam are listed for each resonance. An estimate of the total uncertainty of the areal density of ^{239}Pu is determined from a weighted mean of the measured areal densities from each resonance and, based solely on counting statistics, is given in the last row of Table 5.3. Systematic errors are not included since counting statistics is the major challenge with existing technology.

Other Pu isotopes of interest in spent fuel are ^{240}Pu and ^{242}Pu while the NRF responses have not been measured yet, nuclides with even numbers of neutrons and protons generally have stronger NRF resonances than those with at least one unpaired nucleon such as ^{239}Pu[1]. With this

---

[1] See for example, references[30],[31], and[32]

Table 5.4 Summarizing the effects on maximum beam current, I_e, and the resulting fractional areal density statistical uncertainties, σ_{Nx}, when a LaBr$_3$ detector array is used instead of HPGe. The * indicates that ^{240}Pu resonances are unknown and that known ^{238}U resonances were used for this calculation instead.

		HPGe		LaBr$_3$	
	σ_E	1.3 (keV)		23 (keV)	
	$\dot{C}_{max}$	2×10^4/s		3×10^5/s	
	x_f	4 cm	6 cm	4 cm	6 cm
	I_e (mA)	7.8	42	117	630
^{239}Pu	σ_{Nx} (%)	11.4	8.3	9.3	6.53
^{240}Pu*	σ_{Nx} (%)	1.4	0.98	1.0	0.54

in mind, we estimate the accuracy to which a measurement of the ^{240}Pu content in a spent fuel assembly might be obtained. Assuming that the ^{238}U NRF state characteristics shown in Table 3.5 are representative of the ^{240}Pu resonances, we can calculate the total statistical uncertainty for the ^{238}U resonances assuming an areal density in spent fuel of 0.15 g/cm^2.

The assumed strong resonances could reduce measurement times by a factor of 70 compared to ^{239}Pu. A 24 hour measurement could achieve 1% precision, or a 5% precision measurement could be done in 1 hour.

Measurement of Pu in Spent Fuel using Alternative Detector Types

Whereas NRF γ rays measured in backscatter measurements were determined to be significantly weaker than background photon intensities within any known detector's resolution, this is not the case for a transmission measurement. Because of this, worsening detector resolution does not reduce the precision of the measurement by $1/\sqrt{\xi}$, but rather produces a more complicated and less severe effect. Conversely, detectors that can operate at higher count rates would allow significantly stronger beams and/or thinner filters. We explicitly consider the use of LaBr$_3$, which can easily tolerate ~15 times higher count rates than HPGe detectors, and evaluate two cases with 4 cm and 6 cm thick filters, respectively. The expected uncertainties for a 24 hr transmission measurement using 400 LaBr$_3$ detectors of similar size to 100% relative efficiency HPGe detectors were calculated. The beam intensities, I_e, corresponding to the given detector count rates and the resulting fractional areal density statistical uncertainties, σ_{Nx} for these geometries are presented in Table 5.4.

These results indicate that lower-resolution detectors capable of significantly higher count rates may be capable of providing 20% - 40% lower statistical error (higher precision) but for the price of a needed 10-fold increase in electron beam current. Better precision transmission measurements of Pu in spent fuel, so long as bremsstrahlung beam intensity may be increased such that detectors are rate-limited.

From the examples presented in this section, we draw the following conclusions:

- backscatter measurements of ^{239}Pu concentration in SNF is not practical, and it is unlikely that ^{240}Pu would have sufficiently strong NRF resonances to make backscatter measurements of ^{240}Pu practical;

- transmission measurements of ^{239}Pu concentration with bremsstrahlung would be even more time-consuming, requiring $\sim 2 \times 10^4$ detector·days to obtain 1% counting statistics;
- if ^{240}Pu resonances are as large as those in ^{238}U, transmission measurements of ^{240}Pu concentration to 1% uncertainty would still take ~200 detector·days, which is possible even if not practical.
- Measurements with a statistical uncertainty of several percent would only take 1/10 of the time and reduce measurement time and/or the size of the detector array accordingly.

5.1.2 Spent Fuel Assay Using Quasi-monoenergetic Photon Sources

The ideal photon source for an NRF measurement would be a monoenergetic beam that excites a particular resonance of interest and generates a minimal scattered photon background. Quasi-monoenergetic (QM) photon sources that produce a narrow source photon energy distribution based on the Compton up-scattering of laser light are under development to produce intense photon beams with 1 - 10 keV energy width. This source type is briefly described in Section 2.3.1.

In the analysis of NRF systems using QM sources it is mostly assumed that the source delivers a continuous beam. However, laser Compton sources are pulsed in nature. If the pulse rate of a hypothetical source is sufficiently high, it may be considered approximately continuous. Lower frequency sources require more detailed consideration, and would best be combined with threshold (Cherenkov) detectors as discussed below.

5.1.2.1 Backscatter Measurement with Quasi-monoenergetic Photons

Analogous to Section 5.1.1.1, we consider here the possibility of directly measuring the rate at which Pu in spent fuel undergoes NRF when irradiated with a QM photon source. To study this measurement scenario, we divide the calculation into four parts:

- Backscatter of resonant-energy photons;
- Backscatter of non-resonant photons;
- Radioactive background due to spent fuel activity; and
- Detector response.

Backscattered Photon Spectra

We assume a QM beam that is uniform in intensity over an 8 eV range and sufficiently narrow to be considered incident upon only a single row of fuel pins in an assembly. The mean energy of the beam was taken to be the centroid energy of the 2431 keV ^{239}Pu resonance. Likewise, we assume HPGe detectors are collimated and positioned to view only a single fuel pin within the irradiated row of fuel pins. To simulate this, the probability of photons interacting within fuel pins that are outside of the collimator viewing angle were explicitly excluded from directly contributing to the calculated photon flux. A schematic of the geometry simulated in MCNPX is shown in Figure 5.3. The portions of the fuel lattice that are differently colored indicate regions within which photons interacting are considered to directly contribute to the calculated flux.

The resonantly and non-resonantly backscattered photon fluences were calculated with identical MCNPX runs, except NRF datafiles were excluded from the non-resonant photon scatter calculations. The photon source is assumed to be non-diverging, normally incident upon the fuel assembly, centered at the row of pins adjacent to the center row (which has several void locations), and uniformly distributed throughout a 6.3 mm radius circle.

Two tallies were performed, each giving the expected photon fluence at a hypothetical detector location. Both locations were 100 cm from the row of fuel pins that were irradiated, at an angle of 125^o from the initial beam trajectory. One tally simulated a detector collimated to view the 3rd fuel pin in the row of irradiated fuel, and the second simulated a detector collimated to view the 13th fuel pin. The spectra calculated at each detector position are shown in Figures 5.4 and 5.5,

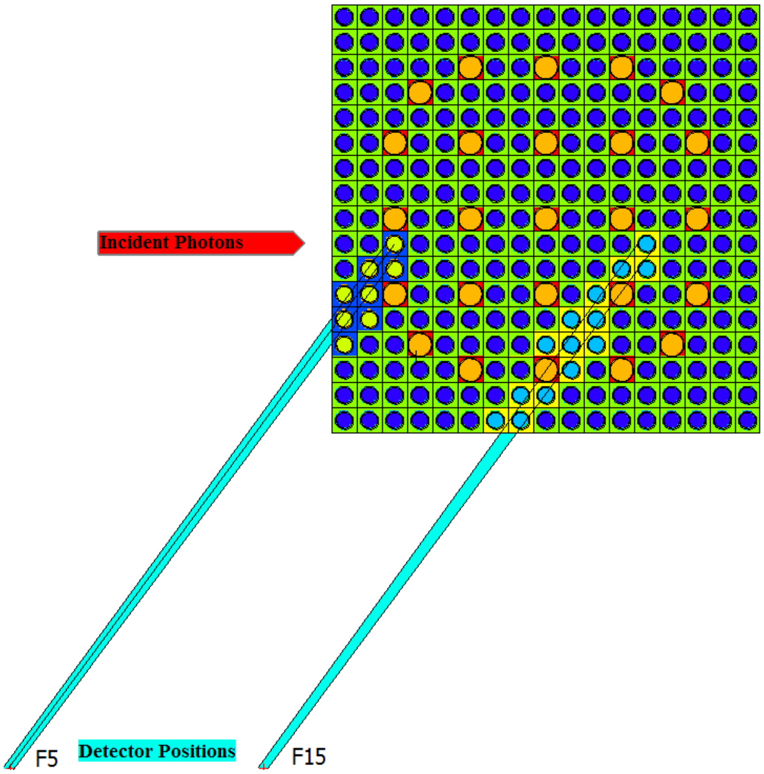

Figure 5.3 Geometry simulated in MCNPX to determine energy-dependent flux of backscattered QM photons incident upon a spent fuel assembly.

where the blue lines indicate the spectrum resulting when NRF physics is included, and the red when NRF is excluded. The reason that a full energy peak remains when NRF is disabled is due to the fact that non-resonant elastic scatter (NRES) is still possible. The cross section for NRES is significantly smaller than that for NRF, however all isotopes in the spent fuel are capable of undergoing NRES, whereas presumably, only the ^{239}Pu at 0.4wt.% undergoes NRF at this energy. At full energy, the calculated intensities of NRF γ rays divided by the intensities calculated without NRF is 7.2 for both pins. This value is roughly the maximum possible signal-to-background ratio, ξ_{max}, that a QM backscatter measurement of the 2431 keV ^{239}Pu resonance could attain. However, most QM photon sources are at least 100 times broader in energy, resulting in signficantly worse ξ. For $\sigma_S > \Delta E_{\text{det}}$, realistic signal-to-background ratios, ξ, using QM photons are determined by the detector resolution. The ratio can be estimated as

$$\xi_{real} \approx \frac{\xi_{MonoeE}\Delta E_{src}}{\Delta E_{\text{det}}} \approx \frac{1}{50} \tag{5.1}$$

for these simulations, in which $\Delta E_{src} = 8$eV and $\Delta E_{\text{det}} = 3$ keV HPGe detector. The ramifications of poor signal-to-background will be discussed below.

Values describing the total calculated spectra for these runs are given in Table 5.5. The column labeled Φ_{ES} is the intensity of the full-energy peak in the simulation that excluded NRF physics, Φ_{NRF} is the sum of photons that are expected to be due to NRF, $\Phi_{\text{NRF}} = \Phi(E = 2431) + \Phi(E = 2423) - \Phi_{ES}$. The fraction of the total flux that is due to photons of energy 511 keV or less is quite large. This implies that if necessary, absorbers could be placed between the fuel assembly

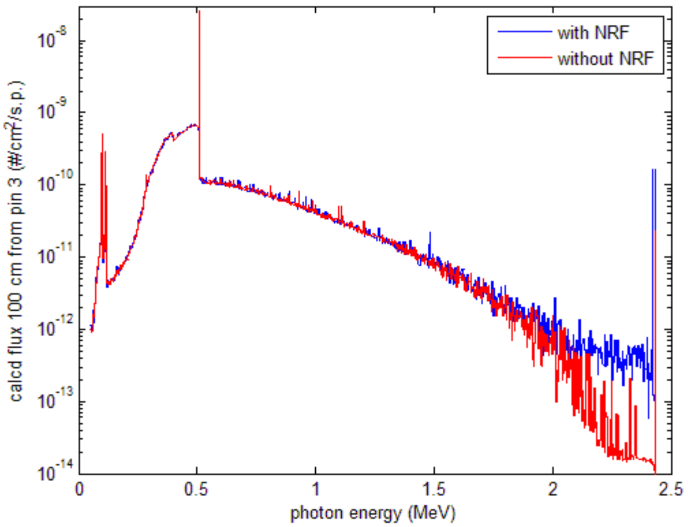

Figure 5.4 MCNPX-computed spectrum due to backscatter of monoenergetic photons at resonant (blue) and a nearby non-resonant (red) energies incident upon a single row of a spent fuel assembly. These spectra correspond to the labeling 'F5' in Figure 5.3.(3^{rd} pin)

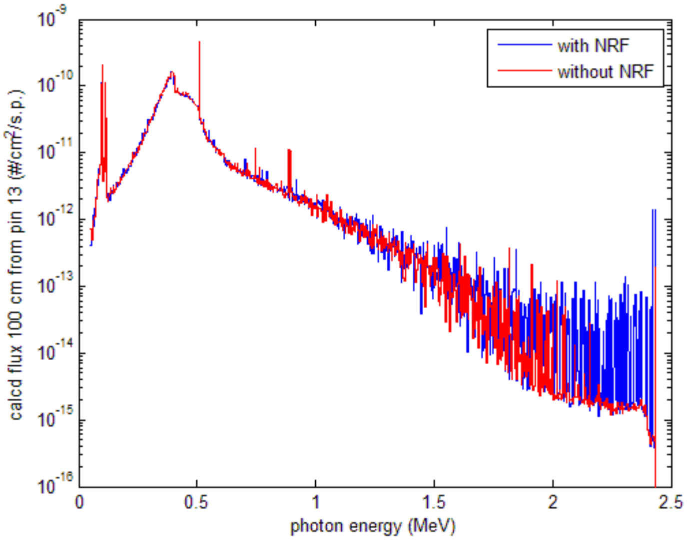

Figure 5.5 MCNPX-computed spectrum due to backscatter of monoenergetic photons at resonant (blue) and a nearby non-resonant (red) energies incident upon a single row of a spent fuel assembly. These spectra correspond to the labeling 'F15' in Figure 5.3. (13^{th} pin)

Table 5.5 Parameters describing average spectra due to a single monoenergetic photon incident upon a spent fuel assembly with resonant energy that are backscattered towards detectors that are collimated to view the 3rd and 13th row of pins, respectively. $\frac{\Phi(E<511)}{\Phi_T}$ and $\frac{\Phi(E=511)}{\Phi_T}$ indicate the fraction of the total calculated flux that are due to photons with energies less than, and equal to 511 keV, respectively. Φ_{NRF} is the expected flux of NRF γ rays per source photon, Φ_{ES} is the expected flux due to non-resonant elastic scatter of source-energy photons, and Φ_T is the expected total flux of photons due to monoenergetic, monodirectional photons normally incident upon a 1 cm diameter portion of a fuel assembly.

tally pin	$\frac{\Phi(E<511)}{\Phi_T}$	$\frac{\Phi(E=511)}{\Phi_T}$	Φ_{NRF} (1/cm^2/ph)	Φ_{ES} (1/cm^2/ph)	Φ_T (1/cm^2/ph)
3	0.44	0.33	3.1×10^{-10}	2.4×10^{-11}	7.83×10^{-8}
13	0.80	0.05	2.7×10^{-12}	2.0×10^{-13}	7.96×10^{-9}

and photon detectors to reduce the low-energy photon count rate and therefore the total count rate of a detector.

Neglecting the contribution to the background count rate due to radioactive decay of spent fuel, we may use the values in Table 5.5 to determine the best-case counting parameters necessary to make a measurement of ^{239}Pu content in spent fuel using backscattered NRF γ rays. For simplicity, we assume that photons will be detected with a 100% relative efficiency HPGe detector of surface area, $A_{det} = 50$ cm^2. To make a 1% measurement, we would normally require 10^4 NRF counts. However, due to the very poor signal intensity, relative to background ($\xi = 1/50$), we estimate using equation 2.15 that $C_{\mathrm{NRF}} = 10^5$ NRF counts are necessary. Given that NRF γ rays have a full-energy deposition probability for the detector, $\epsilon_{\mathrm{NRF}} = 0.2$, we would need

$$N_{res} = \frac{C_{\mathrm{NRF}}}{\epsilon_{\mathrm{NRF}} A_{det} \Phi_{\mathrm{NRF}}} = 3.22 \times 10^{13} \tag{5.2}$$

photons within ±4 eV of the resonance centroid energy to make this measurement on a fuel pin in the third layer with a single HPGe detector. Likewise, a 1% measurement of a pin in the 13th row of fuel would require 3.70×10^{15} photons within ±4 eV of the resonance centroid energy. For example a proposed (LLNL[14]) QM photon source is to generate 10^6 photons/eV/s. With this source, a 1% measurement of the 3rd row of fuel pins would require 4×10^6s of active detectors, or approximately 1200 detector·hours.

For beams with realistic energy bandwidth detector count rate limitations are important. A summary of the constraining parameters of such a system is shown in Table 5.6 for various source widths and HPGe detectors (assuming 3 keV resolution and a maximum count rate of 2×10^4Hz).

Revisiting the possible use of the proposed (LLNL) quasi-monoenergetic photon source, and assuming $\sigma_S \approx 2,500$ eV, we observe that approximately 63 detector·days would be necessary to perform the 1% meaurement, indicating this measurement would be possible to conduct in 1 day using a 63-HPGe detector array. Likewise, more intense photon sources (in terms of total number of photons on target per second) would generally saturate unshielded HPGe detectors, which would necessitate the use of a filter, which is discussed below in the context of filtering spent fuel radioactivity.

Table 5.6 Backscatter measurement parameters for 1% measurment of ^{239}Pu in spent fuel assembly for third row of pins, neglecting fuel radioactivity. HPGe detectors have been assumed to have 3 keV resolution and to operate at 2×10^4Hz.

σ_S (keV)	$\Phi_{\rm NRF}\frac{N_T}{N_{\rm NRF}}$ (1/cm^2/ph)	ξ	$C_{\rm NRF}$ counts	C_T counts	t_{meas} (det·day)	intensity (1/eV/s)
0.1	1.0×10^{-11}	0.42	2.4×10^4	9.5×10^8	0.55	2.0×10^7
1	1.0×10^{-12}	0.042	7.0×10^4	2.8×10^{10}	15.6	2.0×10^6
2.5	4.0×10^{-13}	0.017	1.1×10^5	1.1×10^{11}	63	8.2×10^5
3	3.3×10^{-13}	0.014	1.2×10^5	1.4×10^{11}	82	6.8×10^5
10	1.0×10^{-13}	0.014	1.2×10^5	4.7×10^{11}	274	2.0×10^5
100	1.0×10^{-14}	0.014	1.2×10^5	4.7×10^{12}	2740	2.0×10^4

Table 5.7 Backscatter measurement parameters for 1% measurment of ^{239}Pu in spent fuel assembly for third row of pins, when 3 inch Pb filter is present. HPGe detectors have been assumed to have 3 keV resolution and to operate at 10^4Hz due to beam photons and 10^4Hz due to radioactive decay in spent fuel.

σ_S (keV)	$\Phi_{\rm NRF}\frac{N_T}{N_{\rm NRF}}$ (1/cm^2/ph)	ξ	$C_{\rm NRF}$ counts	C_T counts	t_{meas} (det·day)	intensity (1/eV/s)
0.1	1.0×10^{-11}	0.42	2.4×10^4	9.5×10^8	0.07	6.1×10^9
1	1.0×10^{-12}	0.042	7.0×10^4	2.8×10^{10}	2.1	2.0×10^8
2.5	4.0×10^{-13}	0.017	1.1×10^5	1.1×10^{11}	8.4	2.4×10^8
3	3.3×10^{-13}	0.014	1.2×10^5	1.4×10^{11}	11	2.0×10^8
10	1.0×10^{-13}	0.014	1.2×10^5	4.7×10^{11}	37	6.1×10^7
100	1.0×10^{-14}	0.014	1.2×10^5	4.7×10^{12}	366	6.1×10^6

Impact of Spent Fuel Radioactivity on Backscatter Measurement

The assay geometry depicted in Figure 5.3 is quite similar to that considered in Section 5.1.1.1. In this section, it was determined that approximately 7.5 - 10 cm of Pb would need to be placed in the collimator opening between an HPGe detector and the portion of the interrogated fuel assembly that is within the line of sight. 7.5 cm of Pb will attenuate 2431 keV photons by a factor of 40, and the total count rate due to scattered interrogating photons by a factor of 600. With this filter, we re-present the measurement parameters in Table 5.7. For sources with a broader energy width, the signal-to-background ratios are not significantly changed and measurement times actually decrease due to filtering of the low-energy portion of the backscattered spectrum. However, the necessary source intensity to achieve the tabulated rates are increased by a factor of approximately 40.

The expected count rate of background photons that a 100% relative efficiency detector in this geometry, located behind 7.5 cm of Pb, measures is approximately 10^4/s. The previously referred to proposed QM photon source, producing 10^6 photons/eV/s on target, would now induce ~30 counts per second in a reference detector and 6×10^{-4} NRF counts/s. Therefore the assumption in the preceeding section that detector count rates are satuarated due to counting of interrogating source photons would require significantly more intense photon beam, as indicated in Table 5.7. The expected count rate of radioactive decay photons contributing background at 2431 keV would

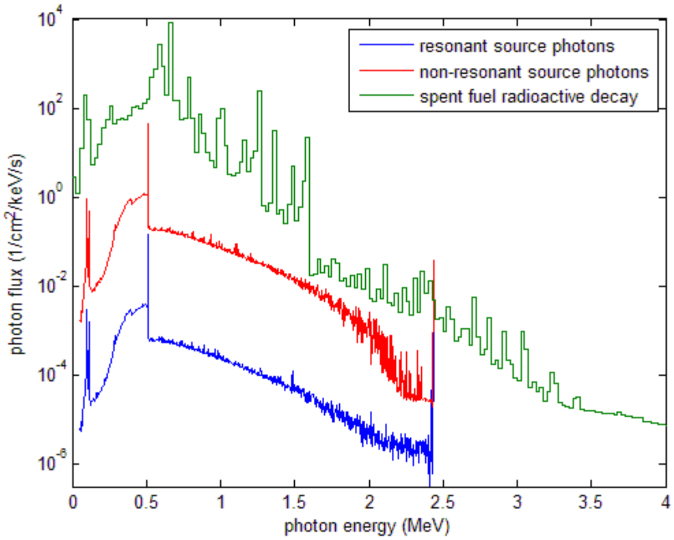

Figure 5.6 Relative intensities of photon fluxes due to scattering of resonant (blue) and non-resonant (red) interrogating source photons compared with the intensity of background photons (green).

contribute a count rate of 3×10^{-3}counts/3keV/s. This would further decrease the signal-to-background ratio, ξ, for the NRF signal (from 0.017 to 0.015) for proposed sources, but would have very little effect on ξ for very intense sources. The time that a 1% measurement would take using the LLNL-proposed source would then increase by a factor of 43 from 50 detector·days to 2.2×10^{3} detector·days.

Use of Threshold Detectors

Radiation detectors that are only sensitive to photons above a threshold energy do not necessarily significantly improve the prospect of making a measurement of ^{239}Pu content in spent fuel via a backscatter measurement unless the detector can also resolve the energy of detected photons, or can be used with a pulsed QM photon source to reduce the background rates through time-gating.

Without time gating, the issue of background can be illustrated by comparing the photon spectra shown in Figure 5.4 with a simulated spectrum of the emitted γ-ray spectrum from the radioactivity in a SNF assembly as is shown in Figure 5.6.

Threshold detectors effectively integrate the photon flux above some minimum energy E_{min}, possibly with a response function. The most optimistic threshold detector response model would be that of a step function and $E_{\text{min}} = 2.4$ MeV. In this case, the NRF signal would represent just 1.8×10^{-4} of the measured signal, implying that statistics would accrue about 100 times slower than if the threshold detector primarily measured NRF signals, with most of the signal coming from the radioactive background and the non-resonant source photons.

However, if the QM photon source is pulsed, like the QM sources described in Section 2.3.1 with 10 ps bunches at $f = 120$ Hz, detectors that measure single photons will be limited to very low acquisition rates. Conversely, integrating threshold-type detectors could be configured to measure an integrated signal only during the beam pulse. Assuming a time resolution σ_t of 1 ns, the measured intensity of radioactive background photons would be reduced by a factor of $\sigma_t \times f = 1.2 \times 10^{-7}$. In this case, systems with threshold detectors and pulsed QM photon sources would measure a negligible radioactive background and would thus be able to measure spent fuel. Depending on the sharpness of the threshold that could be implemented, the signal-to-background ratios could reach those indicated for $\sigma_S \leq 3$ keV in Table 5.6. QM sources with a wider energy spread would result in proportionally smaller values of ξ.

Conclusions for Backscatter Measurements Using Quasi-monoenergetic Sources

The best-case scenario for using NRF to measure Pu content in spent fuel is to use a truly monoenergetic photon source of arbitrary intensity and a detector with good energy resolution that is not count rate-limited. In this case, the NRF signal due to the strongest ^{239}Pu resonances is approximately 10 times background (for 3 keV energy resolution detectors), and measurement of 10^4 NRF counts would provide $\sim$1% counting statistics. In the geometry in which the detector-TD distance was 100 cm, as described in Section 5.1.2.1, this would require 8×10^{11} source photons for a single 100% relative efficiency detector to measure the third row of pins. More detectors would proportionally reduce the necessary number of source photons, i.e., an array of 100 such detectors would require 8×10^9 source photons.

This ideal scenario is unrealistic in three ways: energy-resolving detectors are incapable of measuring arbitrary count rates and photon sources can neither be arbitrarily intense, nor truly monoenergetic. The problem of detector rate limitations becomes foremost because it limits source beam intensities and necessitates shielding from the spent fuel radioactivity, which causes more source photons to be required to obtain the same number of NRF counts. Photon sources with broader energy distributions reduce the signal-to-background ratio, requiring longer counting times to obtain the same statistics.

If the QM source is pulsed, energy-resolving detectors may operate at average rates that are significantly lower than the nominal rate limit, resulting in increased counting times. Threshold detectors are not rate limited, and could be gated to reject radioactive background photons between photon source pulses. This could result in significant improvements for backscatter measurements using very intense QM sources. A best-case scenario would be the use of a $\sim 10^8$ photons/eV/s, $\sigma_S = 2.5$ keV source inducing NRF that is measured by an ideal Cherenkov detector array. With $\xi = 0.017$, this measurement would take 12 hours using a single detector with a 50 cm^2 area and an efficiency comparable to the full-energy efficiency of HPGe ($\sim$20%). An array of 80 such detectors could then accomplish a measurement with 1% statistical uncertainty in 10 minutes. While this indicates the promise of NRF, neither the detectors nor the photon source presently exist. Construction of demonstration QM sources of 10^6 photons/eV/s intensity have been proposed, and aerogel Cherenkov materials could potentially produce acceptible threshold characteristics[33, 34].

In summary, we observe the following for backscatter measurements:

- Increasing the QM source intensity from the proposed LLNL design to 2×10^8 ph/eV/s would proportionally reduce the necessary count time. Above this intensity, detector count rates would become the limiting factor and increased source intensities would require additional filter thicknesses to reduce count rates;

- Narrower than 2.5 keV bandwidth beams would represent an improvement in ξ and could potentially produce up to a factor of 8 decrease in measurement time;

- Broader bandwidth beams would not necessarily worsen the system performance, but would reduce the allowable increase in beam intensity before which additional filter thickness would be necessary, thus leading to longer measurement times;
- Improved detector energy resolution (over the 3 keV FWHM resolution assumed here) would result in proportionally better values of ξ, and proportionally shorter measurement times (until $\sim$5 eV resolution is achieved);
- Worsened detector energy resolution results in proportionally longer measurement times until separate peaks cannot be resolved;
- Detectors capable of higher measurement rates proportionally decrease counting times and reduces necessary filter thickness, which further reduces counting times but also reduces the allowable increase in beam intensity or width;
- Measurements with gated threshold detectors and a pulsed photon source would largely be insensitive to the radioactive background and would thus be suitable for backscatter assay.

5.1.2.2 Transmission Measurements Using Quasi-monoenergetic Sources

Because the transmission measurements rely on a transmission detector, the radiation detectors are not directly exposed to the large photon intensity due to radioactive decay in the used fuel assembly. Therefore we are able to consider the transmission measurement of a fuel assembly without directly considering the influence of the radioactive background. Analogous to Section 5.1.2.1, we divide the problem of measuring used fuel into several independent calculations:

1. Transport of resonant-energy photons;
2. Transport of non-resonant photons; and
3. Detector response.

The transport of resonant and non-resonant photons were simulated in MCNPX in two assay geometries, both of which use monodirectional, monoenergetic photons to irradiate fuel in a 17x17 fuel assembly. In one geometry, the photon source is normally incident upon a full row (17 pins) adjacent to the center of the fuel assembly (labeled ‘A’ in Figure 5.7). In the other geometry, the photon beam is assumed incident upon the assembly at an angle, 33° from normal. The red lines in Figure 5.7 represent the trajectories of the source photons through a fuel assembly for these two source geometries. The thicknesses of material through which the simulated photons penetrate as they traverse the fuel (assuming no interaction) are given in Table 5.8.

Beyond the fuel assembly, a TD is placed in the trajectory of the interrogating photon beam. For these simulations, the TD was assumed to be a 1 cm thick plate of pure ^{239}Pu with a 10 cm diameter. In a real system the diameter of the TD would be as small as the transmitted beam and considerably thinner than 1 cm. Finally, the photon flux, resulting from backscattered photons emitted from the TD is determined at a position 100 cm along a ray leaving the center of the TD at a 120° angle, relative to the initial photon beam trajectory.

Spectra calculated for geometry B, using MCNPX and the modified photonuclear data files are shown in Figure 5.8. Table 5.9 presents parameters describing the spectra shown in Figure 5.8, as

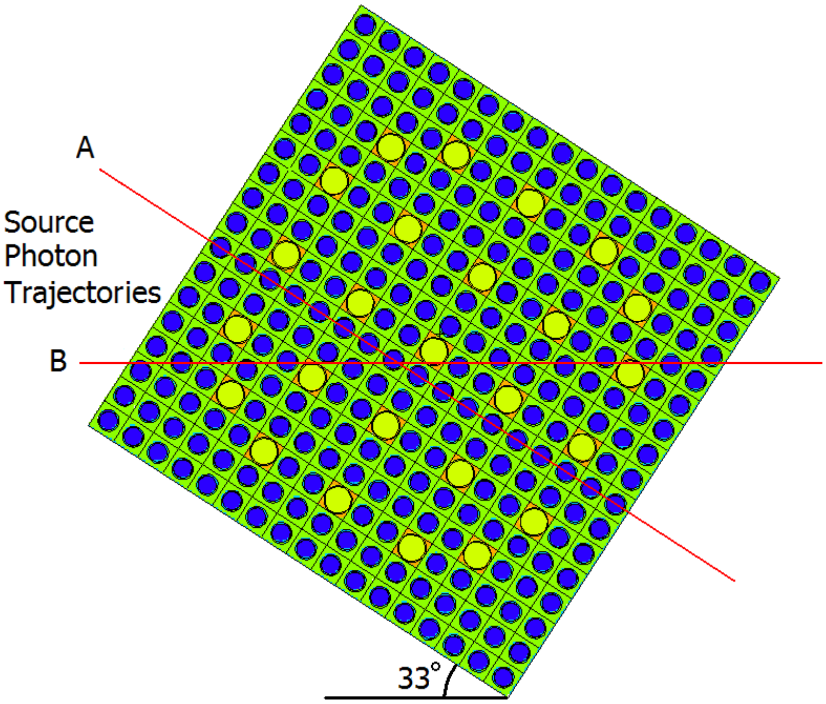

Figure 5.7 Schematic describing the source photon trajectories for the two different geometries of monoenergetic transmission measurements considered. The red lines indicate rays describing the trajectory of the source photons for the two geometries, labeled ‘A’ and ‘B’.

Table 5.8 Thicknesses of materials traversed by rays depicting monodirectional source trajectories in two source geometries.

Source Geometry	UO_2 (cm)	Zr Clad (cm)
A	13.940	2.210
B	7.654	2.700

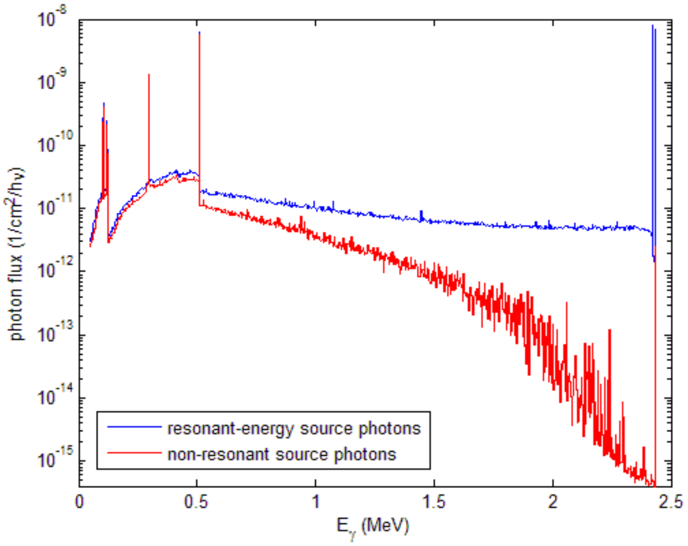

Figure 5.8 MCNPX-computed spectra due to a transmission measurement of a fuel assembly containing no ^{239}Pu using monoenergetic photons at resonant (blue) and a nearby non-resonant (red) energies incident upon a spent fuel assembly as indicated by Geometry B in Figure 5.7.

well as those spectra that result from a photon beam incident as depicted in geometry 'A'. Similar to the simulation of the backscatter method, the intensities in Table 5.9 may be scaled to the intensities of resonant and non-resonant source photons and summed to determine the expected spectrum due to a given QM photon source distribution.

Computed Photon Spectra using Quasi-monoenergetic Sources

A series of simulations were conducted using Gaussian beam source energy profiles centered on the 2.431 MeV ^{239}Pu resonance, the irradiation geometry labeled 'A' in Figure 5.7, and with ^{239}Pu content of 0% and 3.62wt.%. Using these simulations, the analytical attenuation model can be tested against MCNPX, the NRF signal intensity can be compared to the calculated background intensity, and the expected rates at which NRF and non-NRF γ rays would be measured can be determined.

The intensity of the 2431 keV NRF γ ray compared to background was determined in two ways; for photon source distributions wider than the tally energy bin width, a Gaussian distribution was fit to the calculated peak due to non-resonant elastic scatter of source photons. For narrower source distributions, MCNPX calculations were also performed where the NRF process was turned off. Comparing spectra for identical runs with and without NRF indicates the relative intensity of the NRF γ rays, relative to the non-resonant elastic scatter. Figure 5.9 presents the calculated relative intensity of NRF γ rays at 2431 keV, relative to the calculated intensity of non-resonantly scattered photons that would be incident upon a detector.

As expected, the intensity of NRF γ rays, relative to background increases when a larger fraction of the source photons are resonant-energy, as occurs with a narrower source. This effect becomes most pronounced when the width of the beam becomes less than the assumed detector resolution, at which point reducing σ_S produces a smaller elastic scatter contribution. Using equation 2.15, we observe that the number of NRF counts needed to make a measurement of a

Table 5.9 Parameters describing average spectra due to a single monoenergetic photon with $E = 2431$ keV incident upon a spent fuel assembly that penetrate the fuel assembly, impinge upon the TD , and are backscattered toward a detector located 100 cm from the TD at an angle of 120°, relative to the initial beam direction. The energies of the monoenergetic photons were either considered to be that of the centroid energy of the 2431 keV ^{239}Pu resonance, or sufficiently distant from this energy that the resonance would have no impact on the transport of the photons. The geometry of the incident photon beam, relative to the assembly is depicted in Figure 5.7. $\frac{\Phi(E\leq511)}{\Phi_T}$ indicates the fraction of the total calculated flux that are due to photons with energies $\leq$ 511 keV. Φ_{NRF} is the expected flux of NRF γ rays per source photon, Φ_{ES} is the expected flux due to non-resonant elastic scatter of source-energy photons, and Φ_T is the expected total flux of photons due to monoenergetic, monodirectional photons normally incident upon a 1 cm diameter portion of a fuel assembly.

beam geometry	$\frac{\Phi(E\leq511)}{\Phi_T}$	Φ_{NRF} (1/cm^2/ph)	Φ_{ES} (1/cm^2/ph)	Φ_T (1/cm^2/ph)
A_{res}	0.41	3.6×10^{-9}	7.0×10^{-13}	8.2×10^{-9}
A_{nr}	0.88	0	7.0×10^{-13}	3.3×10^{-9}
B_{res}	0.37	1.5×10^{-8}	2.7×10^{-12}	3.3×10^{-8}
B_{nr}	0.87	0	2.7×10^{-12}	1.2×10^{-8}

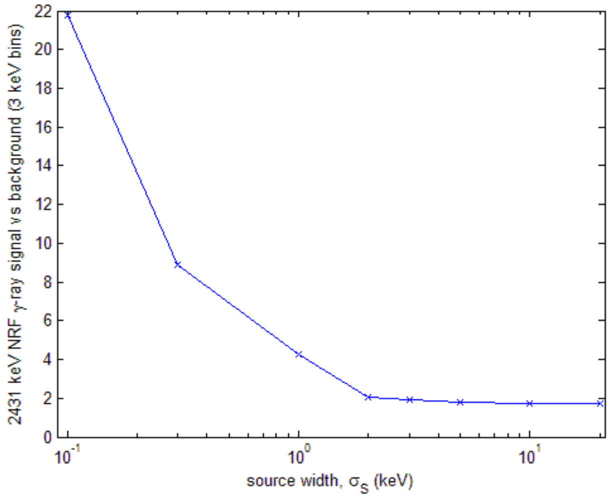

Figure 5.9 Calculated ratios of 2.431 MeV NRF γ-ray flux at a detector location, relative to background flux (ξ) within a 3 keV energy bin. Statistical errors are less than 2%.

Table 5.10 Transmission measurement parameters necessary to perform 1% measurment of ^{239}Pu in spent fuel assembly in Geometry 'A', where $\rho_{\mathrm{Pu}} = 0.72\mathrm{g/cm}^2$, assuming HPGe detectors operate at 2×10^4Hz.

σ_S (keV)	$\Phi^{\sigma_S}_{\mathrm{NRF}}$ (1/cm^2/ph)	$\Phi^{\sigma_S}_{\mathrm{T}}$ (1/cm^2/ph)	ξ	NRF counts	t_{meas} (det·day)	intensity (1/eV/s)
0.1	3.14×10^{-11}	3.34×10^{-9}	22.4	8.21×10^{7}	25.3	3.98×10^{8}
0.3	1.05×10^{-11}	3.31×10^{-9}	7.47	9.55×10^{7}	87.6	1.34×10^{8}
1	3.14×10^{-12}	3.30×10^{-9}	2.59	1.34×10^{8}	407	4.02×10^{7}
2	1.57×10^{-12}	3.30×10^{-9}	2.05	1.49×10^{8}	907	2.01×10^{7}
3	1.05×10^{-12}	3.30×10^{-9}	1.95	1.53×10^{8}	1.4×10^{3}	1.34×10^{7}
5	6.27×10^{-13}	3.30×10^{-9}	1.90	1.55×10^{8}	2.4×10^{3}	8.06×10^{6}
10	3.14×10^{-13}	3.30×10^{-9}	1.88	1.56×10^{8}	4.7×10^{3}	4.03×10^{6}
20	1.57×10^{-13}	3.30×10^{-9}	1.87	1.56×10^{8}	9.5×10^{3}	2.01×10^{6}

given precision is twice as many for a $\sigma_S = 20$ keV source than for a $\sigma_S = 100$ eV source.

Using HPGe Detectors

Using equation 2.46 and the exponential constant, α that relates areal densities to the effective resonant attenuation, (=0.016 g/cm^2 from Table 3.3 for the 2.431 MeV resonance), we can derive an expression for the necessary number of counts, C_{NRF}, to measure an areal density, ρ_{Pu}, of ^{239}Pu in spent fuel to a precision given by the fraction uncertainty, $\epsilon/\rho_{\mathrm{Pu}}$,:

$$C_{\mathrm{NRF}} = \frac{1 + 2/\xi}{\left[\alpha\rho_{\mathrm{Pu}}(\epsilon/\rho_{\mathrm{Pu}})\right]^2} \tag{5.3}$$

and can calculate transmission measurement parameters. For example, for $\epsilon/\rho_{\mathrm{Pu}} = 1\%$ and ρ_{Pu} =0.72 g/cm^2, a total of 8.2×10^7 NRF counts are required for a 100 eV wide source. This increases 1.6×10^8 NRF counts for sources wider than the detector resolution. In order for HPGe detectors to count scattered beam photons at a rate of 2×10^4/s, the photon source would need to provide 10^{11} photons/s on target, corresponding to beam intensities ranging from 4×10^8 to 2×10^6 /eV/s for 100 eV to 20 keV wide sources. These and many more parameters are summarized in Table 5.10 for Geometry 'A', and Table 5.11 for Geometry 'B'

The values shown in Tables 5.10 and 5.11 assume that the photon source intensity has the brightness stated in the last column. For larger peak brightness photon sources, thin filters could be used to reduce overall count rates without significantly reducing NRF count rates. For photon sources with lower brightness than those stated, the detection time fractionally increases. The detection times shown also assume a 1% precision measurement of ^{239}Pu, less precise measurements reduce the counting time by the square of the fractional decrease.

Tables 5.10 and 5.11 illustrate the difficulty of performing a precise transmission measurement on ^{239}Pu. The primary problems are that ^{239}Pu resonances are weak and the sources required are extremely intense. The LLNL-proposed QM source brightness of 10^6 photons/s/eV with a width of a few keV would enable 1% measurments over 10^4 detector·days.

If ^{240}Pu has an 80 eV·b resonance, which is possible as discussed earlier, the measurement time for this isotope would be a factor of 25 - 50 less than for ^{239}Pu. For example, using a LLNL-proposed type beam would allow a 3% ^{240}Pu measurement in one day with a 30 HPGe detector array.

Table 5.11 Transmission measurement parameters necessary to perform 1% measurment of ^{239}Pu in spent fuel assembly in Geometry 'B', where $\rho_{\text{Pu}} = 0.40\text{g/cm}^2$, assuming HPGe detectors operate at 2×10^4Hz.

σ_S (keV)	$\Phi^{\sigma_S}_{\text{NRF}}$ (1/cm^2/ph)	$\Phi^{\sigma_S}_{\text{T}}$ (1/cm^2/ph)	ξ	NRF counts	t_{meas} (det·day)	intensity (1/eV/s)
0.1	1.34×10^{-10}	1.22×10^{-8}	24.8	2.64×10^{8}	69	1.09×10^{8}
0.3	4.47×10^{-11}	1.21×10^{-8}	8.28	3.03×10^{8}	237	3.68×10^{7}
1	1.34×10^{-11}	1.20×10^{-8}	2.87	4.15×10^{8}	1.08×10^{3}	1.11×10^{7}
2	6.70×10^{-12}	1.20×10^{-8}	2.27	4.59×10^{8}	2.38×10^{3}	5.54×10^{6}
3	4.47×10^{-12}	1.20×10^{-8}	2.16	4.70×10^{8}	3.65×10^{3}	3.69×10^{6}
5	2.68×10^{-12}	1.20×10^{-8}	2.11	4.76×10^{8}	6.17×10^{3}	2.22×10^{6}
10	1.34×10^{-12}	1.20×10^{-8}	2.08	4.79×10^{8}	1.24×10^{4}	1.11×10^{6}
20	6.70×10^{-13}	1.20×10^{-8}	2.08	4.79×10^{8}	2.48×10^{4}	5.54×10^{5}

Table 5.12 Comparing transmission measurement times for ^{229}Pu with detector arrays comprised of LaBr$_3$ and HPGe detectors for different source widths, σ_S.

σ_S (keV)	Detection Geometry	HPGe t_{meas} (det·day)	LaBr$_3$ t_{meas} (det·day)	improvement
0.1	A	25	1.7	15
1.0	A	4.1×10^{2}	29	14.1
10	A	4.7×10^{3}	1.5×10^{2}	3.1
100	A	4.7×10^{4}	7.4×10^{3}	1.6
0.1	B	69	4.6	15
1.0	B	1.1×10^{3}	76	14.1
10	B	1.2×10^{4}	3.8×10^{3}	3.3
100	B	1.2×10^{5}	7.7×10^{4}	1.6

High-resolution Scintillator Detectors

Detectors capable of operating at higher count rates generally have worse energy resolution. However, when the width of the photon source is narrower than the energy resolution of the detector, detector resolution is not important. Given that LaBr$_3$ detectors can operate at approximately 15 times the rate of HPGe detectors, increased photon beam intensities (relative to those indicated in Tables 5.10 and 5.11) can produce lower counting times. For beams with a narrow energy spread, the counting time reduction is directly proportional to the the beam intensity increase, whereas the improvement decreases with wider energy spread. Table 5.12 summarizes the times that a 1% measurement would take using a LaBr$_3$ detector array versus a HPGe array. The LaBr$_3$ detection times assume that the photon source is 15 times as intense as that stated in the previous tables for the HPGe detector array.

Regardless of the detection geometry, faster detectors produce significant improvement for very intense, narrow-band photon sources. Likewise, if photon beam intensities are not above those stated in Tables 5.10 and 5.11, faster detectors are not advantageous. However, if a photon beam could be made to produce 6×10^9 photons/eV/s on target, an array of one hundred 100% relative efficiency LaBr$_3$ detectors could perform a 1% measurement of ^{239}Pu in spent fuel in about 25

Table 5.13 Parameters for measuring ^{239}Pu in spent fuel assembly to 1% precision using QM photons with a beam brightness of 10^{11}/eV/s and a threshold detector of comparable volume to a 100% relative efficiency HPGe detector.

σ_S (keV)	ξ	NRF counts	t_{meas} (det·hr)	$\dot{C}$ (1/s)
0.1	22.4	8.2×10^7	4.8	4.9×10^3
0.5	4.48	1.1×10^8	6.4	5.8×10^3
1	2.24	2.4×10^8	8.4	6.8×10^3
2.5	0.896	2.4×10^8	14	1.0×10^4
10	0.22	7.5×10^8	44	2.6×10^4
50	0.045	3.4×10^9	202	1.1×10^5
100	0.024	6.8×10^9	400	2.2×10^5

minutes (1.7 detector·days/100 detectors). Such an array would correspond to subtending 7% of the backwards solid angle (or 0.43 steradians).

Threshold Detectors

Detectors that are only sensitive to photons above an energy threshold are useful for a transmission measurement if the intensity of source photons can be increased by a factor of over 100, compared to those that are presently proposed and a factor of 10^5 over those under construction. This is because the processes of transmission through an assembly and subsequent backscatter in the TD sufficiently reduces the intensity of beam photons that reach energy-resolving detectors such that the detectors are not count rate limited.

Using Table 5.9, we observe that approximately 1/2 of the photon flux due to resonant energy, monoenergetic photons is due to NRF. As shown in Figure 5.8, above 2 MeV, the majority of the beam-induced backscattered flux is due to NRF and elastic scatter of beam photons. We may therefore consider the intensity of NRF γ rays, relative to elastic scatter photons as an estimate of the value of ξ that threshold detectors would experience. These values are shown in Table 5.13, as are the number of NRF counts that would be necessary to obtain 1% statistics. This number would increase, relative to those for HPGe detectors, however, given that threshold detectors could perform in current mode, extremely bright beams could be used. Also indicated in Table 5.13 are the times (in detector·hours) and resulting count rates, $\dot{C}$, due to elastic scatter and NRF of source photons that would be detected assuming 10% of incident photons induce the threshold response, and that the beam brightness incident upon the fuel assembly is 10^{11}/eV/s.

Extremely intense QM photon sources, coupled with one or more threshold type detectors could provide 1% precision measurement of ^{239}Pu in very short times. The use of narrower band sources is more important when using a threshold detector because of the inability to determine detected photon energies.

5.2 Measurement of ^{235}U Enrichment in UF$_6$ Cylinders

NRF-based methods that directly measure the areal density of a specific isotope in a target can potentially be applied to the determination of ^{235}U enrichment in UF$_6$ cylinders. The challenges

Table 5.14 Specifications of UF_6 cylinder filling and geometry from Reference[68].

model	nom. diam. (in)	cyl. mat.	min. vol. (L)	max. U enrich. (wt. %)	max. UF_6 wt. (kg)	vol. of sol. UF_6 (L)	fill fr., f
1S	1.5	Nickel	0.15	100	0.45	0.0882	0.59
2S	3.5	Nickel	0.74	100	2.22	0.4353	0.59
5A	5	Monel	8.04	100	24.95	4.892	0.61
8A	8	Monel	37.35	12.5	115.67	22.68	0.61
12B	12	Monel	67.4	5	208.7	40.92	0.61
30B	30	Steel	736	5	2277	446.5	0.61
48X	48	Steel	3084	4.5	9539	1870	0.61
48Y	48	Steel	4041	4.5	12501	2451	0.61
48HX	48	Steel	3964	1	12261	2404	0.61

Figure 5.10 Filling profiles for UF_6 cylinders. x represents the fraction of the UF_6 that adheres to the walls before gravitational filling causes the remainder to fill the bottom of the cylinder.

in this application are different from that of SNF assay in that the concentration of the isotope to be measured is generally much higher and the radioactivity much lower. The applicability of both, backscatter and transmission methods, is analyzed.

UF_6 is created as a stable uranium gas in enrichment processes and stored in metal cylinders. The phase diagram of UF_6 has a triple point is at 0.15 MPa and 64.02 °C. At and below this temperature, the liquid phase of UF_6 is unstable, therefore in most conditions, UF_6 cylinders will contain primarily solid UF_6 and nearly void, vapor filled space. UF_6 cylinders are filled by allowing warm, low-pressure UF_6 gas to cool and condense within evacuated cylinders. The size of the cylinder dictates the allowable maximum U enrichment as listed in Table 5.14. The temperature of UF_6 gas and cylinder during cylinder filling can strongly influence the profile of UF_6 within the cylinder. Cold cylinders increase the likelihood that the entirety of the UF_6 gas will uniformly desublimate onto the exterior of the cylinder, producing a UF_6 annulus[69]. Conversely, warm cylinders allow gravity to pull the condensing UF_6 toward the bottom of the cylinder. A representative series of filling profiles are shown in Figure 5.10.

First, the resonant, and non-resonant attenuation of photons penetrating through various UF_6 cylinder types were considered. The attenuation coefficient for 1734 keV photons, corresponding to the energy of the largest known ^{235}U resonance, is 0.04889 cm^2/g, or 0.249 cm^{-1} for normal density solid UF_6. The expected intensities of 1734 keV photons after transmission through varying thickness of UF_6 are shown in Figure 5.11, with the maximum possible areal densities for cylinders indicated. This figure indicates that a transmission measurement may be made on thinner cylinders, but that the non-resonant attenuation limits the thickness through which a transmission measurement can be made and thus limits the applicability for the thicker cylinders.

The excess attenuation for resonant-energy photons for a transmission measurement through

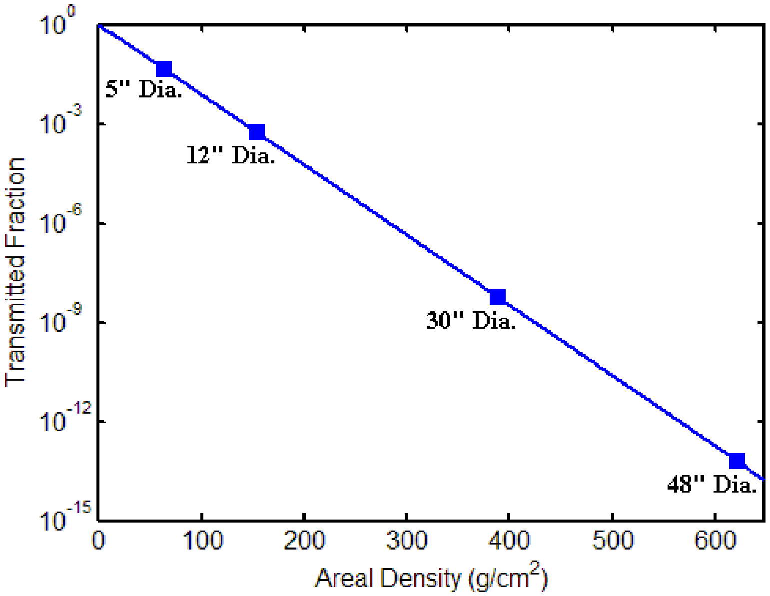

Figure 5.11 Non-resonant attenuation of 1734 keV photons incident upon varying thicknesses of solid UF_6. The points indicate the maximum UF_6 areal density for various cylinder types.

the center of cylinder is shown in Figure 5.12 as a function of U enrichment. Also indicated are the maximum allowed U enrichments for each cylinder type. The figure indicates that the excess attenuation of resonant-energy photons, as observed by a transmission-type measurement, would be significant for all of the cylinder types considered. The ^{235}U areal density can be determined from the measured attenuation of photons due to NRF in the same way as the Pu content in spent fuel.

5.2.1 Transmission Measurement Example

Employing the techniques and modeling tools developed for the study of spent fuel assay, a transmission measurement of a 12” cylinder was investigated as a sample case. The irradiation of the cylinder with a bremsstrahlung beam with an endpoint energy of 2 MeV was simulated in MCNPX. The photon beam was emitted from a converter located 25 cm from the cylinder center and collimated to 5° as schematically shown in Figure 5.13. The ^{235}U transmission detection sheet was positioned 100 cm downstream of the cylinder. The flux of photons from resonant, elastic, and inelastic interactions in the transmission detection sheet was tallied at a distance of 50 cm from the sheet at a scattering angle of 135°. The calculated energy-dependent flux distribution was subsequently filtered by the shielded detector response model to determine total and NRF photon count rates. The detector response was calculated for a 100% relative efficiency HPGe detector for various filter thicknesses, unshielded, 1/2” of Pb, and 1” of Pb. The resulting rates normalized to the bremsstrahlung-inducing electron beam current are summarized in Table 5.15.

The maximum beam intensities that could be used for such a measurement are limited by the detector count rate capability and thus dependent on the total integrated photon count rates listed in the bottom row of Table 5.15. Using a 1/2” Pb filter, a 1 Ampere electron beam incident upon the bremsstrahlung converter would induce 8.6×10^4 counts per second, which is too high for HPGe detectors. Using the conservatively assumed maximum HPGe detector rate of 2×10^4 counts

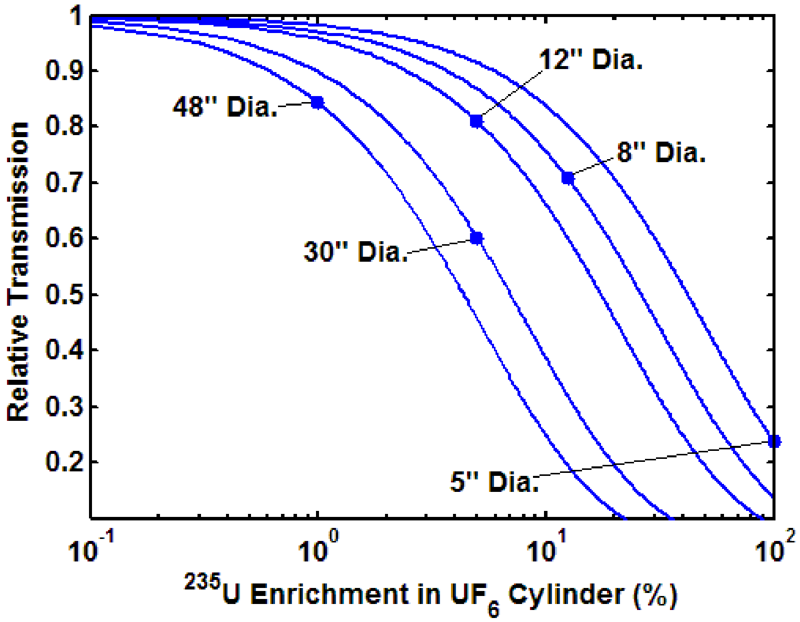

Figure 5.12 Resonant attenuation of 1734 keV photons incident upon the maximum thicknesses of solid UF$_6$ for various ^{235}U enrichments. The points indicate the maximum allowed UF$_6$ enrichments for various cylinder types.

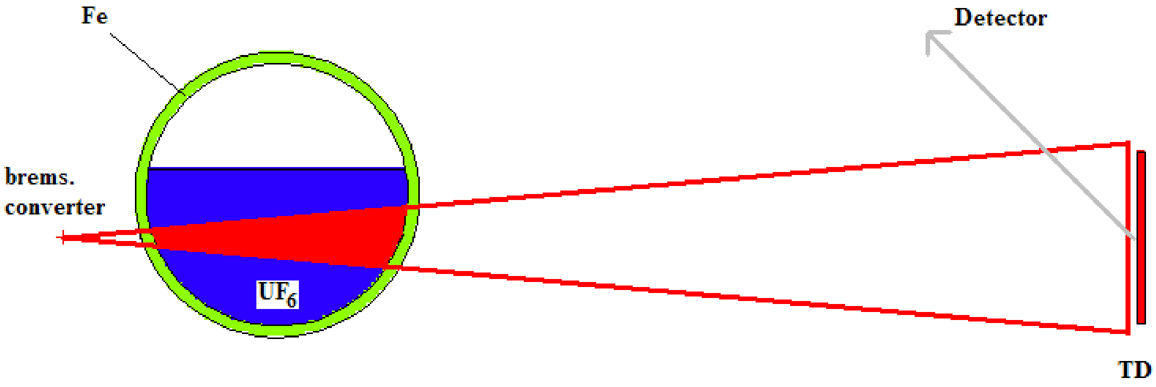

Figure 5.13 Schematic geometry for transmission measurement of 12" UF$_6$ cylinder.

Table 5.15 Simulated photon fluxes and count rates in a shielded HPGe detector for a transmission measurement of a 12” UF_6 cylinder.

Pb filter thickness		0	1/2”	1”
energy (MeV)	flux ($1/cm^2/C$)	counts (1/C)	counts (1/C)	counts (1/C)
1.656	4.51×10^{-1}	5.63	2.86	1.42
1.733	1.21	1.51×10^{1}	7.57	3.81
1.769	4.74×10^{-3}	5.92×10^{-2}	2.94×10^{-2}	1.48×10^{-2}
1.815	1.31×10^{-1}	1.64	7.99×10^{-1}	4.09×10^{-1}
1.828	4.48×10^{-1}	5.60	2.73	1.40
1.862	6.62×10^{-1}	8.28	4.01	2.05
total	1.65×10^{5}	8.25×10^{6}	8.58×10^{4}	1.83×10^{4}

Table 5.16 Beam currents and measurement times for enrichment (5%) measurements with 5% precision.

detector type	filter thickness	e^- beam int. (mA)	measurement duration (det·hr)
HPGe	0	2.4	152
$LaBr_3$	0	36	74
HPGe	1/2”	233	3.3
$LaBr_3$	1/2”	3500	1.5

per second, one estimates that a 230 mA beam would be acceptable from a detector perspective, likewise a 2.5 mA and 1.1 A beam would produce 2×10^4 counts per second in HPGe detectors behind no filter and a 1” filter, respectively. Bremsstrahlung beams created by 1 ampere electron beams are not readily available, and their production presents considerable technical challenges. We therefore assume that for this irradiation type, filters thinner than 1” are most practical.

We can estimate the necessary number of NRF counts required to make a measurement of a given precision based on the relationship between the uncertainty due to counting statistics and the uncertainty in the amount of ^{235}U in a cylinder. This number depends on the detector resolution and the strengths of the resonances and totals approximately 50,000 NRF counts for a 5% measurement using HPGe detectors, or 400,000 counts if lower-resolution $LaBr_3$ detectors are used. Electron beam currents and filter thicknesses for operation at the maximum detector count rate are listed in Table 5.16 together with the estimated duration of a 5%precision measurement. The measurement times indicate that an arrangment using a dozen HPGe detectors shielded by 1/2” of Pb could acheive a 5% statistical uncertainty measurement of the enrichment in a 12” UF_6 cylinder in 16 minutes.

5.2.2 Backscatter Measurement Simulation

Two backscatter measurement scenarios were investigated. One was that of a 5” diameter UF_6 cylinder filled with 100% enriched UF_6, and the other one was that of a 48” diameter cylinder filled with 1% enriched UF_6. The simulated measurement geometry for the 5” cylinder is shown in Figure 5.14.

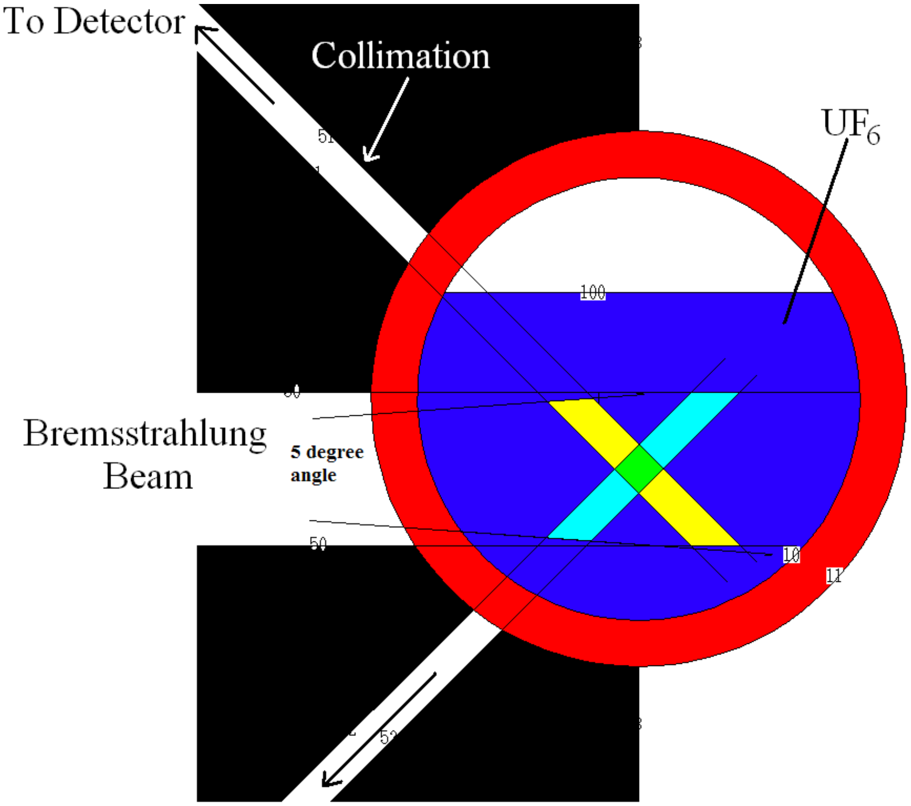

Figure 5.14 Schematic geometry for backscatter measurement of 5” UF_6 cylinder. The intersection of the collimator hole views and the beam are indicated.

The backwards hemisphere is filled with shielding that only allows photons through three bore holes. Each collimator hole is centered on a point 2 cm below the midline of the cylinder at the horizontal center of the cylinder. The photon beam reaches the UF_6 cylinder through a 4.4 cm diameter bore hole. The photon detectors positioned at ±45° behind 1 cm diameter collimator holes at a distance of 50 cm from the cylinder.

The photon beam was simulated as a bremsstrahlung spectrum with a 2 MeV endpoint energy and a 5° opening angle. The simulation results indicate that a measurement of the ^{235}U content in a 5” cylinder with 2% statistical uncertainty could be performed with one HPGe detector in one hour. Using multiple detectors could proportionally reduce the time necessary to make such measurements, indicating that very precise measurement of the ^{235}U fraction in small, highly-enriched cylinders could be acheived using intense bremsstrahlung sources and dedicated geometries in less than 15 minutes.

The simulated geometry for the measurement of the 48” diameter cylinder is shown in Figure 5.15. An ideal collimator with a 3.2 cm diameter opening for the bremsstrahlung beam and 6 bore holes for the detection of the scattered photons covers the backward hemisphere. Each collimator hole is centered on a point 10 cm below the vertical center of the cylinder. The 1 cm diameter collimator holes are at ±45° relative to the beam, with pairs centered 48, 50 and 52 cm upstream of the horizontal center of the cylinder as seen in Figure 5.15.

The photon source in this simulation was positioned 80 cm from the center of the cylinder, emitting bremsstrahlung photons with an endpoint energy of 2 MeV into the forward 5°. The

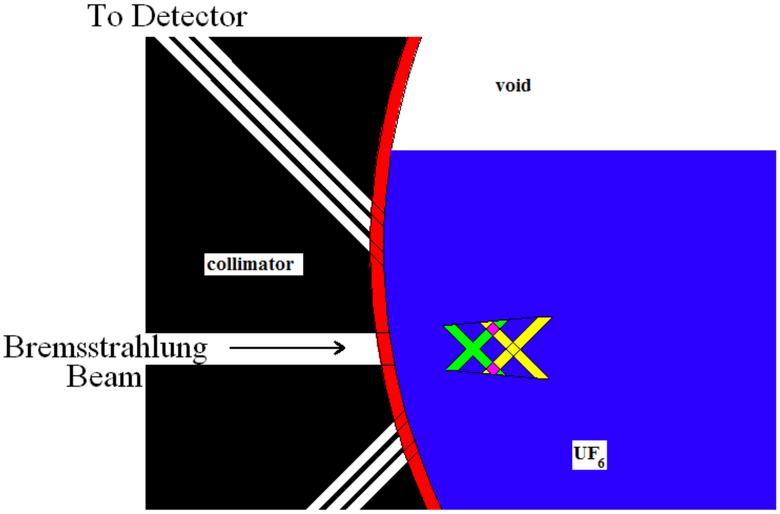

Figure 5.15 Schematic geometry for backscatter measurement of 48” UF_6 cylinder. The intersection of the four of the six collimator hole views and the beam are indicated.

photon fluences were tallied at a distance of 200 cm from the intersection of the collimator hole cylinder and the beam center. A schematic of this geometry is shown in Figure 5.15.

The precise measurement of the uranium enrichment at the 1% level in a very large, 48” diameter cylinder is considerably harder and more time consuming than the measurement of the enrichment in a small cylinder as discussed above. Due to the low enrichment the signal-to-background ratio is reduced by a factor of about 100. This increases the statistical uncertainty with which the NRF peaks are measured by a factor of about 5 - 10 compared to pure $^{235}UF_6$. The count rates are very depth dependent. For example, increasing the depth of the volume viewed by the gamma detectors from 9 to 13 cm decreases the photon flux seen by the detectors by about a factor of 20. In addition, larger distances between source target and detector result in further reduction in NRF (and total) count rates. In the described geometry with a half-inch thick Pb filter in front of the detector a very intense bremsstrahlung beam, generated by up to 1.6 A electron beams, could be used without saturating a 100% relative efficiency HPGe detector. Assuming such beam were used (and neglecting the practical difficulties of producing it) a measurement with 5% statistical uncertainty could be made in 20 detector hours. While such a measurement does not appear to be very practical, it could be improved and optimized by locating the detectors nearer to the UF_6 cylinder and by interrogating the UF_6 at a shallower depth. Still, it appears possible to use bremsstrahlung induced NRF to measure the ^{235}U content in UF_6 cylinders with 1% enrichment. Using HPGe detector arrays one could potentially make precise measurements in less than one hour.

5.3 Pu Measurements in MOX Fuels

Another potential application of NRF-based methods is the NDA of fresh fuel, i.e., the measurement of Pu and other actinides in fuel produced in a reprocessing facility or of the Pu content in mixed oxide or MOX fuel. Here we present the results of a series of simulations, similar to those performed for the study of SNF assay, as described in Section 5.1, in which a MOX fuel pin was

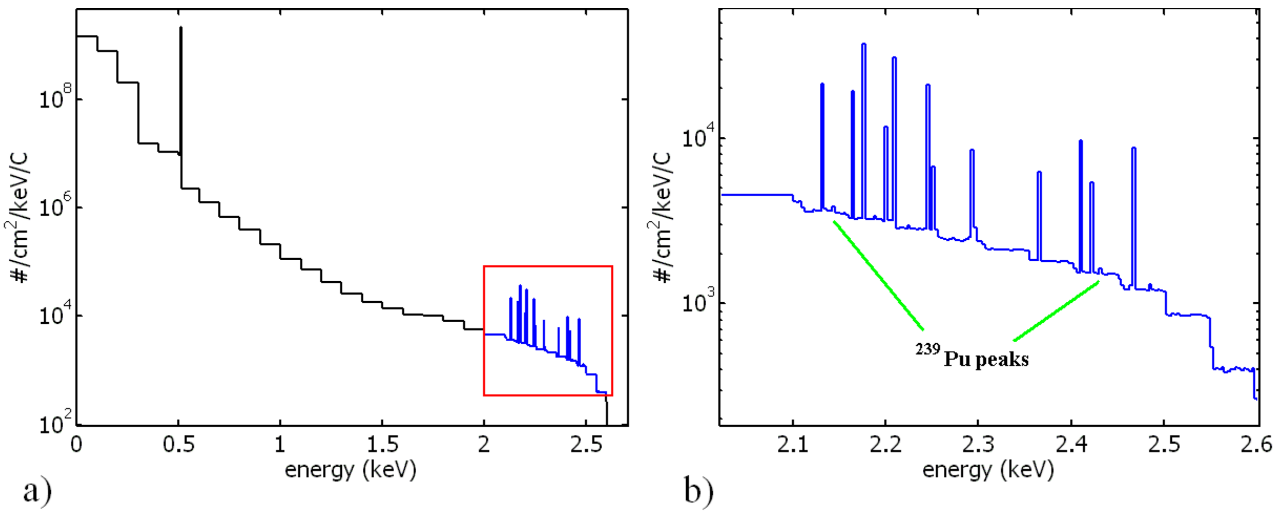

Figure 5.16 a), calculated backscattered photon flux for assay of a 5 mm diameter MOX cylinder at a position 60 cm from the target, at 135° relative to initial electron beam direction. The flux is normalized per Coulomb of 2.6 MeV electrons incident upon the bremsstrahlung converter.

Figure 5.16 b), same as Figure 5.16 a), except with NRF energy region expanded. Most NRF peaks are due to NRF of ^{238}U. Two (smaller) ^{239}Pu NRF peaks are indicated.

irradiated with 2.6 MeV endpoint-energy bremsstrahlung beam. The composition of the fuel pin was assumed to be MO_2, where 95% of the M atoms were ^{238}U, 2.5% were ^{239}Pu, and 2.5% were other Pu isotopes whose NRF responses are unknown, and were not considered in this simulation. However, ^{240}Pu and ^{242}Pu could have significantly larger cross sections than ^{239}Pu and thus are of interest. The measurement geometry was similar to the one shown in Figure 2.3 a) with the bremsstrahlung converter located 60 cm from the center of the fuel pin. The detector was also positioned 60 cm from the fuel pin center, at an angle of 135° relative to the beam trajectory. The calculated photon spectrum backscattered from the MOX fuel pin that would be incident upon a shielded detector is shown in Figures 5.16 a) and 5.16 b). The spectrum shows numerous NRF lines; however, the majority of these lines are due to NRF of ^{238}U. In the expanded spectrum in Figure 5.16 b), the two largest NRF peaks due to ^{239}Pu NRF are visible and indicated.

The spectrum in Figure 5.16 a) was input into detector response models to determine the total and NRF count rates per electron incident upon the bremsstrahlung converter for different filter thicknesses. Assuming that a detector operates at 20 kHz, the total count rates are converted into beam intensities, which are then used to scale the NRF count rates. Table 5.17 presents bremsstrahlung-inducing beam currents, NRF count rates for two resonances, and times (in detector·hours) necessary to obtain 5% and 1% (25 times longer than 5% measurement as dictated by counting statistics) statistical uncertainties.

For systems using bremsstrahlung sources to measure ^{239}Pu in MOX, intense beams and multiple detectors placed behind thick Pb filters could achieve 5% statistical uncertainties using NRF in 3 hours if twenty four 100% relative efficiency HPGe detector were used and the MOX fuel pin were irradiated with a 250mA bremsstrahlung beam.

Future intense quasi-monoenergetic photon sources could potentially lead to much shorter measurement times. Due to the lower non-resonant photon flux, detection count rate limitations are encountered at accordingly higher NRF rates, as discussed for SNF measurements, or completely

Table 5.17 Bremsstrahlung-inducing beam intensities, I, NRF count rates for two ^{239}Pu resonances, R_{NRF}, and detection times, t, necessary to obtain 1% and 5% statistical uncertainty in ^{239}Pu content in MOX fuel using 2.6 MeV endpoint-energy bremsstrahlung.

		R_{NRF} (1/s)		t (det·hr)	
x_f (cm)	I (μA)	2143 keV	2431 keV	5%	1%
0	2.46	1.28×10^{-5}	5.02×10^{-6}	1.80×10^{5}	4.50×10^{6}
1.27	208	5.83×10^{-4}	2.32×10^{-4}	3.98×10^{3}	9.95×10^{4}
2.54	1.0×10^{3}	1.49×10^{-3}	6.04×10^{-4}	1.55×10^{3}	3.87×10^{4}
5	1.85×10^{4}	8.02×10^{-3}	3.35×10^{-3}	2.84×10^{2}	7.10×10^{3}
7.5	2.48×10^{5}	3.05×10^{-2}	1.32×10^{-2}	7.34×10^{1}	1.84×10^{3}

overcome if a suitable threshold detector can be developed. In conclusion, NRF-based methods could provide unique NDA measurement capabilities, but new powerful photon sources and gamma detectors would be needed.

6 Conclusions

The feasibility of applying NRF-based methods to nuclear safeguards has been investigated using analytical modeling and radiation transport simulations. We have employed the radiation transport code MCNPX for the modeling of the scattered, non-resonant background, the notch refilling in transmission measurements, and the full simulation of NRF measurements.

In our early studies we had found that MCNPX underestimated the non-resonant elastic scattering at backwards angles by orders of magnitude, mainly due to a flawed treatment of Rayleigh scattering in the code. The correction of this shortcoming by upgrading the form factors resulted in much better agreement with some experimental data, although the photonuclear processes, nuclear Thomson, Delbr uck, and giant dipole scatter, which are important contributors to the elastic scattering background at higher energies, were not taken into account. Our analysis showed that for the elastic scattering of photons with energies around 2 MeV on uranium, the use of the upgraded form factors in MCNPX overestimates the Rayleigh scattering and leads to a chance agreement with experimental data. For higher photon energies and for low Z targets the disagreements can be large due to the missing photonuclear scattering. It would be desirable to at least include nuclear Thomson scattering in MCNPX simulations for NRF studies. Calculations based on ENDF form factors, as currently implemented in MCNPX could underestimate the elastic scattering cross section by as much as a factor of ten for a uranium target at higher photon energies. Even larger discrepancies, up to several orders of magnitude, are possible for lighter elements such as zirconium.

We completed the analysis of our transmission experiment that measured ^{238}U areal densities ranging between 1.7 and 8.5 g/cm^2 in an approximately 86 g/cm^2 thick Pb target by observation of the attenuation of resonant-energy photons. The data obtained in this experiment, using targets of comparable thickness to an SNF assembly and a bremsstrahlung beam, have exhibited a trend indicative of notch refill that could increase the measured NRF rate by up to 5% for large resonances and the target containing the most ^{238}U. A correction based on MCNPX modeling has been implemented in the analysis producing the areal densities measured by transmission NRF. To within statistical uncertainties, the measurement agrees with the modeling used to describe resonant attenuation and subsequent measurement of NRF photons emitted from the transmission detector. The experiment demonstrated that a ^{238}U content of 1% could be measured. However, the precision was count rate limited indicating the challenge for using transmission nuclear resonance fluorescence to precisely measure small quantities of an isotope in an assay target.

Utilizing the developed modeling capabilities, we studied and evaluated NRF-based methods for three safeguards applications: the isotopic assay of spent nuclear fuel (SNF), the measurement of ^{235}U enrichment in UF$_6$ cylinders, and the determination of ^{239}Pu in mixed oxide (MOX) fuel. Particularly challenging is the determination of Pu content in SNF. Backscattering measurements face three main difficulties that severely limit this approach: a small signal-to-background ratio for the low Pu concentrations in SNF, a large background from the radioactivity of the SNF, and a strong dependence of the intensity of the NRF signal on depth. The transmission method provides two important advantages: the detectors can be shielded from γ-rays emitted from the fission products in the SNF, and the measurement sensitivity is independent of depth. Given the low concentrations of the Pu isotopes in SNF and the small integrated nuclear resonance cross sections, the main challenge in achieving the goal of a few percent measurement uncertainties lies in accruing of sufficient counting statistics in an acceptable measurement time.

Using bremsstrahlung sources, transmission measurements are possible but sufficiently precise measurements of Pu isotopes in SNF would require 10's to 100's of hours, a very intense bremsstrahlung source, and a very large array of fast detectors with high energy resolution. Quasi-monoenergetic photon sources such as Laser Compton scattering sources could potentially lead to greatly improved performance. Due to the narrow energy spread, the flux of lower-energy photons scattered into the detectors is dramatically reduced, compared to bremsstrahlung sources thus lessening detector count rate limitations. For example, assuming a photon source with a 1 keV energy spread, an intensity of 6×10^8 ph/eV/s, and operating continuously or at MHz pulse rates, the measurement time would be on the order of hours using a large detectors array. Shorter measurement times would require sources with narrower energy spreads and higher intensities. However, LCS sources of the type under development at LLNL are pulsed at kHz or lower rates and threshold detectors, such as Cherenkov detectors, that can integrate the signal instead of detecting single photons are needed. Interestingly, such threshold detectors could also make backscatter measurements with a high-intensity, pulsed photon source possible. Because the detectors could be gated and made insensitive in between short, sub-nanosecond pulses, the background from the radioactivity of the SNF seen by the detectors would be reduced by many orders of magnitude. In a best-case scenario, a measurement with 1% statistical uncertainty could be accomplished with a 10^8 ph/eV/s photon source and an ideal threshold detector array in 10 min. While this indicates promise, neither photon source nor detector technology presently exists.

For the measurement of ^{235}U enrichment in UF_6 cylinders, the transmission method can be applied to the cylinders up to 12" in diameter. Using an intense bremsstrahlung beam and a dozen HPGe detectors, a 5% precision measurement of 5% enrichment could be performed in less than half an hour. For larger cylinders, through which the photon beam cannot be transmitted, the enrichment can be determined to a depth of roughly 10 cm in backscattering measurements. Our results indicate that 1% enrichment could likely be measured with a 5% statistical uncertainty in less than one hour. Another potential application of the NRF technique is the determination of Pu and other actinides in fresh fuel. As an example we considered the measurement of 2.5% ^{239}Pu in a MOX fuel pin. Using an intense bremsstrahlung beam and an array of 24 HPGe detectors in a backscatter arrangement the ^{239}Pu content could be measured with 5% statistical uncertainties in roughly 3 hours. As in the case of SNF assay, much shorter measurement times could potentially be achieved with future intense quasi-monoenergetic photon sources.

The concepts for applying NRF to quantitative measurements in safeguards have been established and the framework and tools for designing and analyzing specific methods have been developed. Further research is essential to fully assess the technique and to develop future measurement systems.

Future Work

A high priority for assessing NRF measurements of Pu in SNF is to determine if ^{240}Pu has sufficiently strong NRF resonances so that this isotope could be measured using available photon sources and detectors. As an even mass number isotope, ^{240}Pu likely has significantly larger resonances than ^{239}Pu, which could result in measurement sensitivities that are more than ten times higher. Determination of ^{240}Pu content may be useful to constrain other SNF measurements. Also, since ^{240}Pu content increases with total burn-up, measuring a lower than expected ^{240}Pu concentration in SNF could indicate weapons-grade Pu breeding. Similar efforts to improve nuclear data for other isotopes that may prove important for safeguarding future nuclear fuel cycles are also of interest. The list of important actinides includes other long-lived Pu isotopes, Th isotopes, ^{233}U, and possibly other transuranics. For any isotope, the accuracy to which an NRF-based measurement may be made will be limited by the accuracy and precision to which the resonance strength is known. Therefore, more precise measurements of resonance cross sections should be pursued for all isotopes.

Along with nuclear data improvements, the ability to model NRF measurements should be further strengthened. The non-resonant elastic scatter of photons is treated very approximately by ENDF, and as a result, it is not well modeled by most Monte Carlo radiation transport codes (MCNPX included). Spent fuel measurements with the required sensitivity and accuracy most likely require quasi-monoenergetic photon sources with intensities that are at least two orders of magnitude higher than those currently being designed or proposed. Thus, the development of narrow-band, very intense LCS photon sources is of utmost interest, as is the development of very fast, high-resolution γ-ray detectors and efficient threshold detectors. Future applications of NRF methods may be in large, fixed installation such as a reprocessing plant and in advanced fuel cycles where increased concentrations of minor transuranics may present increased difficulties for other NDA techniques.

Appendix

A Rayleigh Scattering in MCNP

A.1 Introduction

Documentation of the MCNP series of codes has claimed for years to accurately represent the data present in evaluated nuclear data files [25],[4],[40],[41]. The photo-atomic data in the ENDF/B-VI format are based on the evaluated photon data library (EPDL97)[42]. However, the work supporting this report observed that the sections of code describing the form factor evaluation of coherent and incoherent scattering had not been updated since their precursor code, MCP, was written in 1973[43]. This legacy code results in significant inaccuracies in photon spectra computed by MCNPX when simulating geometries that are typical of NRF experiments[44].

MCNP treats all coherent scattering as Rayleigh scattering of unpolarized photons and follows the form factor approximation for the Rayleigh cross section:

$$\sigma_{Ray}(\theta) = \sigma_{Th}(\theta)\,[F(q,Z)]^2 \tag{A.1}$$

where $F(q,Z)$ is a tabulated form factor value, and $\sigma_{Th}(\theta)$ is the Thomson scatter cross section, given by $\sigma_{Th}(\theta) = \frac{r_e^2}{2}(1+\cos^2\theta)$. Here, r_e^2 is the classical electron radius, 2.818 fm, and θ is the angle between the scattered and incident photon.

Data libraries used in MCNP are created by the code NJOY, which reads ENDF tabulations of atomic form factors and converts them into the ACE format used in MCNP[26]. Atomic form factor values are tabulated for a given Z and momentum transfer between the scattered photon and the atomic electron, q. The units of q should be units of momentum, however q has traditionally been tabulated in *reduced wave number*, which has units of inverse length[1].

The derivation and use of momentum transfer values in MCNP has been poorly documented. MCP and MCNP user manuals describes q in units of cm^{-1},[41],[43] however the data tabulated in MCNPX are in units of $\AA^{-1}$[45].

The legacy problems in elastic scatter come from the fact that MCNP has historically had a fixed array of q-values for which coherent scattering form factors, $C(Z,q)$ are defined. Despite the fact that the EPDL97 (and ENDF) now tabulates form factors for q up to $10^{11}\AA^{-1}$, q in MCNP was restricted to $q \leq 6\ \AA^{-1}$ and coherent scattering form factors for $q > 6$ were assumed to be 0. Table A.1 demonstrates the maximum coherent scattering angles, $\theta_{\max}$, that were allowed by this restriction. Figure A.1 helps to explain why this short-coming had gone un-noticed by many MCNP users[2]. In it, the fraction of the Rayleigh scattering cross section that is due to scattering

---

[1] The conversion between momentum transfer, $\hbar k\sin(\theta/2)$, and reduced wave number is accomplished by dividing by Plank's constant, h, inserting $\frac{c}{c}\frac{m_ec^2}{m_ec^2}$, equating, $E = \hbar ck$ and, $\sin(\theta/2) = \sqrt{\frac{1-\cos\theta}{2}}$. Evaluating the constants:

$$q = \frac{c}{hc}\frac{m_ec^2}{m_ec^2}2\hbar k\sin(\theta/2) = \frac{E}{m_ec^2}\frac{2m_ec^2}{\sqrt{2}hc}\sqrt{1-\cos\theta} = 29.1445[\AA^{-1}]\frac{E}{m_ec^2}\sqrt{1-\cos\theta}$$

[2] This short-coming was independently observed by Lodwick and Spitz when they compared in vivo x-ray fluorescence measurements of lead in bone to MCNP calculations[46]

Table A.1 Maximum coherent scattering angles allowed in the MCNP codes.

E (keV)	Angle
74.4	180°
105	90°
194	45°
853	10°
1733	4.9°
2423	3.5°

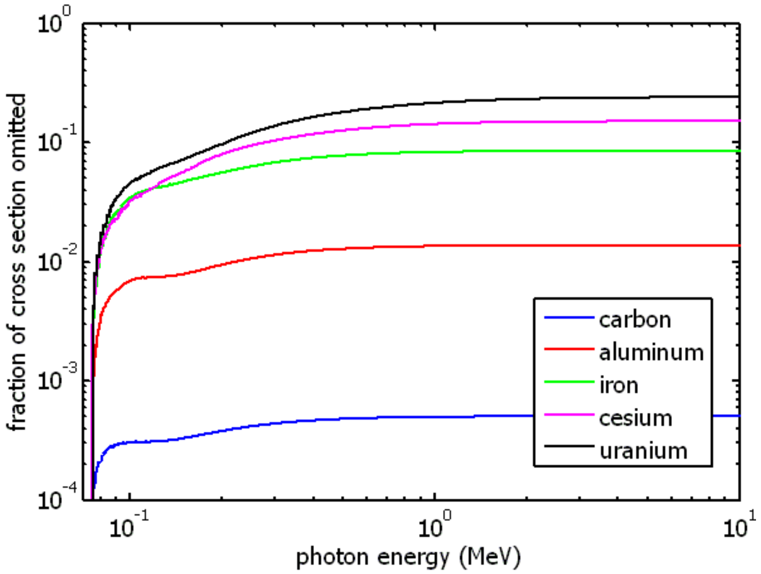

Figure A.1 Fraction of Rayleigh scattering cross section that corresponds to a reduced momentum transfer value, $q \geq 6\ \mathring{A}^{-1}$.

above $\theta_{\max}$ is plotted versus photon energy for various elements, i.e.

$$f = \frac{\int_{q=6[\mathring{A}^{-1}]}^{q_{\max}} \sigma_{Ray}(\theta) d\mathbf{\Omega}}{\int_{q=0}^{q_{\max}} \sigma_{Ray}(\theta) d\mathbf{\Omega}} \tag{A.2}$$

where $q_{max} = 29.1445[\mathring{A}^{-1}]\frac{E}{m_e c^2}\sqrt{2}$. The omission is most significant in high-Z materials, and is most important when photon energies exceed approximately 100 keV. As will be described, this omission is only important when coherently-scattered photons can be distinguished from incoherently-scattered and annihilation photons. The distinction is most obvious when backscattering of multi-MeV photons from high-Z materials is considered, and this is precisely what is done in experiments designed to measure NRF.

Modification of the MCNPX source code and the NJOY data processing code are described in Section A.4. These modifications enable MCNPX to simulate Rayleigh scattering for all problems.

To test that modifications of the MCNPX code and datafiles were successful, two pairs of simulations were conducted comparing elastic scattering rates before and after implementation of the modifications. For each pair a pencil beam of monoenergetic 1.7 MeV photons was normally impinged upon a 1 cm radius by 100 mm depth cylindrical target of either uranium or iron.

Photons emitted from the target were tallied as they crossed a spherical surface of 10 cm radius, centered at the center of the target cylinder. The direction of the emitted photons relative to the direction of the incident beam were tallied in 1° angular bins up to 10°, and then in 5° bins. The energy of the emitted photons were also tallied, with photons within 860 eV of the initial energy being considered elastically scattered. This bin width was selected to ensure that incoherently scattered photons are not tallied into the elastic bin for scattering angles greater than 1°. The effective elastic scattering cross section was then calculated by the relation

$$\frac{d\sigma_{\mathrm{ES}}}{d\boldsymbol{\Omega}} \approx \frac{N_{\mathrm{F1}}}{\Delta\Omega}\frac{M}{N_A \rho x} \tag{A.3}$$

where N_{F1} is the number of photons in the elastic tally bin, $\Delta\Omega$ is the solid angle subtended by the angular bin, M is the molar mass of the target material, N_A is Avagadro's number, and ρx is the areal density of the target.

Figures A.2 and A.3 present the simulated angle-differentiated cross sections for elastic scattering of 1.7 MeV photons before (red) and after (black) the implementation of the extended Rayleigh scattering cross section library. The EPDL97 cross section for elastic scattering is also shown in green in both figures. The cross sections resulting from simulations that include the new form factor arrays closely follow the EPDL97 values. For the red histogram, non-zero values calculated for scattering into angles above the critical angle of 5.2° are due to the relatively improbable combination of photoelectric absorption followed by bremsstrahlung emission. This process yields photons in the elastic bin, and would yield an even smaller (nominally) elastic scattering probability were the highest energy bin made narrower. Regardless, the five (uranium) and seven (iron) decade decreases in effective elastic scattering cross section between the $3^{\circ} - 4^{\circ}$ and $6^{\circ} - 7^{\circ}$ bins indicate effects of the non-physical cutoff that had been implemented in MCNP. That the effective cross section was calculated to be 30% (uranium) and 8.5% (iron) lower after implementation of the extended library for the range $1^{\circ} - 5^{\circ}$ is explained by the fact that photons probabilistically sampled to undergo coherent scattering had been constrained to the forward 5.2°, whereas now all angles are physically allowed. The amount by which MCNPX had overpredicted the Rayleigh scattering cross section is exactly the inverse of the fractions shown in Figure A.1 for 1.7 MeV photons. Thus, as another result of the truncated form factor arrays, MCNP had previously been overestimating elastic scattering of photons in forwards directions, and this effect was most severe for high photon energies and high-Z materials.

A.2 Form Factor Sampling Methodology

This section describes the method used in MCNPX to sample the coherent scatter cross section. This method defines the integrated form factors, which must also be included in the ACE files that provide the photo-atomic data for MCNP.

Suppose we want to sample a probability density function (PDF), $P(y)$, defined in the interval $a \leq y \leq b$, and related to another known PDF, $Q(y)$ by the following

$$P(y) = C_0 F(y) Q(y) \tag{A.4}$$

where C_0 is a constant, $C_0 > 1$ and $F(y)$ is a function with range $0 \leq F(y) \leq 1$.

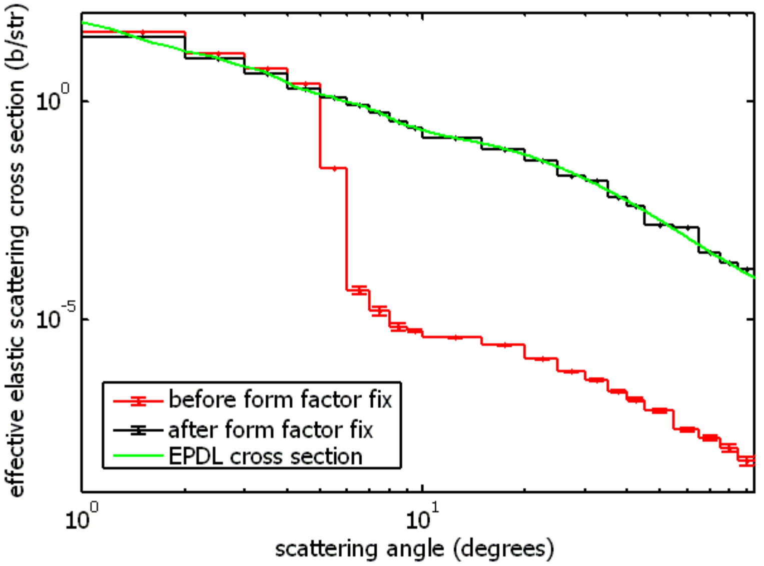

Figure A.2 MCNPX-simulated differential cross section for scattering of 1.7 MeV photons within 860 eV of initial energy from 100 μm thick uranium with EPDL Rayleigh scattering cross section overlaid.

A.2.1 Sampling a Simple PDF

First we must define what is meant by ‘sampling a PDF’. Assume the PDF, $Q(y)$, is a normalized and integratable function in some interval,

$$\int_a^b Q(y) = 1 \tag{A.5}$$

Sampling of $Q(y)$ is accomplished by using a random number, $0 \leq r \leq 1$, to select a value, y_{sample}, between a and b with a probability proportional to the value of the PDF.

The cumulative (or integrated) distribution function (CDF) for $Q(y)$ is defined as,

$$\mathbf{Q}(y') = \int_a^{y'} Q(y)dy \tag{A.6}$$

Therefore $\mathbf{Q}(a) = 0$ and $\mathbf{Q}(b) = 1$. By inverting the function $\mathbf{Q}(y')$, we have a function with a domain of [0,1]. Using the random number, r_1, we obtain

$$y_{\text{sample}} = \mathbf{Q}^{-1}(r_1) \tag{A.7}$$

which is a value of y, sampled from the PDF $Q(y)$. Clearly, this only works for PDFs than can be integrated, and whose integral can be inverted.

A.2.2 Rejection-Sampling Method

Sampling of equation A.4 is accomplished by use of the *rejection-sampling method.* First, $Q(y)$ is sampled. The value of y is accepted, with a probability of $F(y)$, by using a second random number, r_2 to check that

$$r_2 < F(y) \tag{A.8}$$

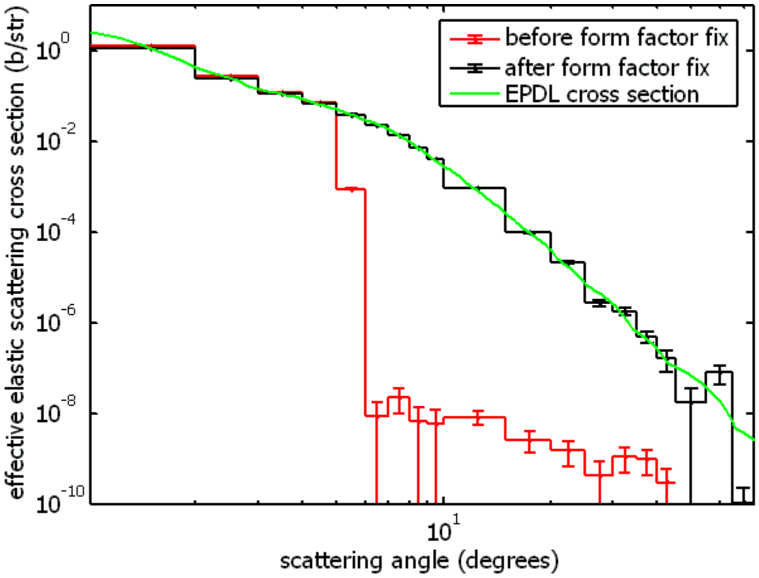

Figure A.3 MCNPX-simulated differential cross section for scattering of 1.7 MeV photons within 860 eV of initial energy from 100 : μm thick iron with EPDL Rayleigh scattering cross section overlaid The large statistical uncertainty at high angles is due to the rarity of the events.

The probability of not accepting a sampled value for y is given by

$$P_{\text{reject}} = 1 - \int_a^b F(y)Q(y)dy \tag{A.9}$$

When y is rejected, we sample another value of $Q(y)$ and again check with a new random number against equation A.8, potentially allowing an infinite number of samplings.

To prove that this will give an appropriate sampling of $P(y)$, first note that

$$1 = \int_a^b P(y)dy = \int_a^b C_0 F(y)Q(y)dy \tag{A.10}$$

so

$$\int_a^b F(y)Q(y)dy = C_0^{-1} \tag{A.11}$$

The probability of k rejections is then

$$P_k = (1 - C_0^{-1})^k \tag{A.12}$$

and the probability of accepting the $k+1$-th iteration is

$$(1 - 1/C_0)^k F(y) \tag{A.13}$$

Using

$$\sum_{k=0}^{\infty} (1 - 1/C_0)^k = C_0 \tag{A.14}$$

we see that if an infinite number of iterations is allowed, the PDF for sampling y is given by

$$C_0 F(y)Q(y) = P(y) \tag{A.15}$$

A.3 Sampling Rayleigh Scattering Cross Sections

The angle of Rayleigh scattering is sampled in MCNPX by the rejection - sampling method. In this formulation, the independent variable, y, is given by, q^2, the square of the momentum transfer of the scattering event, which for a given photon energy is

$$q = K\alpha\sqrt{1-\mu} \tag{A.16}$$

where $K = 29.1445\,\mathring{A}^{-1}$, $\alpha = E/m_e c^2$, and $\mu = \cos(\theta)$.

The Rayleigh scattering cross section is given by

$$\sigma_{Ray}(\theta) = \sigma_{Th}(\theta)\,[F(q,Z)]^2 \tag{A.17}$$

where the Thomson scattering cross section is given by

$$\sigma_{Th}(\theta) = \frac{r_e^2}{2}(1+\cos^2\theta) = \frac{r_e^2}{2}(1+\mu^2) \tag{A.18}$$

The PDF for scattering into the angle, μ, is given by

$$p(\mu) = \frac{\sigma_{\text{Ray}}(Z,\alpha,\mu)}{\int \sigma_{\text{Ray}}(Z,\alpha,\mu)d\mu} \tag{A.19}$$

The PDF for a given squared-momentum transfer is given by

$$P(q^2)d(q^2) = p(\mu)\left|\frac{d\mu}{d(q^2)}\right| d(q^2) \tag{A.20}$$

Solving equation A.16 for μ and differentiating, we have

$$\frac{d\mu}{d(q^2)} = \frac{-1}{K\alpha^2} \tag{A.21}$$

Substituting, equations A.17, A.18, A.21, and A.19 into equation A.20, we obtain the expression for the angular scattering PDF

$$P(q^2) = \frac{r_e^2}{(K\alpha)^2}\frac{1+\mu^2}{2}\frac{[F(q,Z)]^2}{\int \sigma_{\text{Ray}}(Z,\alpha,\mu)d\mu} \tag{A.22}$$

In MCNPX, equation A.22 is re-expressed by multiplying numerator and denominator by pairs of Z^2 and $\int_0^{q^2_{max}}[F(Z,q^2)]^2 d(q^2)$ to obtain

$$P(q^2) = \left[\frac{r_e^2 Z^2 \int_0^{q^2_{max}} Z^{-2}[F(Z,q^2)]^2 d(q^2)}{(K\alpha)^2 \int \sigma_{\text{Ray}}(Z,\alpha,\mu)d\mu}\right]\left[\frac{1+\mu^2}{2}\right]\left[\frac{[F(q,Z)]^2 Z^{-2}}{\int_0^{q^2_{max}}[F(Z,q^2)]^2 Z^{-2} d(q^2)}\right] \tag{A.23}$$

This cumbersome expression is actually written in the form of equation A.4, where the expression in the first brackets

$$C_0 = \frac{r_e^2 Z^2 \int_0^{q^2_{max}} Z^{-2}[F(Z,q^2)]^2 d(q^2)}{(K\alpha)^2 \int \sigma_{\text{Ray}}(Z,\alpha,\mu)d\mu} \tag{A.24}$$

is, in fact, a constant. The integral, $\int \sigma_{\text{Ray}}(Z,\mu)d\mu$, is the total Rayleigh scattering cross section and the other integral is obtained through interpolation between tabulated *integrated form factor* values. The expression in the second brackets of equation A.23 is

$$F(y) = \frac{1+\mu^2}{2} \tag{A.25}$$

which is a function with range, [0,1]. The third brackets contain,

$$Q(y) = \frac{[F(q,Z)]^2 Z^{-2}}{\int_0^{q^2_{max}} [F(Z,q^2)]^2 Z^{-2} d(q^2)} \tag{A.26}$$

which is the PDF for selecting a squared momentum transfer, where again, the tabulated integrated form factor is used.

A.3.1 Integrated Form Factors

The quantity,

$$\int_0^{q^2_{max}} Z^{-2}[F(Z,q^2)]^2 d(q^2) \tag{A.27}$$

is the integrated form factor. It is numerically integrated in NJOY and values are tabulated for corresponding values of q^2. The ENDF form factor tabulation specifies that $\ln[F(Z,q^2)]$ shall be linearly interpolated with $\ln[q^2]$. Thus the integrated form is tabulated as

$$\int_0^{q^2} Z^{-2}[F(Z,q^2)]^2 d(q^2) \approx \exp\left(\sum_i \ln[Z^{-2}[F_i(Z,q_i^2)]^2]\Delta[\ln(q_i^2)]\right) \tag{A.28}$$

The interpolation scheme is slightly more complicated in that ln(0) is undefined, and the first momentum transfer entry, $q_1 = 0$. Such problems are fixed in NJOY by the use of linear integration as necessary. Likewise, the ENDF creators were aware of this, and correspondingly recommend linear interpolation in such cases.

A.4 Description of MCNPX Patch 'Rayleigh Fix'

The modification described here successfully allowed MCNPX to simulate Rayleigh scattering properly, but it has been superseded by the modifications described in reference[38], which use the same logic, but also dynamically allocate variables such that the data used in MCNPX is identical to that in the EPDL97 libraries.

A description of the sampling method used to determine the scatter angle of a photon that underwent Rayleigh scattering is described in Section A.2. MCNP uses tabulated values of $C(Z,q^2)$ for each element, Z, and for fixed array of a momentum transfer values, q. The length of these tabulations was defined by the variable, MCOH= 55 words. Two arrays whose contents are defined during MCNPX initialization, VCO and WCO contained the corresponding values of q and q^2, respectively. The maximum value in VCO was $q = 6\ \mathring{A}^{-1}$. The EPDL97 contains values of $F(Z,q)$ for $q \leq 10^{11}\ \mathring{A}^{-1}$. To enable MCNPX to simulate Rayleigh scattering at all possible angles for energies of interest, new arrays of length MCOHE = 77 words were also defined in

MCNPX initialization. They contained the original 55 values of q and q^2, as well as 22 additional values, increasing quickly to $q = 10^4\ \AA^{-1}$. These arrays were named VCOE and WCOE. The only additional changes necessary to the MCNPX code was a logical check of the length of the form factor arrays (part of the JXS array). If the new form factor array had a length of MCOHE, the code would perform the exact same logic for sampling the coherent scatter PDF as is done in the un-modified code, except that the form factor array and integrated form factor arrays would be defined according to q and q^2 values of VCOE and WCOE, respectively.

The PERL scripting of the MCNPX patch follows:

```
*/ ----------------------------------------------------- GLOBAL1_zc.F
*ident 05p ( File: src/mcnpx/mcnpf/GLOBAL1_zc.F )
*i,mgp5e.24
      integer(kindi), parameter :: mcohe = 77
*/ ----------------------------------------------------- GLOBAL2_vv.F
*ident 05p ( File: src/mcnpx/mcnpf/GLOBAL2_vv.F )
*i,mgt.330
      real(kindr) :: vcoe(mcohe) = (/
     & 0.,.01,.02,.03,.04,.05,.06,.08,.1,.12,.15,.18,.2,.25,
     & .3,.35,.4,.45,.5,.55,.6,.7,.8,.9,1.,1.1,1.2,1.3,1.4,1.5,1.6,
     & 1.7,1.8,1.9,2.,2.2,2.4,2.6,2.8,3.,3.2,3.4,3.6,3.8,4.,4.2,4.4,
     & 4.6,4.8,5.,5.2,5.4,5.6,5.8,6.,6.5,7.,7.5,8.,9.,10.,11.,12.,
     & 14.,16.,18.,20.,25.,30.,40.,50.,75.,100.,500.,1000.,5000.,
     & 10000. /)
*i,mgt.339
      real(kindr) :: wcoe(mcohe) = (/
     & 0.,.0001,.0004,.0009,.0016,.0025,.0036,.0064,.01,
     & .0144,.0225,.0324,.04,.0625,.09,.1225,.16,.2025,.25,.3025,.36,
     & .49,.64,.81,1.,1.21,1.44,1.69,1.96,2.25,2.56,2.89,3.24,3.61,
     & 4.,4.84,5.76,6.76,7.84,9.,10.24,11.56,12.96,14.44,16.,17.64,
     & 19.36,21.16,23.04,25.,27.04,29.16,31.36,33.64,36.,42.25,49.,
     & 56.25,64.,81.,100.,121.,144.,196.,256.,324.,400.,625.,900.,
     & 1600.,2500.,5625.,10000.,250000.,1000000.,
     & 25000000.,100000000. /)
*/ --------------------------------------------------------- colidp.F
*ident 05p ( File: src/mcnpx/mcnpf/colidp.F )
*i,cp.137
      if ((jxs(4,iex)-jxs(3,iex))/2.eq.mcoh) then
*i,cp.153
      else
      if(t5.lt.wcoe(mcohe))go to 191
      t7=xss(jxs(3,iex)+mcohe-1)
      go to 221
  191 do 201 i=2,mcohe
  201 if(t5.lt.wcoe(i))go to 211
  211 t3=(t5-wcoe(i))/(wcoe(i-1)-wcoe(i))
      ib=jxs(3,iex)+i-1
```

```
      t7=xss(ib)+t3*(xss(ib-1)-xss(ib))
  221 t3=t7*rang()
      ib=jxs(3,iex)-1
      do 231 i=2,mcohe
  231 if(t3.lt.xss(ib+i))go to 241
  241 t3=(t3-xss(ib+i))/(xss(ib+i-1)-xss(ib+i))
      cs=1.-2.*(wcoe(i)+t3*(wcoe(i-1)-wcoe(i)))/t5
      t3=1.+cs**2
      if(t3.le.2.*rang())go to 221
      end if
 */ ------------------------------------------------------- calcps.F
 *ident 05p ( File: src/mcnpx/mcnpf/calcps.F )
 *i,ct.96
       if ((jxs(4,iex)-jxs(3,iex))/2.eq.mcoh) then
 *i,ct4b.10
      else
      if(t3.ge.vcoe(mcohe))go to 600
      do 131 i=2,mcohe
  131 if(t3.lt.vcoe(i))go to 141
  141 ib=jxs(3,iex)+mcohe+i-1
      psc=(.2494351/(tpd(2)-tpd(1)))*(1.+cs**2)*(xss(ib)+(xss(ib-1)-
     & xss(ib))*(t3-vcoe(i))/(vcoe(i-1)-vcoe(i)))**2
      end if
```

The data processing code, NJOY, must also be modified in order to create data files that contain form factor and integrated form factor arrays that reflect the MCNPX changes. This process was quite simple. The array VCO in MCNPX corresponds to an array VC in the ACER routine of NJOY. This array is modified, and subsequent assumptions of the length of VC by the following NJOY patch, created to modify NJOY259:

```
*ident upBQ05p
*d acer.14675
      dimension vi(21),vc(77)
*d acer.14687
     & 5.0d0,5.2d0,5.4d0,5.6d0,5.8d0,6.0d0,6.5d0,7.0d0,7.5d0,8.0d0,
     & 9.d0,10.d0,11.d0,12.d0,14.d0,16.d0,18.d0,20.d0,25.d0,30.d0,
     & 40.d0,50.d0,75.d0,100.d0,500.d0,1000.d0,5000.d0,10000.d0/
*d acer.14785
      jflo=jcoh+154
*d acer.14801
      do i=1,77
*d acer.14804
         xss(jcoh+76+i)=s
*d acer.14814
      do i=1,77
*d acer.15084
```

```
      write(nsyso,'(1x,1p,6e14.4)') (xss(jcoh-1+i),i=1,77)
*d acer.15088
      write(nsyso,'(1x,1p,6e14.4)') (xss(jcoh+76+i),i=1,77)
*d acer.15142
         n=21+2*77
```

Unfortunately, NJOY259 appears to have a bug that causes the program to crash in a latter section in which formatted x-ray fluorescence data tables are produced. These tables are supposed to follow the form factor array portion of the ACE file. To bypass this problem, each new ACE file, containing additional form factor data, that was produced by the modified NJOY259 code was combined with properly formatted x-ray data tables in the previously distributed ACE files. This resulted in properly functioning data files that appropriately represent the Rayleigh scattering evaluated data present in the EPDL97.

Bibliography

[1] F.R. Metzger, "Resonance Fluorescence in Nuclei," Prog. in Nuc. Phys. 7, (1959) pp. 54.

[2] U. Kneissl, H.H. Pitz, and A. Zilges, "Investigation of Nuclear Structure by Resonance Fluorescence Scattering," Prog. Part. Nucl. Phys. 37, (1996) pp. 349-433.

[3] W. Bertozzi and R. Ledoux,"Nuclear resonance fluorescence imaging in non-instrusive cargo inspection," Nucl. Instr. and Meth. B 241, pp. 820, 2005.

[4] J.F. Pelowitz (ed.), "MCNPX^{TM} USERS MANUAL Version 2.6.0," LA-CP-07-1473 (2008).

[5] D.R. Hamilton, "On Direction Correlation of Successive Quanta," Phys. Rev. 58, (1950) pp. 122.

[6] W.E. Lamb, Jr., "Capture of Neutrons by Atoms in a Crystal," Phys. Rev. 55, (1939) pp.190

[7] J.R. Phillips, "Irradiated Fuel Measurements," in *Passive Nondestructive Assay of Nuclear Materials*, D.T. Reilly, editor. Office of Nuclear Regulatory Research, NUREG/CR-5550. LA-UR-90-732 (1990) pp. 556.

[8] W.B. Wilson, T.R. England, M. Herman, R.E. MacFarlane, and D.W. Muir, "CINDER'90 code for transmutation calculations," Nuclear Data for Science and Technology Conference, Trieste, Italy (1997).

[9] M. Abs, Y. Jongen, E. Poncelet, J.-L. Bol, "The IBA rhodotron TT1000:a very high power E-beam accelerator," Radiation Physics and Chemistry Vol. 71, (2004) 285-288.

[10] J. Pottier, "A new type of RF electron accelerator: the rhodotron," Nucl. Instr. Meth. B40/41 (1989) pp. 943-945.

[11] HIGS flux performance table, DFELL/TUNL, Feb. 5, 2010 (Version 1.0). Accessed online 2, April 2010. http://www.tunl.duke.edu/pdfs/HIGSPerformance.pdf

[12] F.V. Hartemann, S.G. Anderson, C.P.J Barty, D.J. Gibson, C.A. Hagmann, M.S. Johnson, I. Jovanovic, D.P. MaNabb, M.J. Messerly, J.A. Pruet, M.Y. Shverdin, C.W. SIders, and A.M. Tremaine, "Gamma-ray compton light source development at LLNL," Proceedings of PAC07, Albuquerque, New Mexico, (2007) pp. 1245

[13] H. Ohgaki, T. Noguchi, S. Sugiyama, T. Yamazaki, T. Mikado, M. Chiwaki, K. Yamada, R. Suzuki, and N. Sei, "Linearly polarized photons from Compton backscattering of laser light for nuclear resonance fluorescence experiments," Nuclear Instruments and Methods in Physics Research A 353, (1994) pp. 384-388.

[14] F. Albert, S.G. Anderson, G.A. Anderson, S.M. Betts, D.J. Gibson, C.A. Hagmann, J. Hall, M.S. Johnson, M.J. Messerly, V.A. Semenov, M.Y. Shverdin, A.M. Tremaine, F.V. Hartemann, C.W. Siders, D.P. McNabb, and C.P.J Barty, "Isotope-specific detection of low-density materials with laser-based monoenergetic gamma-rays," Optics Letters 35, No. 3, (2010) pp. 354.

[15] F.V. Hartemann, F. Albert, G.G. Anderson, S.G. Anderson, A.J. Bayramian, S.M. Betts, T.S. Chu, R.R. Cross, C.A. Ebbers, S.E. Fisher, D.J. Gibson, A.S. Ladran, M.J. Messerly, V.A. Semenov, M.Y. Shverdin, C.W. Siders, D.P. McNabb, C.P.J Barty, A.E. Vlieks, E.N. Jongewaard, and S.G. Tantawi, "Development of a precision tunable gamma-ray source driven by a compact x-band linac," Proceedings of PAC09, Vancouver, British Columbia, (2009) WE5RFP030.

[16] M.F. Cunningham, J.N. Ullom, T. Miyazaki, S.E. Labov, J. Clarke, T.M. Lanting, A.T. Lee, P.L. Richards, J. Yoond, and H. Spieler, "High-resolution operation of frequency-multiplexed transition-edge photon sensors," Appl. Phys. Letters 81, No. 1 (2002) pp. 159.

[17] J.N. Ullom, J.A. Beall, W.B. Doriese, W.D. Duncan, L. Ferreira, G.C. Hilton, K.D. Irwin, C.D. Reintsema, and L. R. Vale, "Optimized transition-edge x-ray microcalorimeter with 2.4 eV energy resolution at 5.9 keV," Appl. Phys. Letters 87, (2005) 194103.

[18] "Ortec-Lanthanum Bromide Scintillation Detectors Data Sheet", Available online at http://www.ortec-online.com/download.asbx?AttributeFileId=e0a47196-05ea-4e35-a5a7-7ab39c66f6e1 Accessed 28 Oct 2010.

[19] J.H. Atkinson and V. Perez-Mendez, "Gas Cerenkov Counters," Rev. of Sci. Inst. 30 (1959) pp. 864.

[20] B.D. Sowerby, "Cerenkov Detectors for Low-energy Gamma-Rays," NIM 97 (1971) pp. 145-149.

[21] D.T. Vo and P.A. Russo, "Comparisons of the Portable Digital Spectrometer," Los Alamos National Laboratory Report LA-13895-MS (2002).

[22] M.J. Berger, J.H. Hubbell, S.M. Seltzer, J. Chang, J.S. Coursey, R. Sukumar, and D.S. Zucker, "XCOM: Photon Cross Sections Database, NIST Standard Reference Database 8 (XGAM)" available online at http://physics.nist.gov/PhysRefData/Xcom/Text/XCOM.html (1998).

[23] W. Bertozzi, J.A. Caggiano, W.K. Hensley, M.S. Johnson, S.E. Korbly, R.J. Ledoux, D.P. McNabb, E.B. Norman, W.H. Park, and G.A. Warren, "Nuclear resononce fluorescence excitations near 2 MeV in ^{235}U and ^{239}Pu," Phys. Rev. C 041601(R) (2008).

[24] R.D. Heil, H.H. Pitz, U.E.P Berg, U. Kneissl, K.D. Hummel, G. Kilgus, D. Bohle, A. Richter, C. Wesselborg, and P. Von Brentano, "Observation of orbital magnetic dipole strength in the actinide nuclei ^{232}Th and ^{238}U." Nuc. Phys. A476 (1988) pp. 39-47

[25] M.B. Chadwick, P. Obloinsk, M. Herman, N.M. Greene, R.D. McKnight, D.L. Smith, P.G. Young, R.E. MacFarlane, G.M. Hale, S.C. Frankle, A.C. Kahler, T. Kawano, R.C. Little, D.G. Madland, P. Moller, R.D. Mosteller, P.R. Page, P. Talou, H. Trellue, M.C. White, et al. "ENDF/B-VII.0: Next Generation Evaluated Nuclear Data Library for Nuclear Science and Technology," Nuclear Data Sheets Volume 107, Issue 12, (December 2006) Pages 2931-3118.

[26] R. E. MacFarlane, "NJOY 99 Nuclear Data Processing System", code available at http://t2.lanl.gov/codes/njoy99/.

[27] E. Browne, "Nuclear Data Sheets for A = 235,239," Nuclear Data Sheets 98, (2003) pp. 665-800.

[28] G.A. Warren, J.A. Caggiano, E.A. Miller, W. Bertozzi, A. Klimenko, S.E. Korbly, R.J. Ledoux, and W.H. Park, "Nuclear Resonance Fluorescence of ^{235}U above 3 MeV," 2007 IEEE Nuclear Science Symposium Conference Record. pp. 2047.

[29] J. McFarland, M.S. Thesis. Department of Nuclear Engineering, University of California, Berkeley. (2009).

[30] W. Geiger, Zs. Németh, I. Bauske, P. von Brantano, R.D. Heil, R.-D. Herzberg, U. Kneissl, J. Margraf, H. Maser, N. Pietralla, H.H. Pitz, C. Wesselborg, A. Zilges, "Low-lying dipole excitations in the isotopes ^{113,114}Cd," Nuc. Phys. A 580, (1994) 263-276.

[31] M. Scheck, H. von Garrel, N. Tsoneva, D. Belic, P. von Brentano, C. Fransen, A. Gade, J. Jolie, U. Kneissl, C. Kohstall, A. Linnemann, A. Nord, N. Pietralla, H.H. Pitz, F. Stedile, C. Stoyanov, and V. Werner, "Dipole strength distributions in the stable Ba isotopes $^{134-138}$Ba: A study in the mass region of a nuclear shape transition." Phys. Rev. C 70 044319 (2004).

[32] I. Bauske, J.M. Arias, P. von Brentano, A. Frank, H. Friedrichs, R.D. Heil, R.-D. Herzberg, F. Hoyler, P. Van Isacker, U. Kneissl, J. Margraf, H.H. Pitz, C. Wesselborg, and A. Zilges, "First Observation of Scissors Mode States in an Odd-Mass Nuclueus," Physical Review Letters 71 (1993) pp. 975.

[33] H. Burkhardt, P. Koehler, R. Rietmuller, B.H. Wiik, R. Fohrmann, J. Franzke, H. Krasemann, R. Maschuw, G. Poelz, J. Reichardt, J. Ringel, O Romer, R. Rusch, P. Schmuser, R.van Staa, J. Freeman, P. Lecompte, T. Mayer, S.L Wu, and G. Zobernig, "The Tasso Gas and Aerogel Cherenkov Counters," NIM 184 (1981) 319-331.

[34] Y. Allkofer, C. Amsler, S. Horikawa, I. Johnson, C. Regenfus, J. Rochet "NA nover aerogel Cherenkov detector for DIRAC-II," NIM A 582 (2007) 497-508.

[35] C.A. Hagmann, J.M. Hall, M.S. Johnson, D.P.McNabb, J.H. Kelley, C. Huibregtse, E. Kwan, G. Rusev, and A.P. Tonchev, "Transmission-based detection of nuclides with nuclear resonance fluorescence using a quasimonoenergetic photon source," J. App. Phys. 106, 084901 (2009).

[36] R. Vodhanel, M.K. Brussel, R. Moreh, W.C. Sellyey, and T.E. Chapuran, "Strong *M1* transitions in ^{23}Na below 10 MeV," Phys. Rev. C 29 2 (1984) 409.

[37] L.P. Ekström and R.B. Firestone, "WWW Table of Radioactive Isotopes," database version 2/28/99 from URL http://ie.lbl.gov/toi/index.htm

[38] J.S. Hendricks and B.J. Quiter, "MCNP/X Form Factor Upgrade for Improved Photon Transport," (LA-UR-10-01096) Journal of Nuclear Technology, *in Press.*

[39] G.W. McKinney, A.B. McKinney, J.S. Hendricks, D.B. Pelowitz, B.J. Quiter, MCNPX NRF Library - Release 2, Proc. ANS Ann. Mtg. (San Diego, CA July 13-17, 2010).

[40] J.E. Sweezy, et. al, "MCNP A General Monte Carlo N-Particle Transport Code, Version 5," LA-UR-03-1987, (2003, revised 2005).

[41] J.F. Briesmeister (ed.), "MCNP$^{\text{TM}}$ A General Monte Carlo NParticle Transport Code Version 4C," LA13709M, (2000).

[42] D.E. Cullen, J.H. Hubbell, and L. Kissel, "EPDL97: the evaluated photon data library, '97 version," UCRL-50400, Vol. 6, Rev. 5 (1997).

[43] E.D. Cashwell et. al. "Monte Carlo Photon Codes: MCG and MCP" LA-5157-MS, (March 1973).

[44] B.J. Quiter, B.A. Ludewigt, V.V. Mozin, and S.J. Tobin, "Nondestructive Spent Fuel Assay Using Nuclear Resonance Fluorescence," INMM, July 12-16, 2009, Tucson, AZ.

[45] Lynn Kissel, "RTAB: the Rayleigh scattering database," Radiation Physics and Chemistry Vol. 59, (2000) 185-200.

[46] C.J. Lodwick and H.J. Spitz, "Modification to the Monte Carlo N-Particle Code for Simulating Direct, In Vivo Measurements of Stable Lead in Bone," Health Physics, Vol. 94, No. 6 (2008) pp. 519-526.

[47] L.S. Waters (ed.), "MCNX$^{\text{TM}}$ USER'S MANUAL Version 2.3.0," LA-UR-02-2607 (2002).

[48] L. Kissel, B. Zhou, S.C. Roy, S.K. Sen Gupta, R.H. and Pratt "The Validity of Form-Factor, Modified-Form-Factor and Anomalous-Scattering-Factor Approximations in Elastic Scattering Calculations," Acta Cryst. A51, (1995) 271-288.

[49] A.I. Milstein and M. Schumacher, "Present status of Delbrück scattering," Physics Reports 243, (1994) pp. 183214.

[50] H.C. Cheng, E.-C. Tsai, and X. Zhu, "Delbrück scattering," Phys. Rev. D 26, no. 4, (1982) pp. 908.

[51] A. Scherdin, A. Schäfer, W. Greiner, G. Soff, and P.J. Mohr, "Coulomb corrections to Delbrück scattering," Z. Phys. A 353, (1995) pp. 273-277.

[52] R. Solberg, K. Mork, and I. Øverbø, "Coulomb and screaning corrections to Delbrück forward scattering," Phys. Rev. A 51, No. 1 (1995) pp. 359.

[53] B. Kasten, D. Schaupp, P. Rullhausen, F. Smend, M. Schumacher, and L. Kissel, "Coulomb correction effect in Delbrück scattering and atomic Rayleigh scattering of 1-4 MeV photons," Phys. Rev. C 33, No. 5 (1986) pp. 1606.

[54] P. Rullhausen, F. Smend, and M. Schumacher, "Delbrück scattering of 2754 keV photons by Nd, Ce, I, Sn, Mo, and Zn," Phys. Letters 84B, No. 2 (1979) pp. 166.

[55] H. Falkenberg, A. Hünger, P. Rullhausen, and M. Schumacher, "Amplitudes for Delbrück scattering," Atomic Data and Nuclear Data Tables 50, (1992) pp. 1-27.

[56] T. Bar-Noy and S. Kahane, "Numerical calculations of Delbrück scattering amplitudes," Nuc. Phys. A 288, (1977) pp. 132-140.

[57] U. Berg and U. Kneissl, "Recent progress on nuclear magnetic dipole excitations," Ann. Rev. Nucl. Part. Sci 37, (1987) 33-69.

[58] H. Arenhövel, “Photon scattering by nuclei: theory and experiment,” *Procedings of the Internation Conference on Photonuclear Reactions and Applications*, edited by B.L. Berman, Lawrence Livermore Laboratory (1973) pp. 449.

[59] W.D. Myers, W.J. Swiatecki, T. Kodama, L.J.El-Jaick, and E.R. Hilf, “Droplet model of the giant dipole resonance,” Phys. Rev. C 15, No. 6 (1977) pp. 2032.

[60] L. Jianfeng, S. Zongdi, and Z. Yixin, “Giant dipole resonance parameters,” Reference Input Parameter Library. Available online at http://www-nds.iaea.org/RIPL-2/ (2001).

[61] T.E.O. Ericson and J. Hüfner, “Low-frequency photon scattering by nuclei,” Nuc. Phys. B 57, (1973) pp. 604-616.

[62] B.L. Berman, “Atlas of photoneutron cross sections obtained with monoenergetic photons,” Atomic Data and Nuclear Data Tables 15, (1975) pp. 319-390.

[63] P. Rullhusen, W. Mückenheim, F. Smend, M. Schumacher, G.P.A Berg, and L. Kissel, “Test of vacuum polarization by precise investigation of Delbrück scattering,” Phys. Rev. C 23, No. 4 (1981) pp. 1375.

[64] J.L. Frian, “Low-Energy Theorems for Nuclear Compton and Raman Scattering and $0^+ \rightarrow 0^+$ Two-Photon Decays in Nuclei,” Annals of Physics 95, (1975) pp. 170-201.

[65] P. Rullhusen, F. Smend, and M. Schumacher, “Elastic Scattering of 2.754 MeV Photons by Ta and Interference between Rayleigh, Thomson and Delbrück Scattering,” Z. Physik A 288, (1978) 119-123.

[66] P. Rullhusen, F. Smend and M. Schumacher, “Delbrück scattering of 2754 keV photons by Nd, Ce, I, Sn, Mo and Zn,” Physics Letters 84B, No. 2 (1979) pp. 166.

[67] C.J. Hagmann and J. Pruet,“Photon production through multi-step processes important in nuclear resonance fluorescence experiments,” NIM B 259, (2007) pp. 895-909.

[68] ANSI N14.1-2000, Table 1.

[69] R. Berndt, E. Franke, and P. Mortreau, “^{235}U enrichment or UF_6 mass determination on UF_6 cylinders with non-destructive analysis methods.” Nucl. Inst. and Meth. in Phys. Reas. A 612 (2010) 309-319.